

LASER FUSION BASED 3D-PRINTING OF NITINOL SHAPE MEMORY ALLOY FOR  
BIOMEDICAL APPLICATIONS

By

Md Sarower Hossain Tareq

A DISSERTATION

Submitted to  
Michigan State University  
in partial fulfillment of the requirements  
for the degree of

Mechanical Engineering – Doctor of Philosophy

2024

## ABSTRACT

Nitinol is highly attractive for biomedical applications because of its unique shape memory and superelastic properties as well as acceptable biocompatibility. Additive manufacturing (AM) is getting significant attention in making complex and patient customizable nitinol devices. However, due to its high microstructural and compositional sensitivities, it is still challenging to fabricate functional NiTi devices via AM. It has been widely reported that evaporation of Ni, oxidation of Ti and formation of precipitation phases during fabrication significantly diverts the expected functional properties. To this date, laser powder bed fusion (LPBF) was the choice among many AM techniques to fabricate NiTi devices but successfully fabricated only on a NiTi substrate because of its poor bonding to other substrates (i.e., steel and Ti). In this work, a multi-step printing approach was systematically developed, which enabled printing NiTi on a Ti substrate using a very low laser energy density of  $35 \text{ J/mm}^3$  without any visible defect such as delamination and crack. This printing method reduced the high warping issue due to the process induced residual stress, avoided the Ni evaporation issue as well as formation of undesirable precipitation phase during printing. It was also found that a higher oxygen level in the printing chamber reduced the austenite finish ( $A_f$ ) temperature and negatively affected the printability.

The as-printed NiTi sample exhibited distinct one-step phase transformation with the  $A_f$  temperature of  $2.1^\circ\text{C}$ . To increase the  $A_f$  temperature to  $30.2^\circ\text{C}$  (within the recommended range of  $A_f$  temperature for biomedical applications), a heat treatment protocol was developed, which includes a solution cycle (at  $900^\circ\text{C}$  for 1 hour) followed by an aging cycle (at  $450^\circ\text{C}$  for 30 minutes). The heat treatment protocol enabled to attain the homogenized microstructure while creating ultrafine metastable Ni-rich precipitate,  $\text{Ni}_4\text{Ti}_3$ , which facilitated the desirable phase transformation behavior with the increased  $A_f$  temperature. The heat-treated sample showed narrower and sharper two-step martensitic phase transformation with the formation of intermediate

R-phase. The presence of both  $\text{Ni}_4\text{Ti}_3$  and the R-phase was confirmed by the transmission electron microscopic (TEM) analysis. In the superelasticity test at the body temperature, these samples, starting from the 2<sup>nd</sup> cycle, demonstrated a recovery ratio of more than 90% and a recoverable strain of more than 6.5%. After 10<sup>th</sup> cycles, the stable recoverable strain was 6.52% with a recovery ratio of 96%, which is the highest superelasticity reported for the LPBF processed NiTi to the best of our knowledge. After the initial deformation process, we expect these samples to attain near full superelasticity during service. The micro-hardness study showed that the hardness of the heat-treated samples is less affected by the cyclic loading.

Nitinol stent is attractive since they are self-expandable and behave superelastically when deployed inside the body. In contrast to the multi-step conventional manufacturing route, AM is attractive in making nitinol stent since it provides one-step processing as well as wide option for customizable design. However, the individual strut of a stent is less than 150  $\mu\text{m}$  which is very challenging to fabricate by LPBF with structural accuracy, mechanical integrity and maintaining proper superelasticity. In this work, the LPBF processing parameter, as well as the post heat treatment and surface finish has been systematically developed to minimize the porosity, avoid structural failure during deformation and maximize the superelastic property at body temperature. Finally, the processed thin strut showed the  $A_f$  temperature of 33 °C (which is less than the body temperature) and demonstrated complete superelasticity with 100% strain recovery ratio with 4.5% recoverable strain at body temperature, which is first time to report complete superelasticity in AM processed NiTi thin sample that is suitable for the stent application. The work presents an important roadmap in making NiTi devices by AM while maintaining excellent functional properties of NiTi for biomedical applications.

Copyright by  
MD SAROWER HOSSAIN TAREQ  
2024

To my dearest wife, Sumaiya Afrin, without whose unwavering support throughout this endeavor, I would be lost and helpless.

To my parents, who dreamed of educating me amidst their struggles.

To my youngest uncle, who was the greatest source of motivation during my childhood.

## **ACKNOWLEDGEMENTS**

To my advisors, Dr. Patrick Kwon and Dr. Haseung Chung, for their unwavering support, invaluable feedback, and patience throughout this journey.

To my committee, for their guidance and encouragement.

To Mr. Edward Drown, the research assistant in the composite materials and structural center, for assisting in evaluating the mechanical and thermal properties.

To my colleague Bibek Poudel and Hoa Nguyen for their assistance at the beginning of the project.

## TABLE OF CONTENTS

Chapter 1: Introduction .....	1
Chapter 2: Printing Nitinol with Superelastic Characteristics on a Ti Substrate .....	26
Chapter 3: Developing the Post Heat Treatment Protocol for the Biomedical Applications .....	50
Chapter 4: Optimizing the Printing Parameters and Post Processing Conditions to Fabricate Superelastic Stent.....	73
Chapter 5: Summary and Future Work.....	91
REFERENCES .....	93

# Chapter 1: Introduction

## 1.1. Background

Among the shape memory alloys, nitinol (equiatomic alloy of Ni and Ti, NiTi) is the most useful because of its superior ability to retain the original shape after deformation. Through the reversible phase transformation between the high temperature austenite phase and low temperature martensite phase, NiTi can retain its originally trained shape after deformation either by unloading (superelasticity) or heating (shape memory). Because of these two unique behaviors, the alloy has significant importance in numerous engineering applications [1], [2], [3]. In particular, along with the functional properties, good biocompatibility and corrosion resistance made the alloy highly attractive in making biomedical devices such as stents, endoscopic instruments, dental implants and orthopedic devices [4], [5], [6]. However, most of the NiTi parts in biomedical applications are in complex shapes and may require customizable designs. To date, commercial NiTi parts are fabricated in traditional manufacturing routes, also known as subtracting manufacturing (SM), which require multi-step processing such as casting, rolling, forging and subtracting techniques such as laser cut to attain the required final part geometry [7], [8]. However, though SM provides with undeniable advantage of low-cost mass production, the option of making complex structure with customizable design for individual are the great limitation in the SM routes. Additive manufacturing (AM), on the other hand, provides the capability of producing highly complex parts virtually without any geometrical limitation and offers customizable design without increasing manufacturing lead time. Therefore, in recent years, AM techniques have drawn significant interest in biomedical industries, where being able to provide complexity and customization are more important.

The functional properties of NiTi are highly sensitive to and dependent on the composition and microstructure [9], [10]. Therefore, fabricating NiTi parts with expected final properties has always been challenging. Though making biomedical parts from other materials (such as Ti, steel, etc.) have significantly studied for long period, it is only last few years when making NiTi by AM have been attempted. To date, most of the studies on the ‘AM of NiTi’ have been conducted focusing on the preliminary aspects of printing such as the effect of printing parameters on the printability, transformation temperature, microstructure, and mechanical properties, in general. Studies focused on making NiTi parts with certain transformation and functional properties by AM are scarce. There are still certain challenges associated with printing NiTi parts, such as maintaining the same composition and phases in the printed part as to the powder, achieving the printability of NiTi on other than nitinol substrate, and finally getting required superelastic and shape memory properties in the printed part.

For NiTi biomedical devices, certain transformation and functional properties must be maintained in the fabricated part to be used inside the body [11]. For instance, most of the biomedical implants, stents and devices require austenite transformation ( $A_f$ ) temperature to be below the body temperature (37 °C) and require certain level of superelasticity [12]. One good example can be a cardiovascular stent that needs to be superelastic at body temperature and possesses certain mechanical properties to open the blockage in the vessel.

This dissertation mainly focuses on developing the AM method to fabricate the NiTi parts with proper phase transformation and superelastic properties for biomedical applications. Along with the printing parameters, study on the post heat treatment to tailor the transformation and functional properties of the printed NiTi part for the biomedical application is another goal to achieve. While

achieving the NiTi parts with certain properties, addressing the challenges in fabricating NiTi by AM are also substantial interest to meet in this dissertation.

## **1.2. Nitinol and its functional properties**

Nitinol is a relatively new engineering material discovered in 1962 at Naval Ordnance Laboratory in White Oak, Maryland, by William J. Buehler and Frederick Wang [13]. It is an equiatomic alloy of nickel and titanium and is the most attractive metallic shape memory alloy (SMA) for biomedical applications among all other SMA discovered to date. Other notable SMAs prior to NiTi include Au-Cd (1932) and Cu-Zn (1950). However, after the alloy was discovered, though the discoverers quickly recognized the special property of nitinol and its usefulness in numerous applications, it was not possible to commercialize the nitinol devices until 1990 due to the difficulties associated with the melting, processing, and machining. Now a days, nitinol is highly desirable for numerous engineering components in biomedical, aerospace, automotive and thermoelectrical industries. Two unique properties such as superelasticity and shape memory, that made nitinol so attractive as ‘smart materials’ are briefly discussed below.

### **1.2.1. Superelasticity**

Nitinol shows superelastic behavior in the austenite phase, therefore, at a temperature above austenite finish ( $A_f$ ) nitinol is mostly a superelastic material. Upon applied stress above  $A_f$  temperature (below  $M_d$ ), nitinol can be deformed elastically up to 10% [1], [14]. Like other metallic alloys, deformation of nitinol does not include movements of atomic planes (or slip) or plastic deformation by means of dislocation [5], [15]. Rather, upon applied stress, deformation of nitinol mostly happen by means of phase transformation from austenite to martensite which is recoverable upon unloading, and this reversible phase transformation phenomena enables nitinol to demonstrate significantly higher recoverable strain.

Above  $A_f$  temperature, the most stable phase of nitinol is austenite. The schematic stress-strain plot of a superelastic nitinol above  $A_f$  temperature is shown in Figure 1.1 [12]. When nitinol is loaded above  $A_f$ , austenite elastically deforms first until a strain of 1 to 2 % (zone I in Figure 1.1). After a critical stress is reached, austenite transforms to martensite, which is known as stress induced martensite (SIM). In the stress-strain plot, SIM normally appears as a stress plateau with longer strain up to 6% (zone II in Figure 1.1). At the end of the plateau, the alloy is completely martensite, and upon further loading, martensite deforms elastically to a certain point (zone III in Figure 1.1). If loading is further continued, the martensite will deform plastically (zone IV in Figure 1.1) mostly unrecoverable, and therefore, plastic deformation should be avoided for biomedical implants. For biomedical applications, nitinol is generally unloaded from the end of SIM to ensure maximum strain recovery. Since the most thermodynamically stable phase is austenite above  $A_f$  temperature, upon unloading martensite transforms back to austenite while most of the strain is recovered. Most of the biomedical application of nitinol relies on the superelastic property, and hence in biomedical devices, the  $A_f$  temperature is kept closely below the body temperature to ensure that the austenite phase is stable when the device is inside the body.

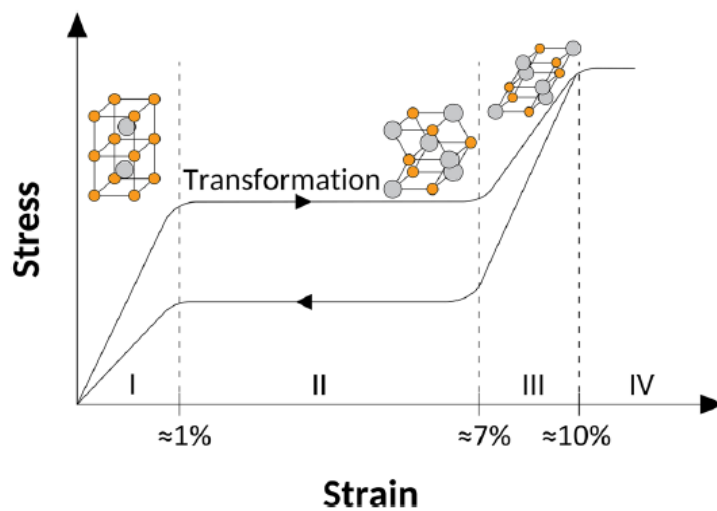


Figure 1.1. Deformation of superelastic nitinol at a temperature above  $A_f$ . Zone I to IV indicate different stage during deformation [12].

### 1.2.2. Shape memory property

The recovery of the original shape after deformation by means of heating is known as shape memory property of nitinol. Below  $M_f$  (martensite finish) temperature, the stable phase for nitinol is martensite, which is a twinned structure (Figure 1.2) [16]. If nitinol is deformed below  $M_f$ , instead of phase transformation, it deforms in traditional way by means of elastic deformation followed by plastic deformation. Upon unloading, the strain associated with the plastic deformation is not recovered. However, unlike traditional metals where plastic deformation happens through dislocation motion, plastic deformation in nitinol is basically detwinning of the twin martensite structure [2]. When this plastically deformed detwinned nitinol is heated above  $A_f$  temperature, where austenite is the stable phase, the detwinned martensite reverses back to austenite [17].

Since no slip or dislocation was associated with the deformation process, the original shape is preserved when transforming back to austenite. This process of retaining original shape by heating is known as shape memory effect. There are some interesting applications of shape memory effect such as coupling of two pipes in cryogenic temperature and heat engine [18]. However, the shape memory property of nitinol is not widely used in biomedical applications.

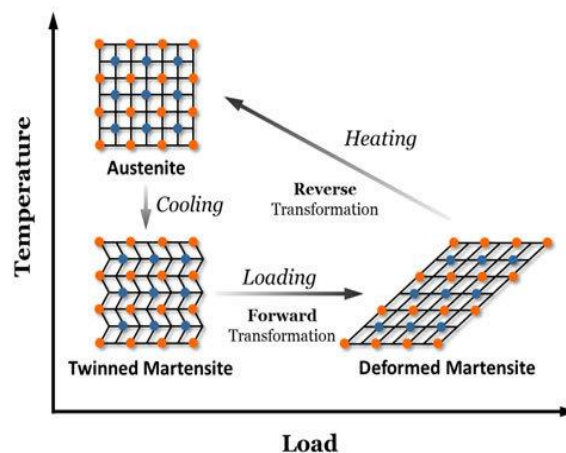


Figure 1.2. Schematic showing shape memory effect of nitinol [6].

### 1.3. Metallurgy of Nitinol

The nickel-titanium equiatomic alloy in the binary nickel-titanium binary phase diagram is known as nitinol (Figure 1.3) [19]. According to the phase diagram, nitinol can be considered as an ordered intermetallic alloy below the eutectoid point at 630 °C. The alloy only shows its unique functional properties such as superelasticity and shape memory property for a very narrow range of compositional variation. The alloy possesses two major phases, austenite at high temperature and martensite at low temperature. The phase transformation temperature between austenite and martensite phases is directly related to the nickel to titanium ratio in the matrix phase and a slight deviation in the composition significantly affects the phase transformation properties [20]. The change in  $A_s$  and  $A_f$  with the change in Ni content is shown in Figure 1.4 [20]. For instance, a 0.5% increase in the titanium or nickel content in the NiTi matrix phase drops the  $A_f$  temperature by 50 °C.

The microstructure of nitinol at room temperature depends on the composition and thermal history of the alloy. For example, if the alloy is slightly Ti rich, upon cooling from liquid phase it will form Ti rich precipitation phase such as  $Ti_2Ni$ . The presence of Ti rich precipitates significantly degrades the functional property and therefore are generally avoided during processing [21]. If the alloy is slightly Ni rich, the solidification process will result in eutectic NiTi phase and Ni rich  $TiNi_3$  precipitates. Presence of Ni rich precipitates was found not to degrade the functional properties and thus most of the biomedical grade nitinol are made from Ni rich NiTi (typically 50.8 at.% Ni) alloy to get maximum superelastic property [22]. However, the formation of  $TiNi_3$  depends on the cooling rate and mostly form in the equilibrium condition. From the phase diagram in Figure 1.3, it is seen that upon cooling, the solubility limit of the NiTi quickly narrow down to a single line below 630 °C and make the equilibrium cooling more difficult to achieve. Therefore,

in general due to kinetics, metastable  $\text{Ni}_4\text{Ti}_3$  and  $\text{Ni}_3\text{Ti}_2$  forms instead of  $\text{Ni}_3\text{Ti}$ .  $\text{Ni}_4\text{Ti}_3$  has significant effect on the phase transformation and functional properties of NiTi and have been widely discussed in the literature [23, p. 3], [24, p. 3].

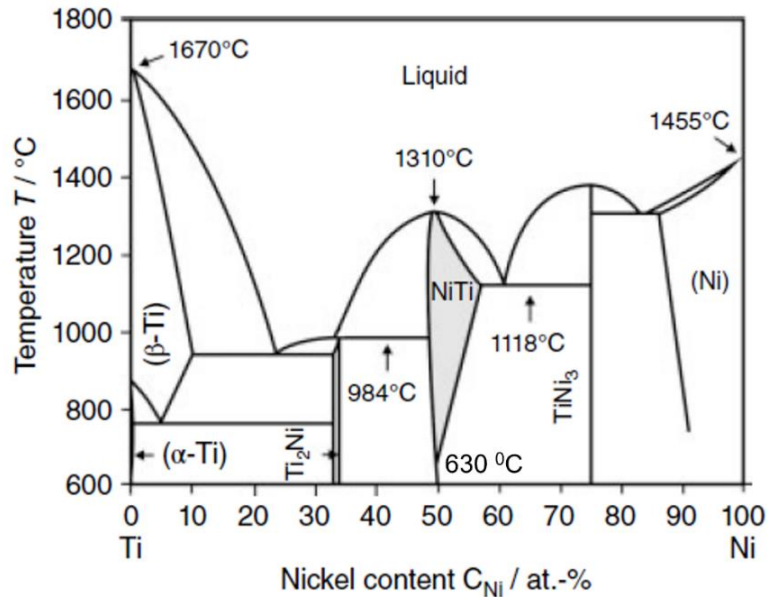


Figure 1.3. Nickel – titanium binary phase diagram [19].

The reason for the unique superelasticity and shape memory property of nitinol is the diffusion-less phase transformation between the austenite and martensite phases. At room temperature, the equilibrium NiTi possess austenite microstructure (known as B2 structure) with two interlocking simple cubic lattices consisting of nickel and titanium atoms as shown in Figure 1.5 (known as CsCl structure) [12]. The thermodynamically stable austenite phase can be become unstable with applied load (in the form of temperature or mechanical loading) and the unstable phase transform to a meta-stable phase to accommodate the applied load. This transformation happens in a shear action with a coordinated displacement of the atomic plane rather than the diffusion of atoms or breaking the bonds between atoms. The newly formed meta stable phase is known as martensite phase which possesses B19' structure with monoclinic lattice as shown in Figure 1.5 [25]. The martensitic transformation is highly dependent on the temperature. Above  $M_s$  temperature, the

martensite is thermodynamically unstable, whereas austenite is stable. However, if the material is deformed, the stable austenite becomes unstable and transform to the martensite phase even at a temperature higher than the  $M_s$  temperature.

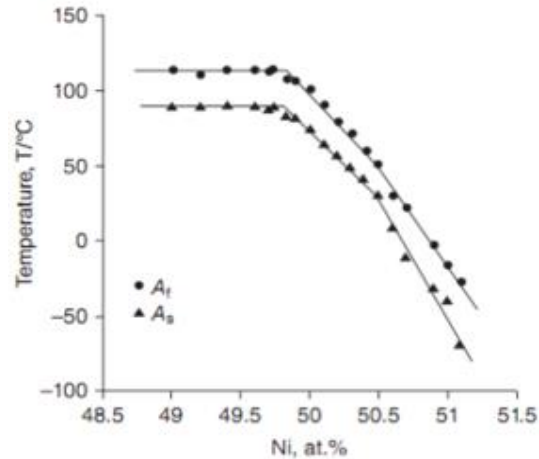


Figure 1.4. Change in austenite start ( $A_s$ ) and finish ( $A_f$ ) temperature with Ni content in the matrix phase [20].

This transformation to martensite is known as SIM as defined earlier. Upon removal of load, the martensite goes back to the austenite since martensite cannot thermodynamically be stable at the temperature. In this case, the applied deformation is completely recovered upon unloading, known as superelasticity.

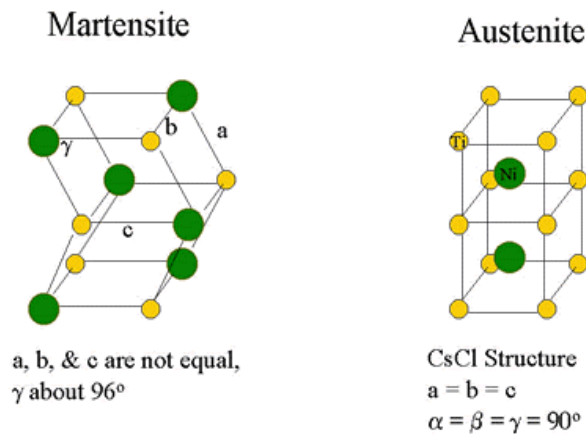


Figure 1.5. Structure of nitinol in two different phases. Monoclinic martensite (left side) and BCC austenite (right side) [8].

However, there is another temperature known as  $M_d$  (martensite dead temperature) above which austenite cannot transform to the martensite upon loading, regardless of the magnitude of load. In that condition, deformation happens in a conventional way such as elastically followed by plastic deformation. Above the  $M_d$  temperature, martensite is completely unstable, and SIM does not happen. Therefore, in biomedical parts, since superelasticity is the mostly desired property, the  $M_d$  and  $A_f$  temperatures are kept above and below the body temperature, respectively [12].

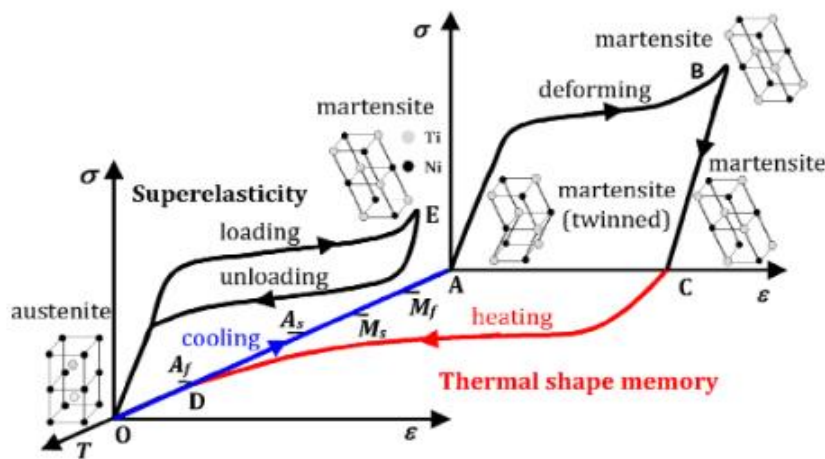


Figure 1.6. Superelasticity and shape memory effect of NiTi in terms of temperature, stress and strain [26].

Again, below the  $M_s$  temperature, austenite becomes unstable and starts transforming to the martensite. At  $M_f$  temperature, the austenite completely transforms to the martensite. Below  $M_f$ , if the material is deformed upon loading and then unloaded, the deformation will not be recovered since martensite is stable below  $M_f$  temperature. Upon heating to the  $A_s$  temperature, the martensite will start transforming, and it will completely transform to the austenite and the deformation will be completely recovered when reaching the  $A_f$  temperature. The superelasticity and shape memory property of nitinol is schematically presented in Figure 1.6 in terms of temperature, strain, and stress [26].

#### **1.4. Additive manufacturing (AM) processes for nitinol**

It has been reported that fabricating NiTi parts in conventional manufacturing routes was challenging because of the alloy's high affinity to the oxygen and high sensitivity to the contaminations that degrade the shape memory and superelastic property [27], [28]. In addition, most of the NiTi parts in biomedical applications are of complex structures that require extensive and precise machining. However, it has been widely reported that machining of NiTi is very difficult because of high ductility, high work hardening and spring back effect with excessive tool wear [19], [26]. These aspects in conventional manufacturing routes of fabricating NiTi make the process challenging and expensive. Therefore, additive manufacturing (AM), providing the design flexibility and one-step fabrication route, has drawn significant attention in making the structurally complex NiTi parts [27], [29].

Among the two types of AM processes, beamless process (such as binder jet printing) is less suitable for making NiTi due to the high oxidation associated with the debinding and sintering steps as well as the difficulty in achieving fully dense parts [29], [30]. Among the beam-based processes, selective laser melting (SLM), electron beam melting (EBM) and direct energy deposition (DED) are the most widely used AM processes to fabricate metallic parts. Among these processes, selective laser melting (SLM) provides with high resolution and better surface finish, and therefore, SLM is reported to be the preferred AM method in fabricating thin and complex NiTi parts [29], [30]. Wang et al. [31], [32] and Farber et al. [31], [32] studied various AM methods to print NiTi and concluded that SLM provides with better geometrical accuracy, density and transformation properties in the final printed part. SLM technique belongs to the powder bed fusion family of AM classification. In SLM, the laser selectively melts and sinters the powder layer on a metal substrate.

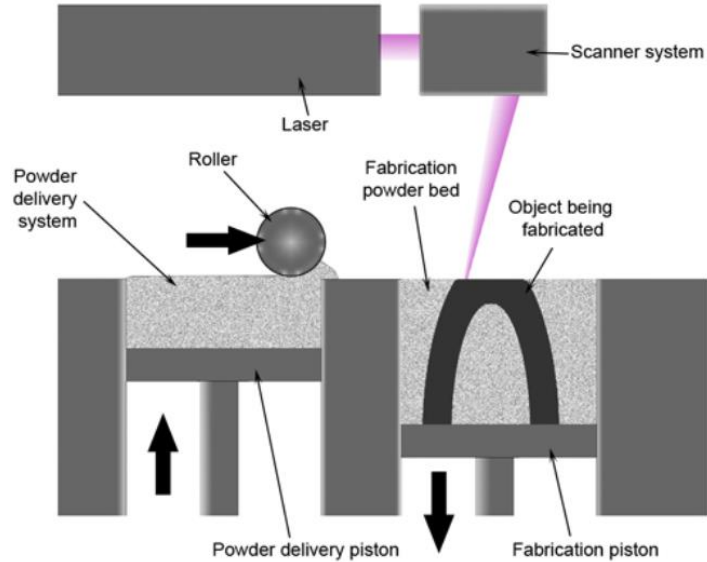


Figure 1.7. Schematic of laser powder bed fusion (LPBF) process [29].

After one layer is consolidated, the powder spreading mechanism spreads another powder layer on top of the previous layer which is again selectively melted by the laser based on the CAD model. This process is repeated until the part is finished. The powder layer thickness in SLM is usually selected between 35 to 100  $\mu\text{m}$  depending on the powder size. During printing, the printing chamber is controlled to avoid the oxidation issue. In some SLM facilities, the substrate is preheated to reduce the thermal gradient during printing and minimize the residual stress. A schematic diagram of the SLM system is shown in Figure 1.7 [33]. The laser energy density is a widely used term to determine the volumetric energy of the density used to sinter the powder.

$$\text{Laser energy density, } LED = \frac{P}{S \cdot L \cdot H}$$

Where P is laser power (W), S is laser speed, L is layer thickness and H is hatch spacing.

SLM parameters used to print NiTi play an important role not only in the final density but also the transformation and functional property of the printed part. It has been shown by the researchers that the laser input energy density, which is a function of laser power, speed, hatch spacing and layer thickness, is the key factor that influences the transformation and functional property of NiTi.

The  $M_s$  and  $A_f$  temperatures were found to generally increase with increasing laser energy density [28], [34]. Wang et al. [35] reported that laser speed has more influence on the variation of the phase transformation temperature as compared to the variation of hatch spacing or laser power. Crystallographic texture of the printed NiTi sample also plays important role on the superelastic and shape memory behaviors [36], [37]. A certain combination of processing parameter is critical in achieving preferred crystal orientation to obtain the maximum superelasticity [38]. Therefore, it is very important to use proper processing parameters to achieve expected transformation and functional property in the printed NiTi part.

### **1.5. Challenges in printing nitinol**

The phase transformation and functional properties of NiTi are highly sensitive to the microstructure and composition of the fabricated part. Even the smallest change in the Ni content in the matrix phase and presence of any precipitation phase or oxide inclusions in the microstructure significantly change the final functional properties [20], [30]. For instance, 0.5 at.% drop in the Ni content shift the  $A_f$  temperature upward by 30 °C [20], [39]. Therefore, fabricating NiTi by AM processes requires addressing these challenges in achieving expected final properties.

#### **1.5.1. Residual stress and warping**

One of the major challenges in printing NiTi by SLM is excessive built-in residual stress and warping. Because of the low thermal conductivity of NiTi, comparatively higher thermal residual stress grows in the printed layers that cause warpage and distortion in the final part [29]. In some cases, after printing a few layers, the deposited part peels off from the substrate, which makes difficult to continue printing. To avoid such issue stemming also from poor bonding, using a nitinol substrate is a common practice [35], [40]. However, nitinol substrate is very expensive and not easily available. To minimize the warping distortion during printing, substrate heating has been

recommended by some researchers [41], [42]. However, it has been reported that substrate heating adversely affects the transformation temperature of the printed NiTi parts [reference]. Substrate heating acts as a heating agent for the printed part and triggers the formation of secondary precipitation phase during printing. Also, with the substrate heating, the cooling rate of each melt pool is comparatively slower, which provides adequate time for the precipitation to form in the microstructure. Formation of nickel or titanium rich precipitations in the microstructure changes the Ni/Ti ratio in the matrix phase and consequently changes the  $A_f$  and/or  $M_s$  temperatures of the printed part. Wang et al. [43] reported that change in substrate heating from 150 °C to 350 °C shifted the  $A_f$  to the upward by 9 °C as shown in Figure 1.8 [43]. This happened because at high substrate heating temperature, the previously formed  $Ni_4Ti_3$  precipitates coarsened in size and reduced the nickel content in the matrix phase.

### 1.5.2. Evaporation of nickel

The second most widely reported challenge in printing NiTi is the evaporation of nickel during printing. Because of Ni's lower vaporization enthalpy, boiling point (374.8 kJ/mol & 2913 °C) and higher vapor pressure (425.5 kJ/mol and 3287 °C) as shown in Figure 1.9 [40], Ni easily evaporate

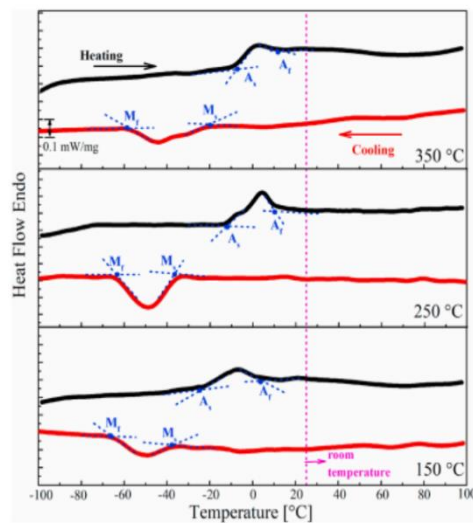


Figure 1.8. DSC result of Ni-rich NiTi alloy printed with different substrate heating [43].

from the melt pool during printing and reduces the Ni/Ti ratio in the matrix phase that consequently increases the phase transformation temperature of the printed part in an uncontrollable way [34], [35], [44]. Haverland et al. [34] and Wang et al. [34], [35] printed NiTi in SLM using various levels of energy density and reported that, with increasing energy density, the  $A_f$  of the printed sample shifted upward due to the increased amount of Ni evaporation. Another study noted that no transformation peak in the DSC test was observed in the printed sample attributing the possible reason to the high Ni evaporation that shifted the  $A_f$  temperature upward and beyond the DSC scan range [45]. To achieve expected transformation and functional properties, it is very critical to maintain the compositional consistency in the printed part. Therefore, studying the optimal processing parameters to avoid Ni loss during printing is essential.

### 1.5.3. Formation of precipitation phase

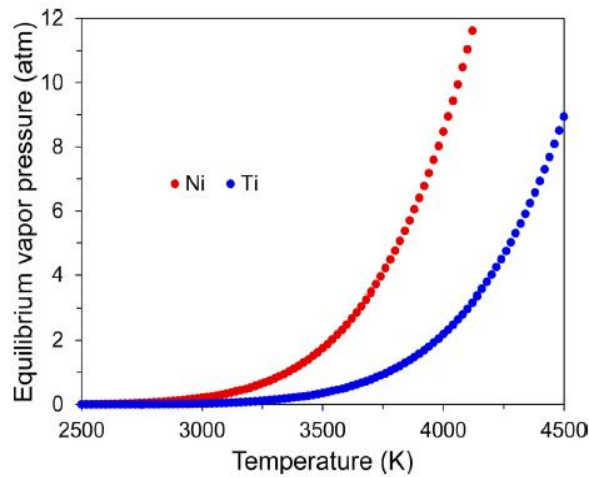


Figure 1.9. Equilibrium vapor pressures of Ni and Ti for Ti-50.0 at.% Ni alloy [31].

Another widely reported phenomena during NiTi printing is the formation of secondary precipitation phases [30], [31], [46]. NiTi is very sensitive to the thermal cycle and easily forms Ni or Ti rich precipitates in the microstructure between 300 °C to 600 °C for holding very short period (even for 5 minutes) [19], [47]. Wang et al. [31] reported that formation of Ni rich

precipitation during printing depleted the Ni content in the matrix phase and shifted the  $A_f$  upward. Even though precipitates are sometimes beneficial and most of the time are intentionally formed by the heat treatment to tailor the transformation properties, it is still hard to control their formation during printing.

#### **1.5.4. Crystallographic texture effect**

Besides the composition and phases, crystallographic texture has remarkable influence on the mechanical and functional properties of the NiTi [37], [48], [49]. For instance, strong crystallographic texture of [001] along the loading direction provides with maximum compressive superelasticity because of the low critical stress for phase transformation in [001] direction [36], [50]. In conventional manufacturing routes, certain crystallographic texture could be achieved by plastic deformation such as rolling. Whereas, in AM method, achieving expected crystallographic texture is challenging since the crystallographic growth depends on various aspects such as laser parameters, building direction, part geometry as well as complex thermal cycles of SLM. Therefore, understanding the effect of various parameters on the grain growth during solidification is necessary in fabricating the NiTi part with expected crystallographic texture.

#### **1.6. Heat treatment to tailor nitinol properties**

Heat treatment (HT) is one of the most powerful methods to tailor the transformation and functional properties of NiTi alloy. HT of nitinol can be classified as homogenization HT (also known as solution HT) and aging HT. Homogenization HT is generally performed between 850 °C and 1050 °C in an inert atmosphere [19], [51]. In homogenization HT, any secondary precipitation phases presence in the microstructure gets dissolved in the matrix phase. Homogenization HT is also performed on the additively manufactured parts to reduce the residual stress as well as making the microstructure comparatively uniform [32], [47]. On the other hand,

aging HT is performed between 300 °C to 600 °C to intentionally create the Ni or Ti rich secondary precipitation phases from the Ni or Ti rich NiTi matrix, respectively.

Depending on the aging temperature and time, the secondary precipitation formed in nickel rich

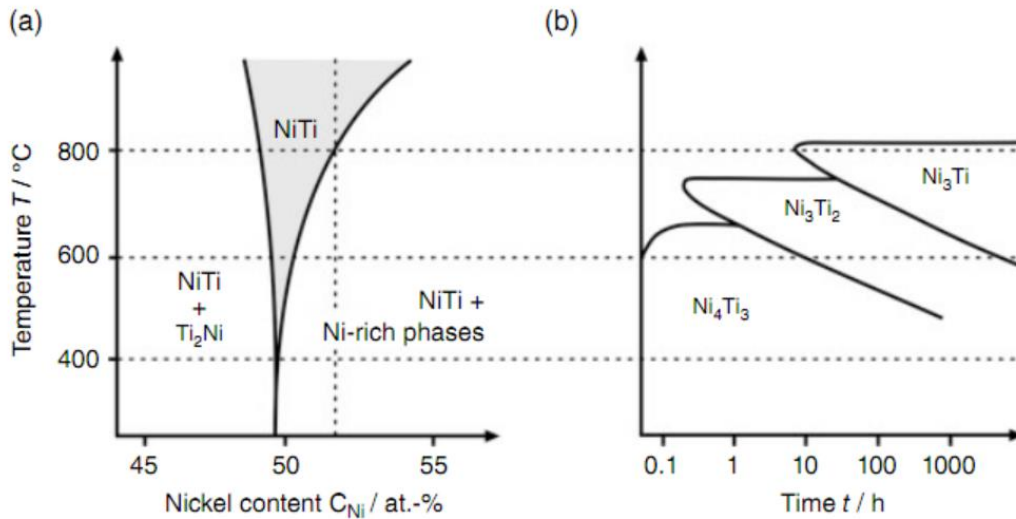


Figure 1.10. a) Section of the nickel-titanium binary phase diagram. b) isothermal transformation diagram of a Ni<sub>52</sub>Ti<sub>48</sub> alloy showing the respective precipitation phase for the temperature and holding time [19].

NiTi alloy are Ni<sub>4</sub>Ti<sub>3</sub>, Ni<sub>3</sub>Ti<sub>2</sub> and Ni<sub>3</sub>Ti. The precipitation phases expected to form from a Ni-rich NiTi alloy corresponding to the holding temperature and time is shown in Figure 1.10 [19]. With low aging temperature and short aging time, the precipitation formed are mostly Ni<sub>4</sub>Ti<sub>3</sub>, whereas, with higher aging temperature and longer aging time, the metastable Ni<sub>3</sub>Ti<sub>2</sub> are formed. The stable Ni<sub>3</sub>Ti precipitates only form when the aging time is considerably longer [19]. It is noted that in all types of HT, the NiTi samples are generally quenched from the holding temperature to ensure fast cooling so that there is not enough time for any extra precipitation to form during cooling. Both homogenization and aging HT significantly affect the phase transformation temperature of the NiTi alloy. In the Ni-rich NiTi alloy, upon homogenization HT, the Ni-rich precipitations are dissolved, which increases the Ni/Ti ratio in the matrix phase. Consequently, the transformation temperatures ( $M_s$  or  $A_f$ ) of the Ni-rich NiTi generally is decreased by the homogenization HT.

Whereas, since aging HT creates new Ni-rich precipitation phases, the Ni/Ti ratio of the matrix phase decreases, and the transformation temperature increases. Saedi et. al. performed solution HT of the SLM printed NiTi sample at 950 °C for 5.5 hours followed by aging HT at 350 °C and 450 °C for various holding times [47]. The DSC result of the heat-treated samples are shown in Figure 1.11 [47]. After homogenization HT, they found that the  $A_f$  of the sample decreased by 20 °C which was attributed to the dissolved precipitation phases that increased the Ni/Ti of the NiTi matrix phase. The transformation peaks in the DSC test of the homogenized sample were found to be sharper which was attributed to the comparatively homogeneous microstructure after the HT. After aging HT, it was found that the longer aging time provided with higher  $A_f$  temperature because of the formation of larger amount of nickel rich precipitates with increasing holding time. For instance, at 350 °C temperature, increase in aging time from 5 minutes to 3 hours increased the  $A_f$  temperature by 50 °C. It also was reported that for aging time longer than 30 minutes provided with two-steps phase transformation peaks in the DSC test. This was attributed to the formation of  $Ni_4Ti_3$  precipitates in the microstructure that facilitated with two-steps phase transformation as B2 – R – B19’.

The presence of precipitation phase also affects the functional properties of the NiTi alloy. For instance, presence of smaller size  $Ni_4Ti_3$  in the microstructure act as a barrier to the dislocation motion and increases the strength of the alloy [19]. This ultimately reduces plastic deformation and increases the recoverable strain, thus enabling us to achieve superelasticity, upon unloading. However, presence of larger size precipitation phase adversely effects the mechanical and functional properties due to the reduced deformation [23, p. 4]. Therefore, it is very critical to

explore proper HT protocol to achieve expected transformation and functional behaviors in the final NiTi part.

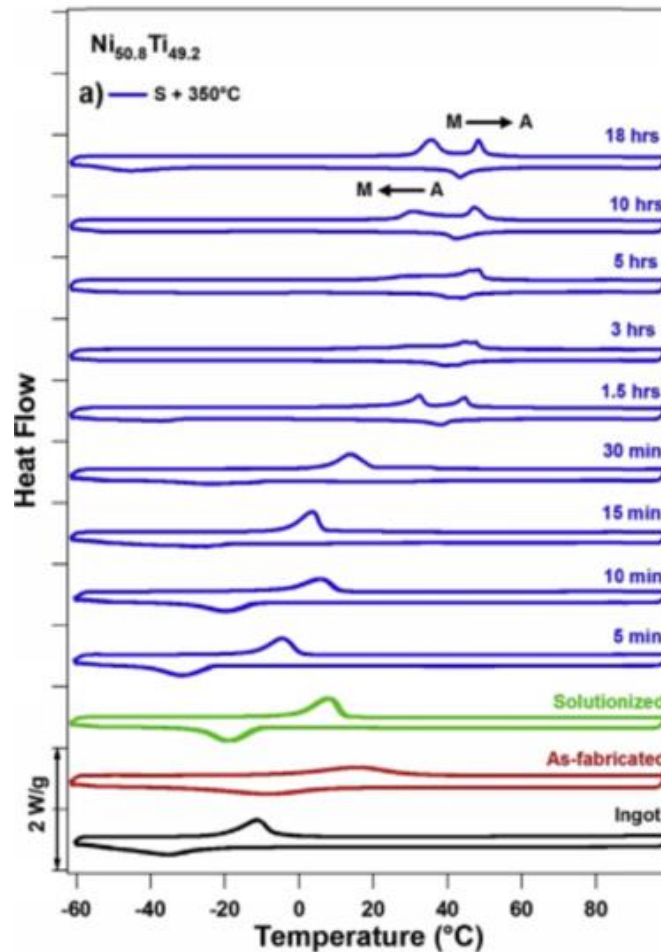


Figure 1.11. DSC plot of the LPBF printed  $\text{Ni}_{50.8}\text{Ti}_{49.2}$  sample after homogenization HT at 950 °C for 5.5 hours and aging HT at 350 °C for various holding temperature [47].

### 1.7. Biomedical application of nitinol: Stent

Nitinol is mostly attractive in the biomedical applications due to its good biocompatibility, corrosion resistance in the body fluid as well as the excellent shape memory property [11], [52]. Like the biological materials, such as hair, bone and tendon, nitinol can be deformed elastically, in some cases up to 10%, and demonstrate a nonlinear stress-strain behavior upon unloading which is rare in any other metallic alloy as shown in Figure 1.12 [11], [53]. Therefore, nitinol is highly

desirable as bone replacement, dental implants, surgical devices, endoscopic instruments, and endovascular stents.

Stent is a hollow cylindrical mesh-like small device used to treat and restore blood flow through the narrowed or clogged arteries [6], [54]. The commonly used material for stenting until recent time are cobalt-chromium and stainless steel. Stents made from these materials are expanded using a balloon to place inside the body. The balloon-expandable stents have perceived risk in carotid arteries to be permanently deformed through outside pressure once the buckling pressure is exceeded, resulting in a partially or completely blocked vessel [55], [56]. In contrast, because of the superelastic property, nitinol stent is self-expandible and does not require any balloon to place it inside the body. ‘Kink resistance’ of nitinol stent is an important feature that protect the stent to be deformed upon outside force [6].

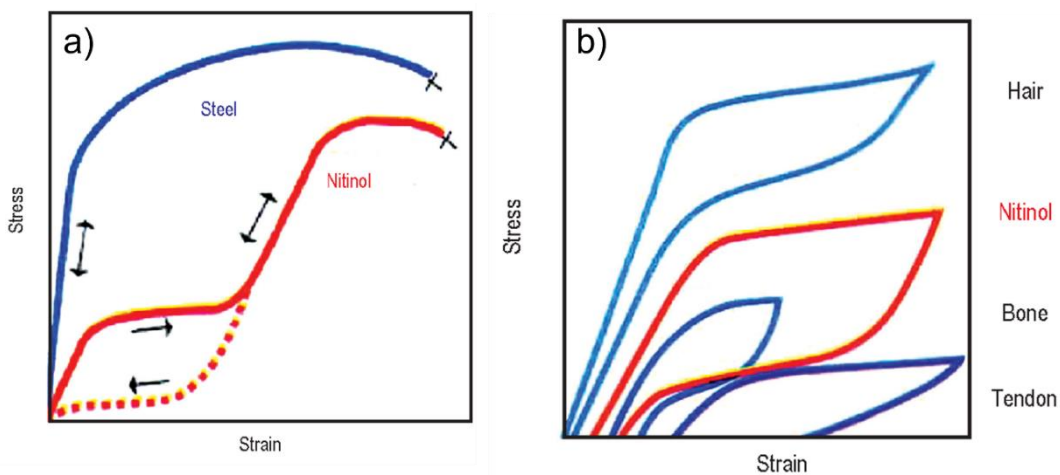


Figure 1.12. a) Stress-strain curve of steel and nitinol. b) Biomechanical compatibility of nitinol showing non-linear stress-strain behavior [39].

The nitinol stent is manufactured with the  $A_f$  temperature less than body temperature ( $37\text{ }^\circ\text{C}$ ) to ensure that the stent is in the austenite phase when placed inside the body. Figure 1.13 shows the steps of a self-expandible stent starting from the as-fabricated stent till the deployment. The stress-

strain associated with the manufacturing, packaging and deployment of a nitinol stent is shown in Figure 1.14 [53].

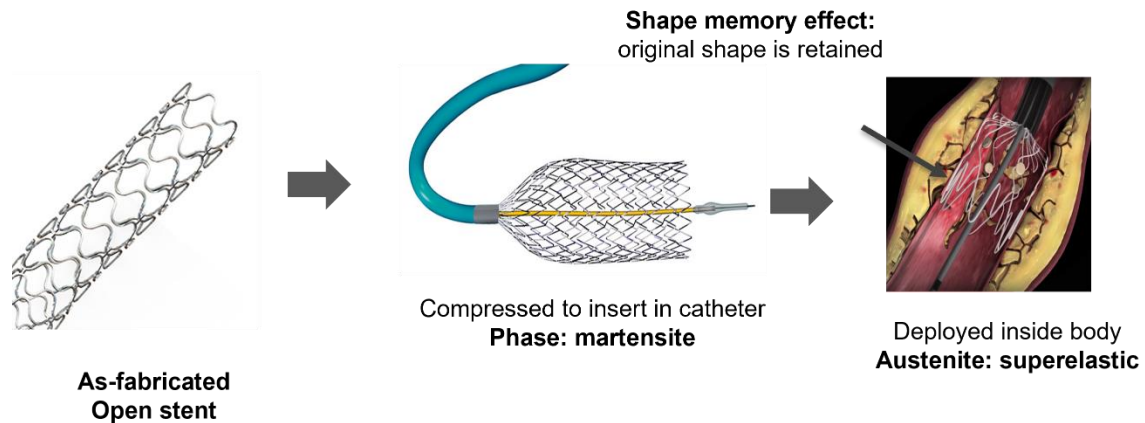


Figure 1.13. The deployment steps of a self-expandable stents.

The original manufactured stent diameter is large (i.e., 7 mm) and is radially compressed to a smaller diameter (i.e., 2 mm) upon applied loads to insert inside a catheter to place inside the body. The compressed stent is in the martensite phase and, when released inside the body, it transforms back to the austenite, and the stent expands. However, the expansion is constrained by the vessel wall such that the stent cannot recover its complete strain (i.e., the expanded diameter 5.5 mm). This incomplete reverse transformation creates an outward force on the vessel wall which is known as “biased-stiffness” [57]. The biased-stiffness saves the stent to be collapsed by the outward force since this requires high elastic force following the loading direction of stress-strain curve. On the other end, the continuous expansion of the stent with the expansion of the body vessel diameter is easy because the incomplete austenite-to-martensite transformation requires less stress to happen. These are the unique features of nitinol that made the materials highly demanding for stent application.

The commercially available nitinol stent is conventionally manufactured through laser cutting from a tubular precursor followed by shape setting and aging HT [55]. However, customizable design is not possible or a stent with multiple branches is difficult to fabricate in conventional manufacturing process.

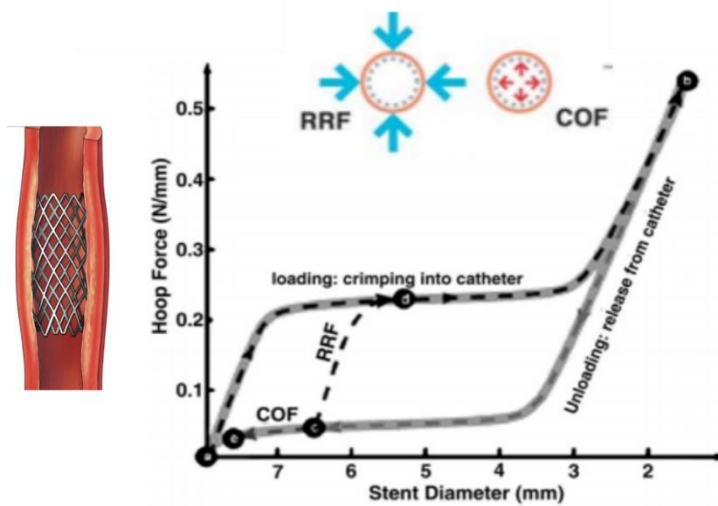


Figure 1.14. Loading states vs. change in diameter of a self-expandible nitinol stent from manufacturing till deployment [39].

AM process, on the other hand, provides the freedom of customizable design with complex geometries, thus, attractive to make nitinol stents. However, making stents in AM method is difficult because of the challenges associated with printing very thin struts (i.e., 200  $\mu\text{m}$ ) in the stent in compared to the laser beam spot and powder size used, in general [58]. Also, achieving proper transformation temperature and superelasticity are extremely challenging due to the high sensitivity of these properties on the composition and microstructure. Only few attempts have been reported to print nitinol stent by SLM method [44], [59], [60]. However, these attempts were mainly focusing on the physical property of the stent. The research dedicated to studying the effect of SLM parameter on the transformation temperature and superelasticity of thin struts is completely uncharted. It is very important to study and optimize the SLM parameters as well as

develop the proper heat treatment protocol (as required) to obtain appropriate  $A_f$  temperature and superelasticity in the thin strut that can be used to ultimately print the stent.

### **1.8. Performance and additive manufacturing of stent**

The performance of a stent depends on the materials property as well as the design optimization. The materials properties required for a stent include enough mechanical strength, proper austenite finish temperature and the superplastic property. A stent needs to have enough mechanical strength so that it can sustain under load applied during the deformation process to insert into a catheter, and when deployed inside a body vessel. The stent needs to have an austenite finish temperature less than the body temperature so that the stent is completely in the austenite phase when deployed inside the body. It is also important to ensure that the stent behaves superelastically when deployed inside the body so that it can retain its original shape in case it is deformed upon any external load during service.

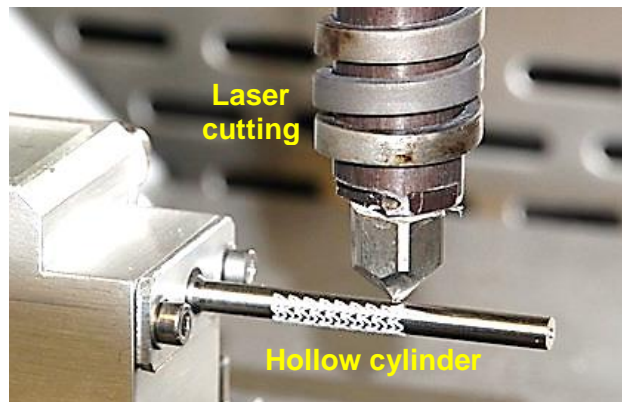


Figure 1.15. Traditional stent manufacturing: selective laser cutting from a hollow cylinder [26].

The most common reason for stent failure during service is the structural failure [6], [53]. The two major reasons for a stent to have structural failure are presence of internal porosity and surface defects. The presence of pores inside the structure reduces the overall load bearing cross-sectional area and increases the local stress that led to the premature failure. Again, presence of surface

defects such as inclusions or surface irregularities act as a stress concentration site and significantly reduce the fatigue performance.



Figure 1.16. Optical micrograph of a 300 μm printed nitinol cross section with pores.

In traditional stent manufacturing route, where stent is made by selective laser cutting from a cast and machined hollow cylinder (Figure 1.15), maintaining full density and better surface finish were comparatively easier. However, in additive manufacturing it is challenging to avoid these bulk and surface defects. The individual strut of a stent is less than 150 μm (Figure 1.16).

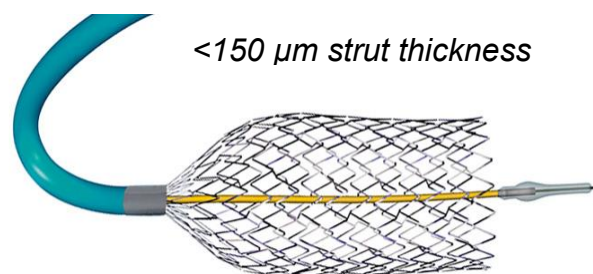


Figure 1.17. 3D view of a stent and catheter [31].

It is well known that making thin structures by AM is always challenging due to the poor structural accuracy, mechanical integrity attributed to the high pores and surface defects [61]. Specially, in a stent, where each strut is less than 150 μm, presence of a 10 μm diameter spherical pore significantly reduces the load bearing capacity (Figure 1.17).

Therefore, it is very critical to optimize the AM processing conditions for stent to achieve near full density, better surface finish as well as higher superelasticity.

### **1.9. Dissertation outline**

The dissertation has been outlined in dedicating the effort to develop the processing conditions to address the challenges in fabricating NiTi by laser powder bed fusion as well as optimizing the processing conditions to achieve the desired physical, mechanical, and functional properties for the biomedical applications. In Chapter 2 to 4, the targeted properties of the final NiTi part, challenges in achieving these properties, developed processing conditions to address the challenges as well as the experimental result with materials characterization have been elaborately discussed in term of the processing-microstructure-property relationship. **Chapter 2 presents the work done to enable printing NiTi on a Ti substrate.** The chapter starts with mentioning the initial challenges experienced in printing NiTi on a Ti substrate. The underlying reasons for the challenges have been discussed in terms of materials property. The developed printing method was then presented that enabled to print NiTi on the Ti substrate while explaining the advantages of the method to overcome the challenges experienced initially. The chapter also discusses the steps taken to avoid the compositional changes due to the Ni evaporation and precipitation phase formation during printing. **The effect of oxygen content on the printability and the phase transformation behavior** of the NiTi part have also been presented in this chapter. **The experiments performed on the NiTi sample printed on Ti substrate are also presented in this chapter.** The microstructure observation, Phase and compositional analysis, mechanical test as well as the superelasticity test result have been presented in this chapter. The mechanical test result has been explained elaborately in relation to the processing conditions as well as based on the observation from the materials characterization. Because of the process limitation, achieving the

desired properties for biomedical application in the as printed NiTi is challenging. Therefore, post heat treatment has been studied to optimize the proper treatment cycle. **Chapter 3 focuses on the work performed to develop the heat treatment protocol to achieve the desired phase transformation and superelastic characteristics for the biomedical applications.** Study on different heat treatment temperature and time, their effect on the phase transformation behavior as well as the underlying reasons of these behaviors in relation to the change in the microstructure and composition have been explained in this chapter. Among the different heat treatment cycles studied the appropriate cycles that provide with properties required for the biomedical applications has been specially studied and characterized. The mechanical, microstructural, phase and compositional analysis of the heat treated NiTi have been presented in this chapter with reasonable explanation. Finally, **Chapter 4 presents the work performed to print NiTi stent.** The critical challenges in printing thin struts, the criteria to overcome these challenges have been discussed. Finally, the study to optimize the printing parameter, post surface treatment and the post heat treatments to fabricate the NiTi stent with structural accuracy, mechanical integrity, proper phase transformation and superelastic properties haven been elaborately discussed.

## **Chapter 2: Printing Nitinol with Superelastic Characteristics on a Ti**

### **Substrate**

#### **2.1. Introduction**

To this date, laser powder bed fusion (LPBF) was the choice among many AM techniques to fabricate NiTi devices but successfully only on a NiTi substrate because of its poor bonding to other substrates (i.e., steel and Ti). Expensive NiTi substrate significantly limits the economic feasibility of fabricating NiTi parts.

This chapter focuses on a systematic approach to develop a method to print NiTi on a Ti substrate and without any substrate heating. The chapter also focuses to explore the printing parameters to minimize the Ni evaporation as well as the formation of secondary precipitation phase during printing to maintain the compositional consistency in the printed sample while avoiding any visible crack or delamination. The challenges experienced to print NiTi on Ti substrate have been discussed, the systematic development of the multi-steps printing method that enabled printing NiTi on the Ti substrate has been elaborately explained. Finally, mechanical and superelastic tests as well as the different material characterizations have been performed to evaluate the properties of the printed sample.

#### **2.2. Materials and Method**

##### **2.2.1. Materials**

Pre-alloyed NiTi powder with 55.5 wt.% (50.7 at.%) Ni content was acquired from AP & C, a GE Additive Company (St-Eustache, Québec, Canada). The powder was mostly spherical with the diameter range between 10  $\mu\text{m}$  and 45  $\mu\text{m}$ . The SEM and EDS were performed on the as-received powder to confirm the size, shape, and composition as shown in Figure 2.1. XRD was also performed to reveal the phases present in the as-received powder as shown in Figure 2.1.

### 2.2.2. Printing Method

The printing was performed in ProX DMP 200 3D Systems (Santa Clarita, California, USA) with a continuous fiber laser of wavelength 1070 nm and beam diameter of 70  $\mu\text{m}$ . The printing was performed on a Ti substrate without any prior substrate heating in a chamber of 300 ppm oxygen level. The NiTi sample was finally fabricated using a laser power of 150 W, speed of 1900 mm/s, layer thickness of 45  $\mu\text{m}$  and hatch spacing of 50  $\mu\text{m}$ .

Initially, it was not possible to directly print NiTi on the Ti substrate because of the poor bonding of the printed layer to the substrate. When the residual stress of the printed part exceeds the substrate-layer bonding strength, the printed layers, being significantly warped, were peeled off from the substrate. The warped and peeled off layers block the roller from spreading the powder for the next layer. Therefore, printing could not be continued beyond three to four layers. Applying multiple design of experiments (DoEs), a printing method was developed to print on the Ti substrate without any prior substrate heating.

At first, three layers (will be mentioned as ‘base layers’) of powder was deposited using the high laser energy density (LED) of 148  $\text{J}/\text{mm}^3$  to ensure that the layers are well bonded to the substrate. On top of the base layers, twenty-five layers of the lattice structure were printed. The final bulk sample was then printed on top of the lattice structure (detail in section 2.3.2). The lattice and the final sample were printed using a very low LED (35  $\text{J}/\text{mm}^3$ ) to minimize Ni evaporation as well as the formation of precipitation phase while avoiding any delamination and cracking. The printing parameters for the base layers, lattice and final bulk sample are listed in Table 2.1.

Table 2.1. List of the printing parameters used to print different steps of the developed printing structure.

Printing stage	Laser power (W)	Laser speed (mm/s)	Hatch spacing ( $\mu\text{m}$ )	Layer thickness ( $\mu\text{m}$ )	Volume energy density ( $\text{J}/\text{mm}^3$ )
Base layer	200	600	50	45	148
Lattice	150	1900	50	45	35
NiTi sample	150	1900	50	45	35

### 2.2.3. Experimental Method

The phase transformation behaviors of the as-received powder and printed sample were investigated using the differential scanning calorimetry (DSC) (TA 2000) from TA instruments (New Castle, Delaware) with the scan rate of  $10\text{ }^\circ\text{C}/\text{min}$  between  $-80^\circ\text{C}$  to  $150^\circ\text{C}$  under Ar gas with the flow rate of  $50\text{ mL}/\text{min}$ . Phase analysis was conducted using a Bruker D8 Discover X-ray Diffractometer equipped with a Vantec 500 detector and Cu K  $\alpha$  ( $0.15406\text{ nm}$ ) X-ray source. Microscopic observations of the as-received NiTi powder and printed samples were also carried out in a scanning electron microscope (SEM, Tescan Mira3 FEG) using both secondary electron (SE) and backscattered electron (BSE) detectors. The samples were prepared by grinding up to 1200 grit sandpaper followed by polishing with 0.3- and 0.1-micron alumina suspension and a water based colloidal silica ( $0.06\text{ }\mu\text{m}$ ). Compositional analyses were performed using the same SEM equipped with an energy dispersive X-ray spectroscopy (EDS) detector. The crystallographic orientation was investigated by electron backscattered diffraction (EBSD) in the same SEM using EDAX TSM OIM data collection system-7 with a step size of  $0.1\text{ }\mu\text{m}$  and tilt angle of  $70^\circ$ . The data obtained from EBSD were processed in the Aztec Crystal software to plot the inverse pole figure (IPF) map with colored grain texture as well as the pole figures. The data was cleaned up using a confidence index (CI) of less than 0.05 and grain dilution was done with CI greater than 0.1 and a misorientation angle less than  $5^\circ$ .

One-way and cyclic compression tests of the printed samples were performed in a uniaxial load frame by United Calibration Corporation (Model SFM-20) in displacement control with a load cell of 20 KN and at strain rate of 0.5 mm/min at room temperature. The load vs displacement data obtained from the test was converted to strain vs. stress data using the following formula.

$$\text{Strain} = \frac{\text{Change in height}}{\text{Initial height}}$$

$$\text{Stress} = \frac{\text{Load}}{\text{Cross sectional area}}$$

To study the mechanical property, the printed sample was loaded under compressive stress until fracture. To investigate the stress-strain behavior under different stress levels, a load-unload test under incremental stresses was performed in a sequence of stresses at 75, 150, 275 and 375 MPa, respectively. The cyclic compression test under 300 MPa up to 10 cycles was performed to investigate the superelastic properties of the fabricated NiTi samples.

## 2.3. Result and Discussion

### 2.3.1. Microstructure, composition, and phase analysis of the NiTi powder

The SEM images of the as-received powder are shown in Figure 2.1. The NiTi powder used in the study is mostly spherical with the diameter ranged from 10  $\mu\text{m}$  to 45  $\mu\text{m}$ . The composition of the

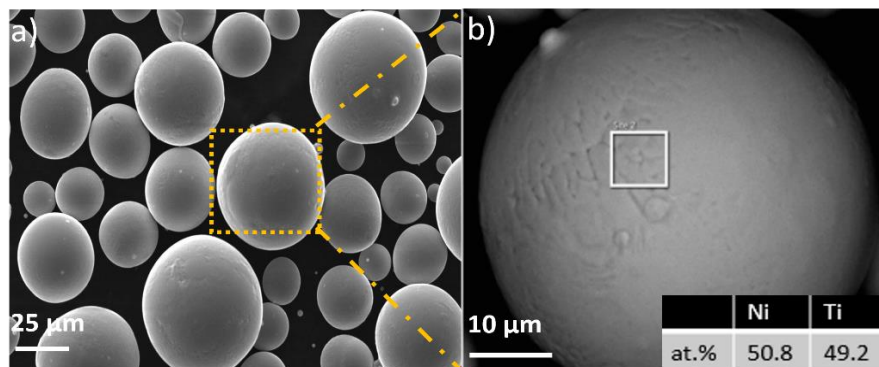


Figure 2.1. (a) SE image of NiTi powder. (b) BSE image with EDS composition attached.

powder, by EDS analysis, was found as 55.5 wt.% (50.6 at.%) Ni which is same to the supplier data sheet. The powders contained 0.027 wt.% of oxygen.

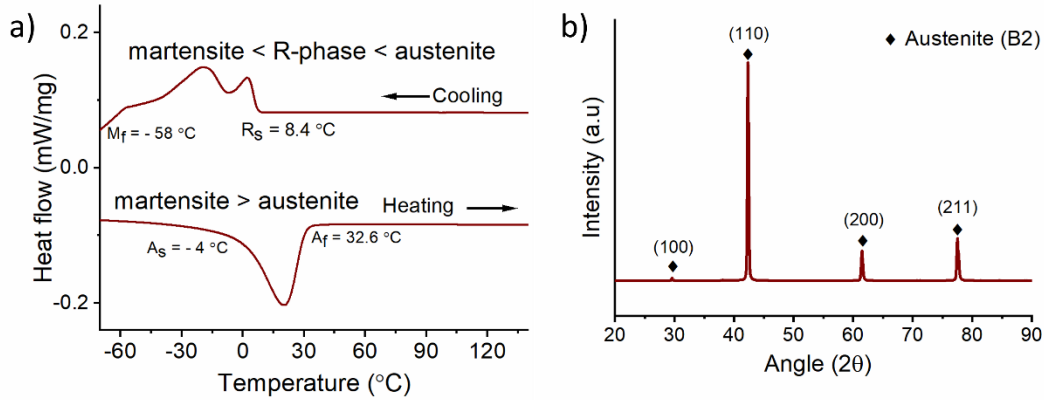


Figure 2.2. a) DSC phase transformation plot, b) XRD spectra of the as received powder.

The phase transformation behavior of the powder is shown in Figure 2.2(a) which clearly indicates the forward (austenite to martensite) and reverse phase transformation (martensite to austenite) peaks with martensitic ( $M_f$ ) and austenitic ( $A_f$ ) finish temperature of  $-62\text{ }^\circ\text{C}$  and  $32.6\text{ }^\circ\text{C}$ , respectively. Phase analysis by XRD of the as-received powder is shown in Figure 2.2(b) which indicates austenite (B2) as the major phase at room temperature.

### 2.3.2. Printability of NiTi on Ti substrate and developed printing method

Because the substrate made of the same material provides strong bonding, NiTi has only been successfully printed, to the date, on the NiTi substrate in LPBF. However, since NiTi substrate is very expensive and not readily available, this study attempts to develop a new method to print the NiTi on a Ti substrate, which is readily available and cost-effective. The major challenge in printing NiTi on a Ti substrate is the poor substrate-part adhesion with the high residual stress accumulated during printing. The printed layers as little as few layers can be peeled off by the high residual stress, preventing the powder spreading mechanism from functioning properly

(Figure 2.3). To resolve this issue, a multi-step printing method is developed, enabling printing NiTi on the Ti substrate.

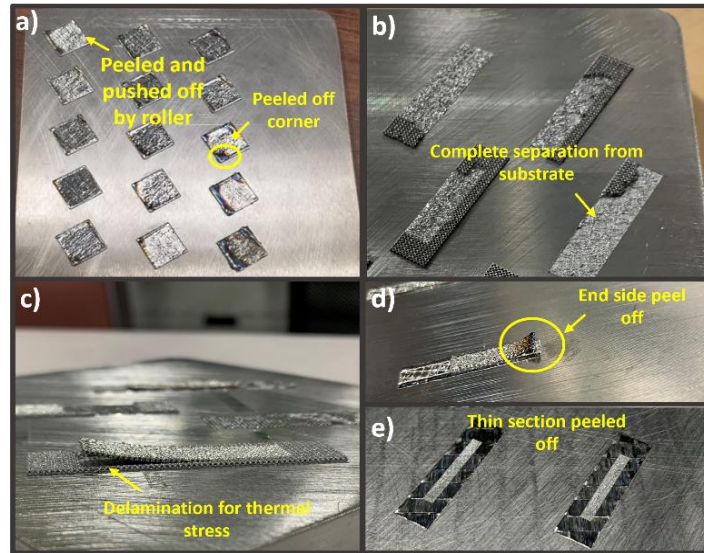


Figure 2.3. Failed printing shows the challenges experienced in printing NiTi on Ti substrate. (a) corner peels off. The peeled off corner heads up and blocks the roller movement. (b) Complete separation from substrate by pushing away subsequently by roller. (c) Bulk layer exerts pulling force and delaminates the whole structure from substrate. (d) Delamination starts from the end of the long structure. (e) Complete peel-off of the long thin bulk structure from substrate.

The schematic diagram of the multi-step printing method is shown in Figure 2.4. First, three NiTi layers (denoted as base layers) are deposited on the Ti substrate using a high LED scanning. The high LED was used to ensure complete diffusion between the substrate and the printed layers in order to achieve the possible maximum bonding strength. From the DOE, the energy density of  $148 \text{ J/mm}^3$  was found to be optimal that enabled us to print a maximum number of layers without delamination. A lower LED density makes the substrate-layer bonding weaker due to the lack of diffusion. Again, very high LED also makes the bonding weaker because of the keyhole porosity and high spattering of the melt pool during printing.

On top of the high LED printed base layers, instead of printing the bulk and continuous layer, the lattice structure in a hexagonal unit cell was printed to reduce the residual stress in the deposited

layers. In the lattice structure, the overall cross-sectional area in contact with the underneath base layer is less than the bulk and continuous structure. The lattice structure with reduced stiffness

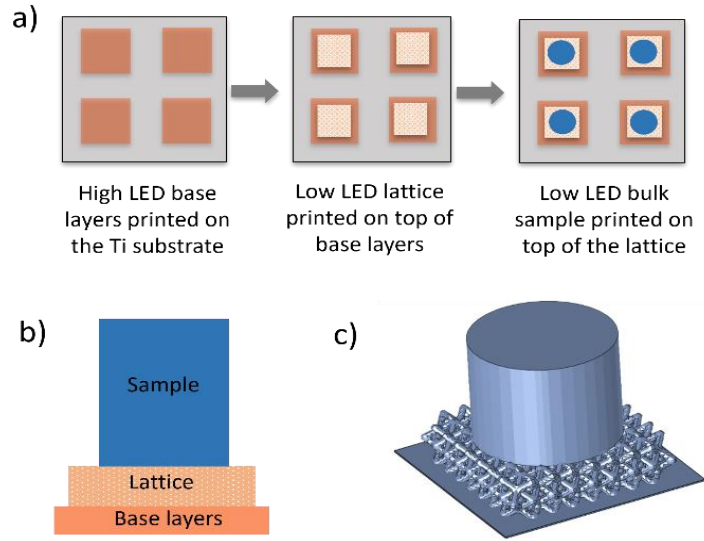


Figure 2.4. The schematic showing the step wise printing method from (a) top view, (b) front view, (c) 3D picture.

relieves the thermal residual stress during cooling. The combined strategies reduced the residual stress developed in the deposited layers and avoided delamination. The lattice structure was printed at least up to 25 layers (the total thickness of 0.875 mm) and the final bulk sample was then printed on top of the lattice structure. Both the lattice and the bulk sample were printed using the energy density of  $35 \text{ J/mm}^3$  that was obtained using a DOE. The energy density less than  $35 \text{ J/mm}^3$  suffered from severe delamination and cracking due to the lack of diffusion. Cubic and cylindrical samples printed using this printing method are shown in Figure 2.6(a) and 2.6(b).

### 2.3.3. Effect of scan strategy and printability of long thin wall structure

Scan strategy was found to play an important role on the printability of NiTi on the Ti substrate, especially, in printing the long thin structure. However, for the smaller cross section of circular (5 to 10 mm diameter) or square shape (5 to 10 mm sides), the scan strategy did not make a considerable difference on the printability. For long and thin structures (such as  $25 \times 2$  or  $20 \times 1.5$

mm), unidirectional scanning along the longitudinal direction was found to be inappropriate and scanning the whole length at a time increases residual stress along the longitudinal direction. This results in one end of the layer significantly being warped and peeled off from the substrate, and printing could not be continued beyond the first few layers (Figure 2.5(a)). Thus, the longitudinal

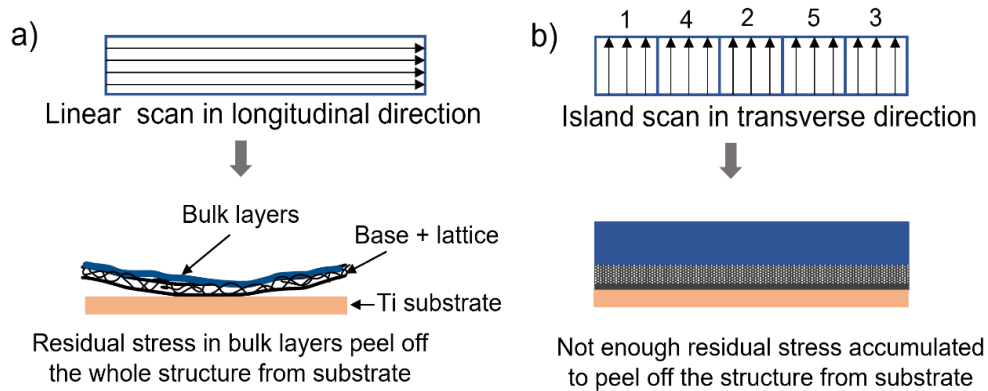


Figure 2.5. a) Linear scanning in longitudinal direction creates higher thermal stress along the scan vector and peels off the structure from substrate. b) Island scanning in transverse direction with non-adjacent strip scan sequence cannot build enough thermal stress to peel off the structure from substrate.

cross section was divided into multiple sub-sections, also known as islands, and the scanning was done in the transverse direction (Figure 2.5(b)). The scanning sequence among the island was set such that any two adjacent islands were not scanned sequentially. This strategy has reduced the residual stress in the longitudinal direction. Since only a small portion of the cross section is scanned at a time, the scan segment is too short to generate residual stress and to peel off the part from the substrate (Figure 2.5(b)). The printed thin tensile coupons using this scan strategy are shown in Figure 2.6(c) and 2.6(d).

#### 2.3.4. Microstructure and composition analysis

The secondary electron (SE) and backscattered electron (BSE) images with the EDS composition analysis of the printed sample are shown in Figure 2.7. Several Ti-rich regions with oxygen content

are observed in the BSE image that was indicated closer to  $Ti_4Ni_2O_x$  in the SEM and EDS analysis (Figure 2.7(c)). Similar Ti-rich oxides were observed by other researchers in the LPBF printed NiTi that was attributed to the high affinity of NiTi to oxygen [29], [59]. Presence of multiple

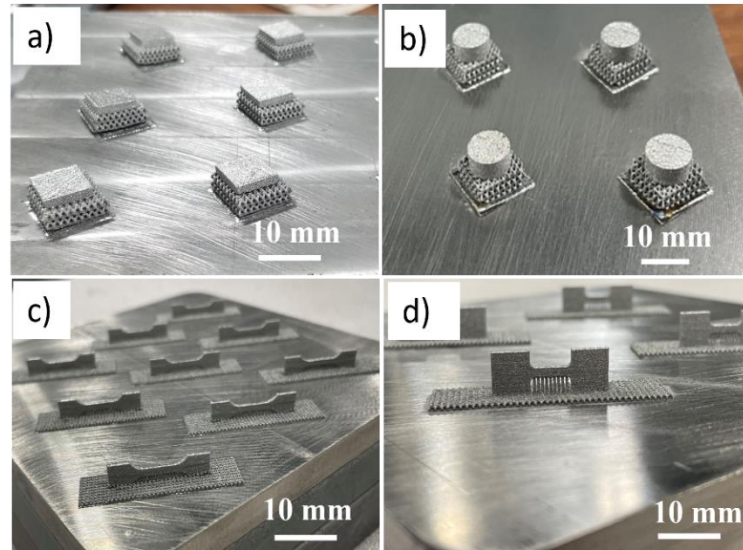


Figure 2.6. Successfully printed NiTi blocks on Ti substrate using the developed printing method. a) square blocks, b) Cylindrical blocks, c) Dog-bone tensile coupon, d) Rectangular tensile coupon.

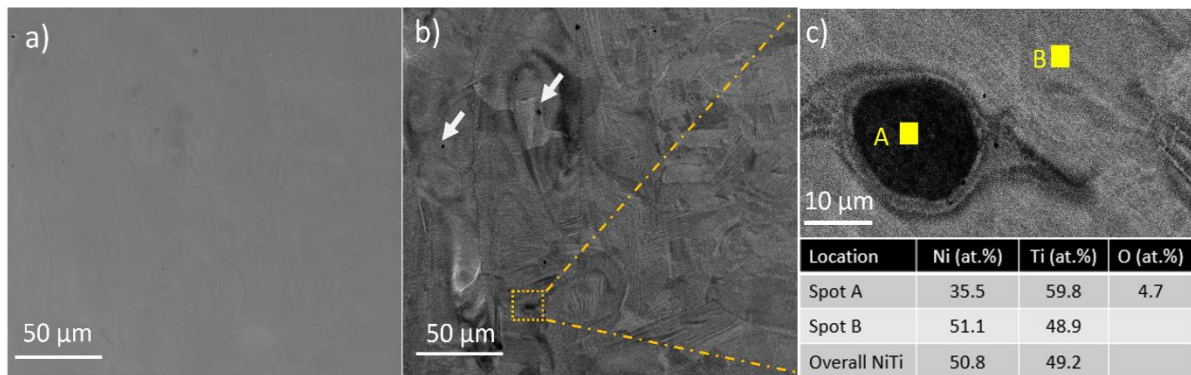


Figure 2.7. a) SE and b) BSE images. White arrows indicate pores. c) magnified BSE image (top) with EDS composition (bottom) shows the Ti-rich region with oxygen content.

porosities in the size between 1 and 3  $\mu m$  are also observed in the image. The porosity may have come from the trapped gas during printing or from the porosity present in the powder. The EDS composition of the overall NiTi is also listed in Figure 2.7(c).

The composition of the printed sample was found to be 55.8 wt.% (50.8 at.%) which is similar to the powder composition. This indicates that the Ni loss by evaporation was minimized by printing with low LED despite of many studies [34], [35], [44] reported on Ni evaporation during NiTi printing. The Ni content in the matrix directly controls the transformation and functional behaviors of the NiTi part. The type and size of precipitation formed during post heat treatment also depends on the Ni content in the matrix [47], [62]. The transformation behavior of the parts undergone excessive compositional change due to Ni evaporation cannot be corrected even by post heat treatment [19]. Therefore, it is important to minimize or avoid any Ni loss during printing. Low LED scanning used in this work did not raise the melt pool temperature high enough for Ni evaporation, especially in the absence of the substrate heating where the cooling rate was faster.

### **2.3.5. Phase transformation behavior**

The DSC plot of the printed NiTi sample in Figure 2.8 clearly indicates the forward and reverse phase transformations with the  $M_s$  and  $A_f$  temperatures of  $-10.3^\circ\text{C}$  and  $2.3^\circ\text{C}$ , respectively. In many studies, the as-printed samples hardly showed clear phase transformation peak in the DSC test due to the severe inhomogeneity and residual stress during printing [29], [30] as well as severe Ni evaporation during printing shifting the phase transformation temperature out of DSC scan range [45], [63]. Compared to the reported results, the DSC phase transformation peaks obtained in this work are clearer and sharper. This can be attributed to the printing method with low LED scanning which reduced the inhomogeneity and Ni evaporation.

Comparing the DSC plots between the as-received powder (Figure 2.2(a)) and the printed NiTi sample (Figure 2.8), the austenite finish temperature ( $A_f$ ) dropped to  $2.3^\circ\text{C}$  from the  $A_f$  of  $32.6^\circ\text{C}$  in the as-received powder, indicating that the Ni to Ti ratio in the NiTi matrix of the printed sample became higher. This happened because of the Ti loss by means of oxidation during printing, as

shown in Figure 2.7(c). The Ti loss by oxidation during NiTi fabrication is widely reported by researchers [29], [59]. Oxidation of Ti starts at 550°C even at very low oxygen level in the built chamber and mainly forms  $Ti_4Ni_2O_x$  in the microstructure [64]. It is known that with increase in the Ni/Ti ratio in the matrix phase, the  $A_f$  temperature decreases [20], [62]. Formation of Ti-rich oxides increases the Ni to Ti ratio in the matrix and consequently reduces the  $A_f$ . However, if the

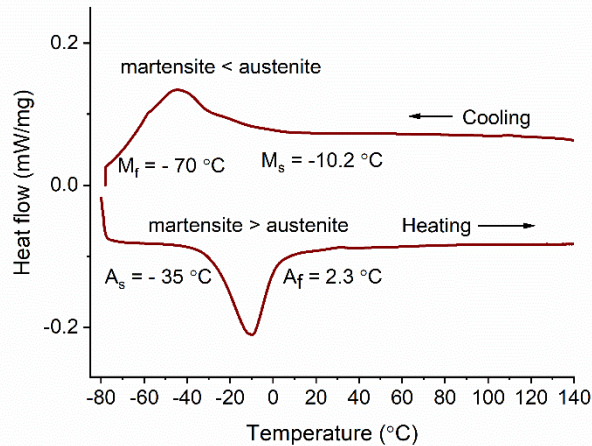


Figure 2.8. DSC plot of the printed NiTi sample. The  $A_f$  and  $M_s$  temperature are recorded as 2.3 °C and -10.2 °C, respectively.

amount and size of oxides formed are below critical levels, the oxides cannot be detected as a separate phase in the XRD [24], [65]. Sometimes, the amount of Ti lost by the oxidation is compensated by the loss of Ni in evaporation. In this study, the Ni loss by evaporation was negligible and the small loss of Ti by oxidation changed the Ni to Ti ratio, which reduced the  $A_f$ , consequently.

### 2.3.6. Phase analysis

Figure 2.9 shows the XRD spectra of the printed NiTi and the as-received powder for the comparison. The XRD spectra of the printed specimen have the intensity peaks at the same angles as the as-received powder indicating the same metallic phases. The as-printed specimen has the

austenite B2 phase at room temperature. The presence of austenite phase in the printed specimen at room temperature is also evident from the cooling curve of the DSC result (Figure 2.8).

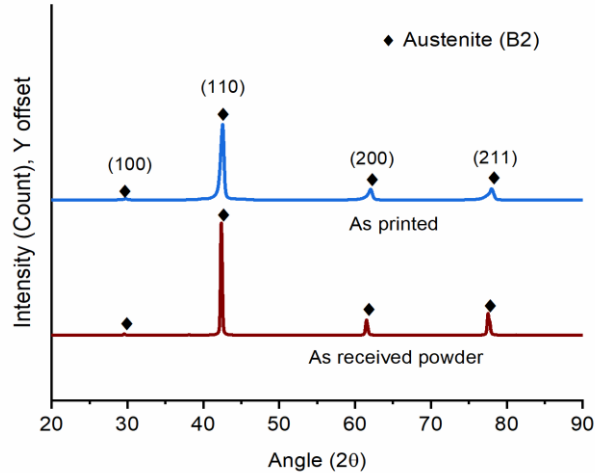


Figure 2.9. XRD spectra of the as received powder and the printed NiTi sample.

It is worth noting that the XRD peaks of the printed specimen are slightly wider, and the intensity of the peaks are also slightly lower than those of the as-received powder because of the minor inhomogeneity and slightly deviated grain orientation in the printed microstructure emanating from the complex thermal history of LPBF. From the XRD spectra, presence of any other secondary phase was not observed because either no secondary phase was formed, or the formed secondary phase was too small to be detected by the XRD. Because these precipitate forms even under the short thermal exposure, it is reported that the LPBF printed NiTi parts mostly come with some newly formed secondary precipitation phases due to the associated complex thermal history during printing [31], [66]. Wang et al. [31] printed NiTi with two different LED of  $80 \text{ J/mm}^3$  and  $130 \text{ J/mm}^3$ . In XRD analysis, they observed the presence of  $\text{Ni}_3\text{Ti}$  in the sample printed with  $80 \text{ J/mm}^3$  while both  $\text{Ni}_3\text{Ti}$  and  $\text{Ti}_2\text{Ni}$  were observed in the sample printed with  $130 \text{ J/mm}^3$ . Biffi et

al. [67] reported that the XRD analysis of the printed samples proved the presence of Ti rich precipitates ( $Ti_2Ni$ ) in the microstructure during printing.

Formation of secondary phases changes the Ni to Ti ratio in the matrix, which affects the transformation behavior and functional properties [30]. In this study, formation of any significant amount of undesirable secondary phase during printing could be avoided by avoiding substrate pre-heating and reducing the melt pool temperature with low LED scanning.

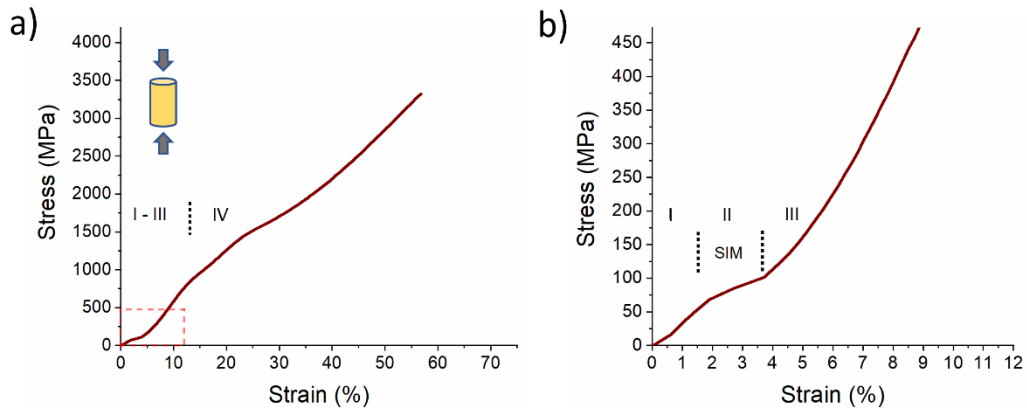


Figure 2.10. (a) Compressive stress strain plot until fracture of the printed NiTi sample, (b) Enlarged view of the initial stress-strain portion showing the stress plateau for the SIM transformation.

### 2.3.7. Stress-strain behavior

The compressive stress-strain plot till fracture is shown in Figure 2.10(a). The enlarged view of the initial portion of the plot is shown in Figure 2.10(b). Figure 2.10(a) shows that the printed sample exhibited an ultra-high fracture strength of 3343 MPa with the fracture strain of 57%. The characteristic stress plateau of the printed NiTi is observed in the enlarged view of the stress-strain plot (Figure 2.10b). The critical stress for martensitic phase transformation was found to be around 75 MPa.

Based on the deformation mechanism, the stress-strain plot in Figure 2.10(a) can be divided into four separate regions (I-IV). The initial linear portion of the plot up to 75 MPa represents the austenitic elastic deformation, which is followed by the stress induced martensitic (SIM) phase

transformation. The strain in SIM associated with reduced stiffness is known as pseudoplastic strain. After the transformation is complete, the martensite deforms elastically with comparatively a higher stiffness followed by the plastic deformation until fracture. The fractured samples were separated in the 45° angles to the loading direction which is the plane of maximum shear stress in compression.

### 2.3.8. Incremental load-unload test

The stress-strain plots of the incremental load-unload tests are presented in Figure 2.11. The applied strain ( $\epsilon_{tot}$ ), irrecoverable strain ( $\epsilon_{irr}$ ), recoverable strain ( $\epsilon_{rec}$ ), and recovery ratio ( $\epsilon_{rec}/(\epsilon_{rec}+\epsilon_{irr})$ ) of the corresponding stress level are listed in Table 2.2. Each sample was loaded to four levels of incremental stresses (75, 150, 275 and 375 MPa) followed by unloading. Table 2.2 extracted from Figure 2.11 shows that both the recoverable strain and recovery ratio have been noticeably increased at a later loading step. The recovery ratio increased from 76% at the loading step I (to 75 MPa) to 92% at loading step IV (to 375 MPa). For the loading step II (to 150 MPa), a clear stress plateau is observed during loading, indicating the SIM. The stress plateau at the loading steps III (to 275 MPa) and IV (to 375 MPa) are observed to be comparatively flatter and shorter than that of the step II (to 150 MPa).

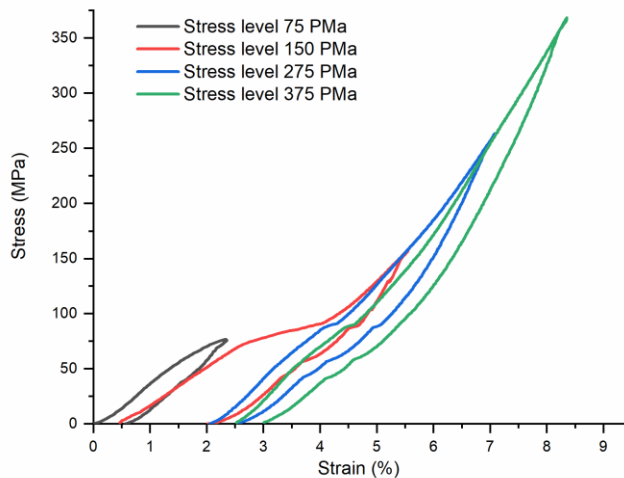


Figure 2.11. Stress-strain plot of the incremental compressive load-unload test.

The loading step I (to 75 MPa) is mainly associated with the elastic deformation of the B2 austenite phase. However, some plastic deformation of the austenite B2 phase could also take place at the first loading step that contributed to developing the residual strain upon unloading (Figure 2.11, stress level 75 MPa). During the loading step II (up to 150 MPa), the sample was exposed to the stress level to complete the martensitic transformation (evident from the stress plateau at the stress level 150 MPa in Figure 2.11). In the later loading steps (275 and 375 MPa), along with the elastic deformation of the austenite and martensitic phase transformation, elastic deformation of the martensite also takes place.

Table 2.2. Applied strain ( $\epsilon_a$ ), irrecoverable strain ( $\epsilon_{irr}$ ), recoverable strain ( $\epsilon_{rec}$ ), and recovery ratio ( $\epsilon_{rec} / (\epsilon_{rec} + \epsilon_{irr})$ ) of the incremental compressive load-unload test of the printed NiTi sample.

Loading steps	Applied stress (MPa)	Applied strain, $\epsilon_{tot}$ (%)	$\epsilon_{irr}$ (%)	$\epsilon_{rec}$ (%)	Recovery ratio (%)
I	75	2.5	0.6	1.9	76
II	150	5.1	1.6	3.5	69
III	275	5	0.5	4.6	90
IV	375	5.8	0.5	5.3	92

### 2.3.9. Superelasticity test

The stress-strain plots as well as the changes in recoverable strain and recovery ratio of the cyclic compression test up to 10 cycles are shown in Figure 2.12. The detailed calculation of the superelastic behavior is listed in Table 2.3. Each sample was exposed to cyclic compression up to a stress of 300 MPa. Figure 2.12(a) shows that the hysteresis of the stress-strain plot significantly decreased with each additional cycle. Especially, the 1<sup>st</sup> cycle associated with very large hysteresis is similar to the behavior observed in the incremental load-unload test in Figure 2.11. The characteristic stress plateau of NiTi is clearly observed in the 1<sup>st</sup> cycle, indicating the SIM. All the cycles except the 1<sup>st</sup> cycle followed almost similar stress-strain paths during the loading-unloading cycle.

No considerable change in the hysteresis area is observed between the 2<sup>nd</sup> cycle and the 10<sup>th</sup> cycle. The similar behavior of the large hysteresis in the 1<sup>st</sup> cycle followed by the reduced hysteresis in the later cycles was also observed by Wang et al. [43] and Yu et al. [68] in the LPBF printed NiTi samples. The hysteresis of the stress-strain plot is an effective measure of

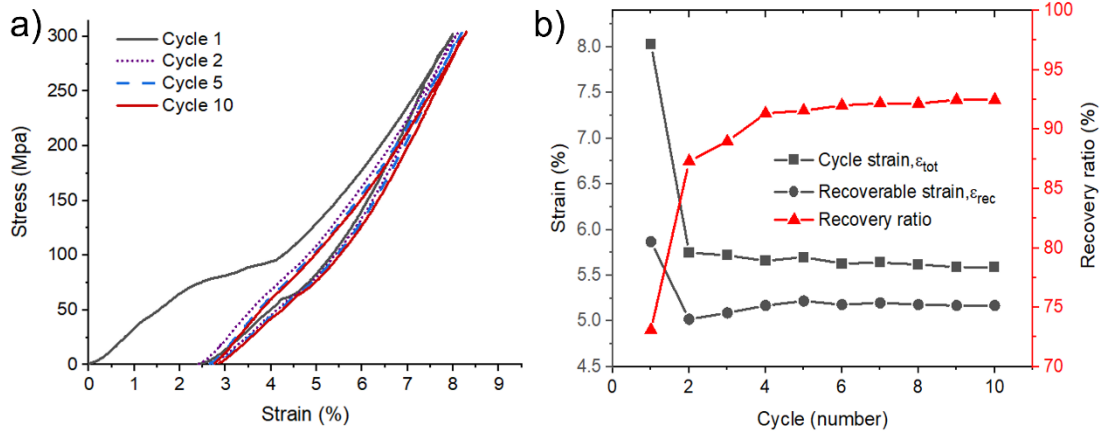


Figure 2.12. (a) Compressive cyclic test of the printed NiTi sample. Only cycles 1, 2, 5 and 10 have been plotted for the easy distinction. (b) Plots showing the total strain, recoverable strain, and recovery ratio of each compressive cycle.

the functional fatigue resistance of NiTi. The narrower hysteresis obtained in the subsequent cycles is an indication of better functional fatigue resistance with stabilized recoverable strain of the printed NiTi samples [43], [68].

Table 2.3. Total strain ( $\epsilon_{tot}$ ), irrecoverable strain ( $\epsilon_{irr}$ ), recoverable strain ( $\epsilon_{rec}$ ), and recovery ratio ( $\epsilon_{rec} / (\epsilon_{rec} + \epsilon_{irr})$ ) of the cyclic compressive test of the printed NiTi sample.

Applied stress (MPa)	1st cycle			10th cycle			
	$\epsilon_{tot}$ (%)	$\epsilon_{irr}$ (%)	Recovery ratio (%)	$\epsilon_{tot}$ (%)	$\epsilon_{irr}$ (%)	$\epsilon_{rec}$ (%)	Recovery ratio (%)
300	8.03	2.16	73.1	5.59	0.42	5.17	92.5

In the 1<sup>st</sup> cycle, the sample was deformed up to the strain of 8.01%, of which 5.62% was recovered (recovery ratio of 73%) upon unloading. The 1<sup>st</sup> cycle ended with the residual strain of 2.16% ( $\epsilon_{irr}$ ), whereas each of the following cycles was associated with noticeably a lower residual strain (0.42%

in the 10<sup>th</sup> cycle) and a higher recovery ratio (92.5% in the 10<sup>th</sup> cycle). The higher recovery ratio (more than 85%) from the 2<sup>nd</sup> cycle is more clearly observed in Figure 2.12(b). This result indicates that the residual strains in the sample at the end of 10<sup>th</sup> cycle were retained mostly from the 1<sup>st</sup> cycle and the residual strain retained in a later cycle is negligible.

The high residual strain at the 1<sup>st</sup> cycle can be attributed to the remnant plastic deformation of the austenite phase and remnant martensite phase that limited the complete strain recovery upon unloading. [43], [47], [69]. At a later cycle, the imposed stress mainly induced the elastic deformation in the B2 austenite phase, austenite to martensite phase transformation, and elastic deformation in the remnant martensitic phase. The later cycles are rarely associated with plastic deformation and newly formed remnant martensitic phase. Consequently, most of the strain at the later cycles could be recovered upon unloading.

This work represents the first attempt to print NiTi on Ti substrate and without pre-heating. The superelastic property obtained in this study is comparable and even better than the reported results for the printed NiTi sample on a NiTi substrate. Saedi et al. [47] printed NiTi with 55.5 J/mm<sup>3</sup> energy density on a NiTi substrate and reported its superelasticity with a recovery ratio of 32.9%. Severe plastic deformation along with the formation of micro defects upon loading were mentioned as the reason for such low recoverable strain. Wang et al. [43] printed NiTi with three different substrate heating of 150 °C, 250 °C and 350 °C, and reported maximum of 57.3% strain recovery ratio in the compressive load-unload test. Formation of large precipitation particles due to the substrate pre-heating was attributed to limiting the phase transformation leading to poor strain recovery.

### 2.3.10. Grain orientation observation

The inverse pole figure (IPF) grain mapping and corresponding pole figure generated from the EBSD of the printed NiTi sample are shown in Figure 2.13. The EBSD was performed on the

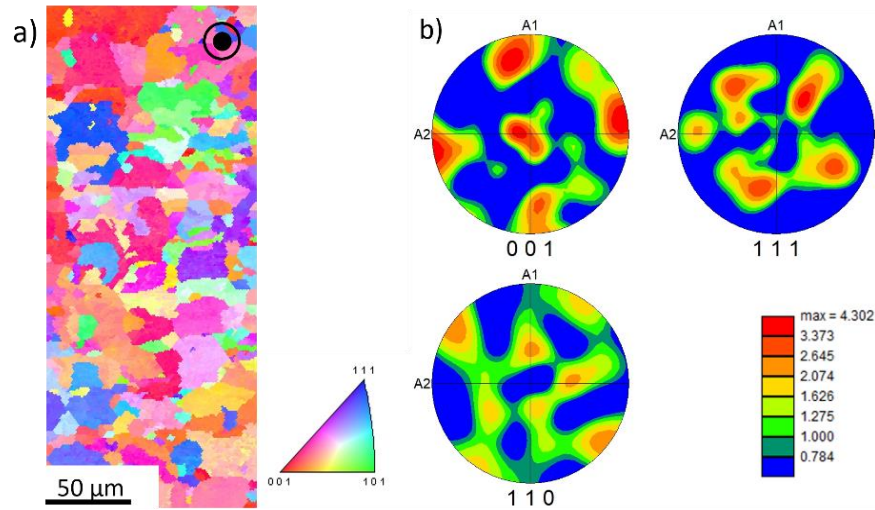


Figure 2.13. EBSD of the printed NiTi sample. The EBSD was taken on a cross section perpendicular to the BD. a) Inverse pole figure with colored grain mapping, and b) corresponding pole figure.

surface perpendicular to the build direction (BD). The IPF mapping in Figure 2.13(a) shows that most of the austenite B2 grains are orientated along [001] direction. The pole figure in Figure 2.13(b) shows that the printed sample has slight preference along the [001] orientation parallel to the BD. It is observed from the pole figure that the [100] and [010] directions are oriented along the laser scanning directions (Figure 2.13(b)).

It is well known that microstructure and crystallographic texture play an important role in the mechanical and superelastic properties of NiTi. The critical stress for martensitic transformation in compressive loading is lower along the [001] crystallographic direction [36], [69]. The better superelastic property could be attributed to the printed samples having most of the grains oriented along the [001] direction which was loaded in the compressive direction in our experiments.

## 2.4. Effect of LPBF parameters on the crystallographic texture

In the cubic-structured materials, [001] is the fastest growing crystallographic direction along the highest thermal gradient during solidification [70]. In a certain combination of laser scanning parameters, the highest thermal gradient during the solidification can be tailored to be parallel to the BD which ultimately leads to grow the grains preferentially along the [001] direction. Xue et al. [38] have discussed the effect of laser energy density as well as the hatch spacing on achieving the [001] crystallographic direction parallel to the BD. Very high laser energy density (high power or low speed) forms keyhole shape (narrower and deeper) melt pool with the highest thermal gradient deviated from parallel to the BD (Figure 2.14(a)). On the other hand, a lower energy density forms comparatively shallower melt pool with flatter bottom. This type of melt pool geometry has the highest thermal gradient parallel to the BD (Figure 2.14(a)).

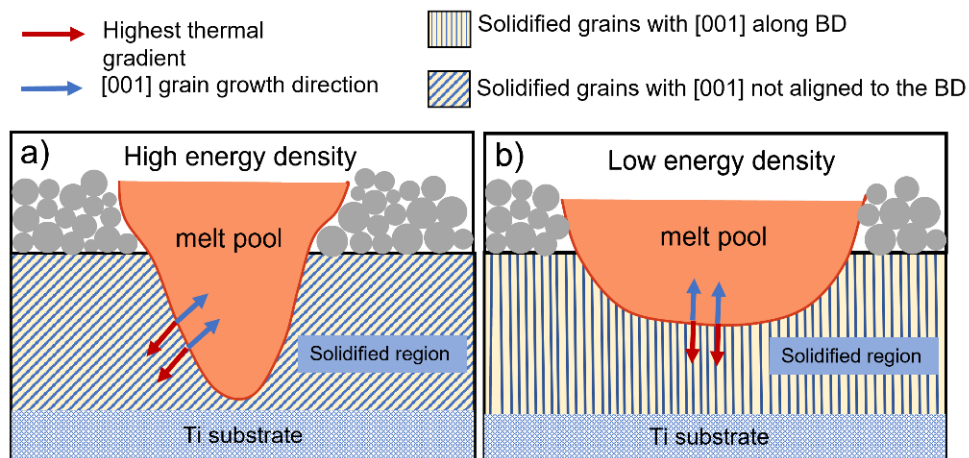


Figure 2.14. Schematic illustration showing a) High energy density laser scanning form deep keyhole shape melt pool where the highest thermal gradient and [001] are not along BD. b) In low laser energy density scanning, the highest thermal gradient along the BD and the [001] grains grow parallel to BD.

However, to achieve proper epitaxial growth along the full height of the sample, the previously solidified layer needs to be partially melted and regrown along the preferred crystallographic direction [30], [50]. The direction of the highest thermal gradient is also a function of substrate

material and the composition of the NiTi powder used in printing. Therefore, it is necessary to study many combinations of scanning parameters for a particular substrate and NiTi composition to achieve the desired crystallographic texture to accomplish near full superelasticity in the printed NiTi parts.

The samples in this study were fabricated using very low energy densities which probably facilitated with a shallower and flatter melt pool. This led the solidification to occur preferentially along the [001] direction. Yang et al. [71] fabricated various NiTi samples with changing laser speed and concluded that the strong [001] crystallographic texture along the BD was mostly obtained with higher scanning speed. The laser scanning speed used in this study was very high (1900 mm/s) which has contributed to achieving a larger number of [001] oriented grains parallel to BD. However, the crystallographic texture obtained is still not perfectly along [001] direction. The IPF of the EBSD shows the presence of many [111] oriented grains along the BD (Figure 2.13(a)). The critical stress for SIM in compression is comparatively higher for the [111] direction. As a result, in these grains, the critical stress for plastic deformation could be lower than the SIM, and these grains were deformed plastically (and irreversible) before transforming into the martensitic phase. This can be attributed as the reason for high residual strain in the 1<sup>st</sup> cycle in the cyclic compression test (Figure 2.12(a) and 2.12(b)). With the grains mostly along [001] direction, the recoverable strain obtained is still significantly higher than the irrecoverable strain. After the 1<sup>st</sup> cycle, the [001] oriented grains mostly showed full strain recovery with very negligible residual strain (Figure 2.12(b)).

## **2.5. Effect of chamber oxygen level on the printability and phase transformation behavior**

High oxygen affinity of NiTi has always been a major challenge in fabricating NiTi in conventional manufacturing process. In this work, the effect of the chamber oxygen level on the printability and

transformation behavior of the NiTi has been investigated. In this regard, NiTi samples were printed in the oxygen levels of 1500 ppm, 1200 ppm and 300 ppm while keeping all the printing strategy and parameters the same. However, with the oxygen level of 1500 ppm, printing could not be continued beyond the first few layers due to severe oxidation issues. The DSC result of the NiTi samples printed in 1200 ppm (S-1200) and 300 ppm (S-300) shown in Figure 2.15(a) clearly indicates that the transformation peaks for the S-300 sample are clearer and sharper than those of the S-1200 sample. The forward transformation peaks in the S-1200 sample are hardly observed, whereas the S-300 sample showed one clear step-forward transformation during cooling. The  $A_f$  temperature of the S-1200 sample ( $A_f = -3.4^\circ\text{C}$ ) also shifted downward by  $5.7^\circ\text{C}$  in compared to that of S-300 sample ( $A_f = 2.3^\circ\text{C}$ ).

The XRD phase analysis result of the S-300 and S-1200 samples are shown in Figure 2.15(b) which shows that the S-1200 sample contains Ti-rich oxides ( $\text{Ti}_4\text{Ni}_2\text{O}$ ).

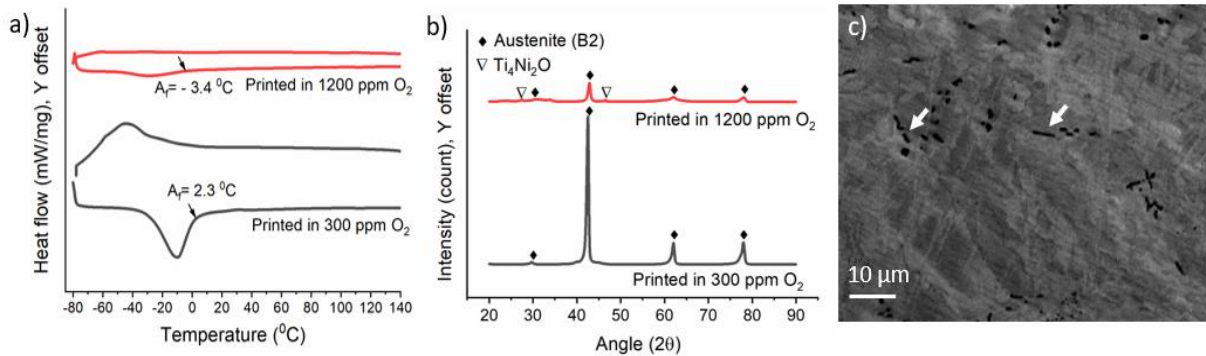


Figure 2.15. a) DSC phase transformation plot and b) XRD plots showing the phases of NiTi samples printed in a printing chamber with oxygen level of 300 ppm and 1200 ppm respectively. c) BSE image of the sample (S-1200) printed in 1200 ppm oxygen chamber shows the Ti-rich oxides  $\text{Ti}_4\text{Ni}_2\text{O}$  indicated with arrow.

The peak intensities of the B2 austenite phase in S-1200 sample are considerably lower than the corresponding B2 austenite peaks in the S-300 samples. The BSE image of the S-1200 sample is shown in Figure 2.15(c) that shows the presence of the Ti-rich precipitate randomly oriented in the

microstructure. With high oxygen level in the printing chamber, a higher amount of Ti was lost by oxidation due to the formation of Ti-rich oxides. This increased the Ni/Ti ratio in the matrix phase that consequently reduced the  $A_f$  temperature of S-1200 sample. The presence of such oxide particles in the microstructure also restricts the regular phase transformation during thermal cycles. As a result, phase transformation happens in a wider range of temperatures that make the

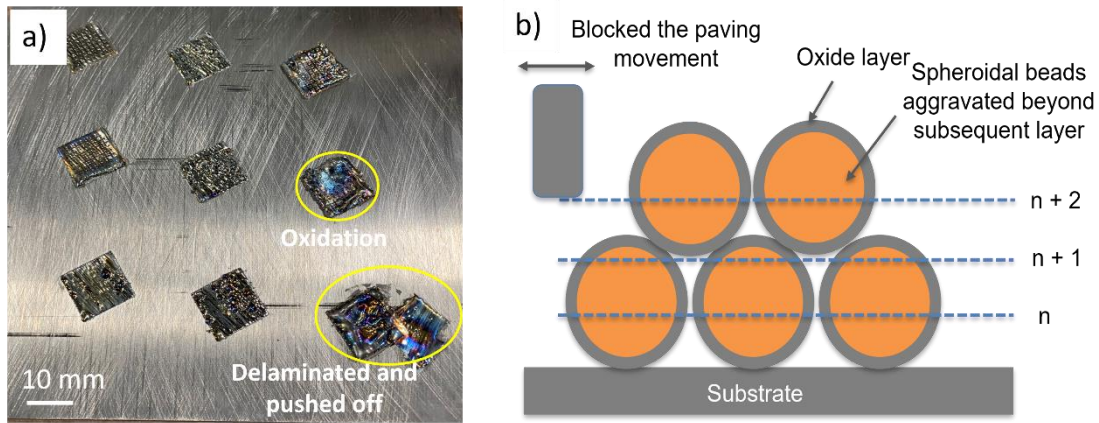


Figure 2.16. a) The oxidation experienced in a chamber with 1500 ppm oxygen level. b) Schematic representation of the rough surface formed by the oxidized spheroid beads and the paving jam.

transformation peak shallower and wider, which is evident in Figure 2.15(a). For the printing attempt in the 1500 ppm oxygen level, the NiTi melt pool was exposed to severe oxidation and formed spheroidal metallic beads due to the poor wet issue. This made the sintered surface rough and obstructed the continuous rake movement. Within a few layers of printing, the metallic beads aggravated to extend beyond the subsequent layer and blocked the powder spreading mechanism. Interlayer delamination was also experienced during 1500 ppm printing attempt due to the presence of oxide film that limited the interlayer bonding. Similar phenomena due to oxidation were also reported for stainless steel and nickel based alloy by Yap et al. [72]. The impact of oxidation during printing is depicted in Figure 2.16(a) and 2.16(b).

## 2.6. Conclusion

A multistep printing method has been developed, which enabled printing NiTi on a Ti substrate and without any substrate heating for the first time. The NiTi samples were printed with a very low energy density without any visible delamination or cracking. The microstructure, grain orientation, transformation behavior, mechanical and superelastic properties of the printed NiTi sample have been evaluated and analyzed. The following statement can be concluded from the work:

- I. Because of the poor bonding and high residual stress, it is challenging to print NiTi in LPBF on a Ti substrate. A multi-steps printing method including the high laser energy bottom layers and the mediating lattice structure was developed before printing NiTi samples. The high energy bottom layer served to keep the printed part bonded to the substrate, the lattice structure assisted with reducing the built-in residual stress and warping phenomena during solidification.
- II. Using the low laser energy density (at 35 J/mm<sup>3</sup>), the widely reported Ni evaporation and precipitation phase formation issue during printing was avoided and the printed samples retained the same composition and phases as the as received powder.
- III. In the cyclic compression test, the printed samples showed superelasticity with a recovery ratio of 73.1% in the 1<sup>st</sup> cycle and 98.9% in the 10<sup>th</sup> cycle from an applied strain of 8.03% respectively. The reduced hysteresis after the 1<sup>st</sup> cycle indicated good fatigue resistance of these samples.
- IV. The EBSD analysis showed the majority of [001] // B2 austenite grains along the BD. The comparatively shallower and flatter melt pool obtained by using low laser energy density

is attributed to achieving strong [001] grains in the build direction, which facilitated with excellent superelasticity obtained in this work.

- V. The sample printed in a chamber of higher oxygen level (1200 ppm vs. 300 ppm) showed reduced  $A_f$  temperature ( $-3.4^\circ\text{C}$  vs.  $2.3^\circ\text{C}$ ) with shallower and wider phase transformation peaks. With a higher oxygen level in the printing chamber, Ti-rich oxides form in the microstructure and reduces the  $A_f$  temperature. Printing in a chamber of 1500 ppm oxygen could not be continued because of severe oxidation. The study indicates that maintaining low oxygen level is important to attain smooth NiTi printing and expected phase transformation properties.

## **Chapter 3: Developing the Post Heat Treatment Protocol for the Biomedical Applications**

### **3.1. Introduction**

Due to the change in composition and constituent phases occurring during printing and the microstructural inhomogeneity in the printed parts, obtaining a desired set of phase transformation behaviors and superelastic properties in the as printed part is a major challenge. Post heat treatment is the only viable method to modify the phase transformation and mechanical properties of the printed NiTi.

This chapter was designed to develop the heat treatment cycles for the LPBF-printed NiTi while achieving the desired phase transformation temperature as well as improved superelasticity required for the biomedical applications. The post heat treatment cycles were systemically studied to explore the appropriate protocol such that the  $A_f$  temperature of the printed sample would be tailored slightly below the body temperature. The phase transformation, phase constituent, and the microstructural changes upon heat treatment have been thoroughly investigated to obtain the desirable ranges of mechanical and superelastic properties for biomedical applications in the final NiTi samples.

### **3.2. Materials and method**

#### **3.2.1. Printing**

The sample was fabricated following the multi-steps printing method developed using the same NiTi powder and the printing machine mentioned in Chapter 2. was used to fabricate the NiTi sample for the heat treatment study. The printing parameters used are shortly listed in Table 2.1.

Table 3.1. LPBF parameter used to print the NiTi samples.

Laser power (W)	speed (mm/s)	Hatch ( $\mu\text{m}$ )	Layer thickness ( $\mu\text{m}$ )	Volume energy density ( $\text{J}/\text{mm}^3$ )
150	1900	50	45	35

### 3.2.2. Heat treatment

Heat treatment of the printed NiTi samples was performed in a tube furnace (Thermo-Scientific Lindberg Blue M, Asheville, North Carolina, USA) while continuously flowing Argon (Ar) gas (Figure 3.1). Each sample was inserted in the furnace after preheated to the desired temperature and cooled by quenching in water at room temperature.

The printed samples were first solution treated at 900 °C for 1 hour to homogenize their microstructure. The temperature for the solution treatment was chosen to ensure dissolving of any secondary phases present as well as to avoid excessive grain coarsening [19], [62]. The solution treated samples were then aged at 350 °C and 450 °C for holding time of 15 minutes, 30 minutes, 1 hour, 4 hours, and 8 hours, respectively. These holding temperature and time were chosen based on the prior trials in purpose to accomplish the desired phase transformation behavior while minimizing the holding time. Aging at a lower temperature (such as 300 °C) was found to be too insensitive while aging at a higher temperature (such as 550 °C) was found to be too sensitive to control the phase transformation temperature to a desired level.

Based on this study, the solution treatment at 900 °C for 1 hour followed by aging treatment at 450°C for 30 minutes was found to achieve the desired phase transformation behavior with the  $A_f$  temperature slightly below the body temperature. Detailed study on the microstructural,

mechanical, superelastic performance of these samples were performed. From this point, the aged sample will indicate the sample with the aging treatment at 450°C for 30 minutes.

### 3.2.3. Experimental procedure

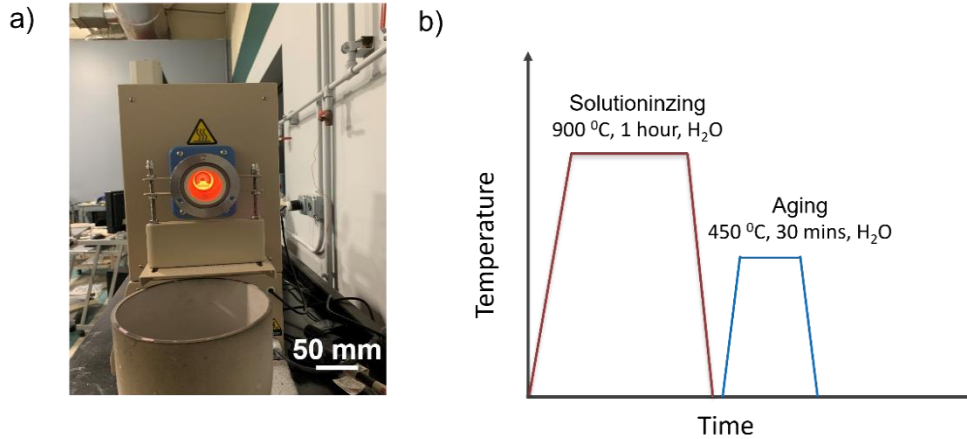


Figure 3.1. a) Tube furnace setup for heat treatment and quenching, b) The heat treatment cycles that provided with desired phase transformation behavior.

The DSC, XRD, SEM, EDS and BSD were performed in the sample instrument mentioned in Chapter 2. The transmission electron microscopy (TEM) was performed for the advanced investigation of the phases and precipitates present in the heat-treated samples. TEM was performed at 200kV in F200X G2 S/TEM manufactured by Thermo Fisher Scientific (Waltham, Massachusetts, USA). The 20  $\mu\text{m}$  sample was cut out and observed at 30 kV for TEM using Helios G4 PFIB UXe manufactured by Thermo Fisher Scientific. A double tilt holder was used to tilt the sample to different zone axis. Scanning transmission electron microscope (STEM) was used at an accelerating voltage of 200 kV. STEM High-angle annular dark-field imaging (HAADF) as well as the EDS were also used to map the chemical composition of the precipitates.

One-way and cyclic compression tests of the printed samples were performed in a uniaxial load frame by United Calibration Corporation (Model SFM-20) in displacement control with a load cell

of 20 KN and at strain rate of 0.5 mm/min at room temperature. The load vs displacement data obtained from the test was converted to strain vs. stress data using the following formula.

$$\text{Strain} = \frac{\text{Change in height}}{\text{Initial height}}$$
$$\text{Stress} = \frac{\text{Load}}{\text{Cross sectional area}}$$

The uniaxial and cyclic compressive tests were performed in the sample load frame at body temperature of 37 °C. Vickers microhardness (HV) measurements were performed to investigate the change in hardness measurement under various processing conditions using a microhardness tester CM-800AT manufactured by Clark (Novi, Michigan, USA) at a load of 100 gf with a dwell time of 15 second. At least three measurements were taken from each sample to get an average hardness value.

### **3.3. Results**

#### **3.3.1. Phase transformation analysis**

Figures 3.2(a) and 3.2(b) show the DSC phase transformation plots of the solutionized NiTi sample after aging treatment at 350 °C and 450 °C for various holding times. The AP sample showed distinct phase transformation peaks during cooling (austenite to martensite) and heating (martensite to austenite). The  $A_f$  temperature of the AP sample was noted as 2.1°C. Comparing with the as-received NiTi powder, the  $A_f$  temperature of the AP sample was dropped by 30.5°C (from 32.6°C to 2.1 °C). Unlike the two-step forward phase transformation in the as-received powder, the AP sample showed one-step forward phase transformation. After the solution treatment, the  $A_f$  temperature was increased to 6.8°C. With the subsequent aging treatment on the ST sample, the  $A_f$  temperature is observed to increase with the holding time. For instance, aging at 450 °C for 15 minutes, 1 hour, and 4 hours shifted the  $A_f$  temperature of the solutionized sample

to 15 °C, 38 °C, and 45 °C, respectively. This is due to the formation of Ni-rich secondary phase that depletes the Ni content in matrix and increases the  $A_f$  temperature [65], [73]. The DSC results also show that the phase transformation peak for the sample aged at 450 °C is more distinct in comparison to the sample aged at 350 °C. Among the aging cycles, aging at 450 °C for 30 minutes provided the narrowest and most distinct martensitic phase transformation peaks with the  $A_f$  temperature slightly below the body temperature, recommended for the biomedical applications [12], [74], [75].

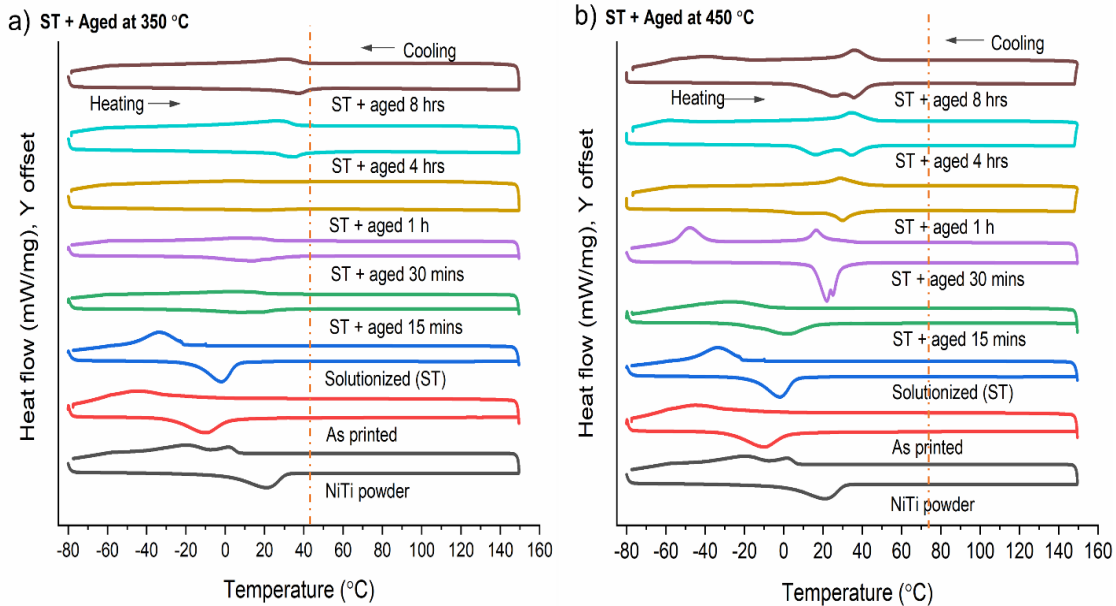


Figure 3.2. DSC phase transformation plot of the solution treated sample aged at a) 350 °C and b) 450 °C at various holding times. The vertical lines at 37 °C present the body temperature.

This ensures that the NiTi sample is completely in the austenite phase before placing inside the body. The phase transformation behaviors obtained by other aging cycles are not appropriate due to either the  $A_f$  temperature higher than the body temperature or the undistinguishable phase transformation peaks. In-depth microstructural analysis as well as the mechanical and superelastic properties at body temperature of the sample aged at 450 °C for 30 minutes have been discussed

in the following sections. From now on, the aging treatment here will indicate aging at 450 °C for 30 minutes.

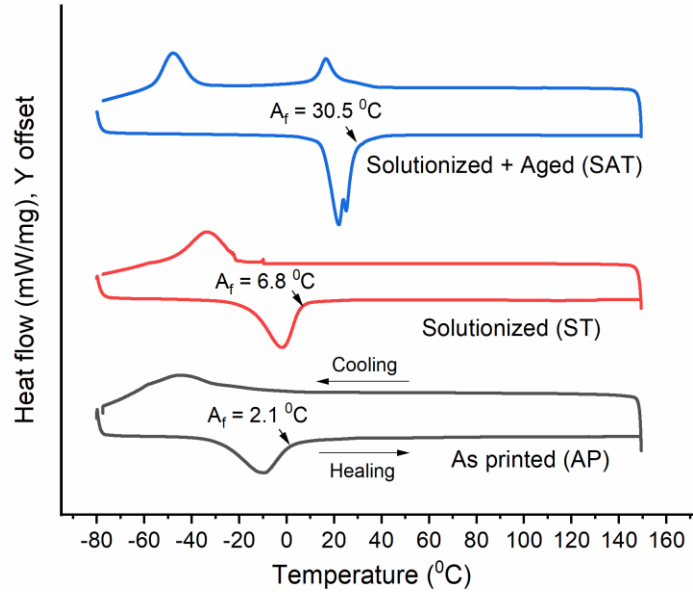


Figure 3.3. DSC phase transformation plot of as printed, solutionized and aged sample at 450 °C for 30 minutes.

The DSC phase transformation plots of the AP, ST, and solution treatment followed by 450 °C, 30 minutes aged (SAT) samples are separately plotted in Figure 3.3. In comparison to the AP and ST samples, the narrower phase transformation peak in the SAT sample (Figure 3.3) indicates that the martensite to austenite phase transformations in the SAT samples occurred within a shorter range of temperature. Unlike the AP and ST samples, the SAT sample also showed two-step martensitic phase transformation. Presence of ultrafine and coherent  $\text{Ni}_4\text{Ti}_3$  precipitate in the microstructure was attributed as one of the main reasons for the two-steps phase transformation which is also known to reduce the plastic deformation and improve the superelastic response in NiTi [24], [76].

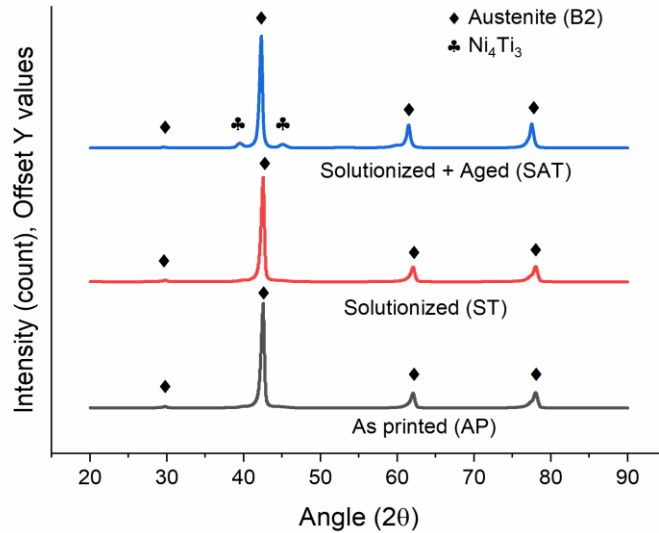


Figure 3.4. XRD spectra of the AP, ST, and SAT sample.

### 3.3.2. Phase analysis

The XRD spectra of the AP, ST, and SAT samples are shown in Figure 3.4. The AP sample provided distinct and strong diffraction peaks for the B2 austenite phase. Other secondary precipitation phases in the AP sample were not detected by the XRD, which suggests that no other secondary phases were formed during printing, or their content is too small to be detected by XRD. After the solution treatment, the major phase constituents did not change based on the XRD analysis of the ST sample as shown in Figure 3.4. After solution and aging treatment, the XRD of the SAT sample clearly showed the presence of Ni-rich precipitation phase, Ni<sub>4</sub>Ti<sub>3</sub>, in Figure 3.4.

### 3.3.3. Microstructure and composition analysis

The EBSD images of the AP sample are shown in Figure 3.5. Figure 3.5(a) shows that the microstructure of the AP sample is characterized by the compositional inhomogeneity, and the rectangular laser scan pattern with the side equal to the hatch spacing of 50 μm used in printing. Several irregular shaped Ti-rich regions were observed with significant oxygen content in the AP sample, as found in the EDS analysis (Figure 3.5(b)). This may have taken place due to the non-

homogeneous compositional distribution during fast cooling as oxygen reacts with Ti. The overall composition of the AP sample (see Figure 3.5(b), overall NiTi composition) matches the as received powder with 50.6 at.% of Ni and 49.4 at.% of Ti, which implies that the low LED avoided the Ni loss by evaporation during printing.

The BSE images of the ST and SAT samples are shown in Figure 3.6. The solution treatment homogenized microstructures form nearly equiaxed grains as observed in the BSE image of the ST sample (Figure 3.6(a)). The irregular Ti-rich region with oxygen content observed in the AP sample disappeared in the ST sample. However, the randomly distributed  $Ti_4Ni_2O_x$  inclusions of about 100 nm length were observed in the ST microstructure. The STEM-HAADF images as well as the associated composition color mapping of these inclusions are shown in Figure 3.6(b).

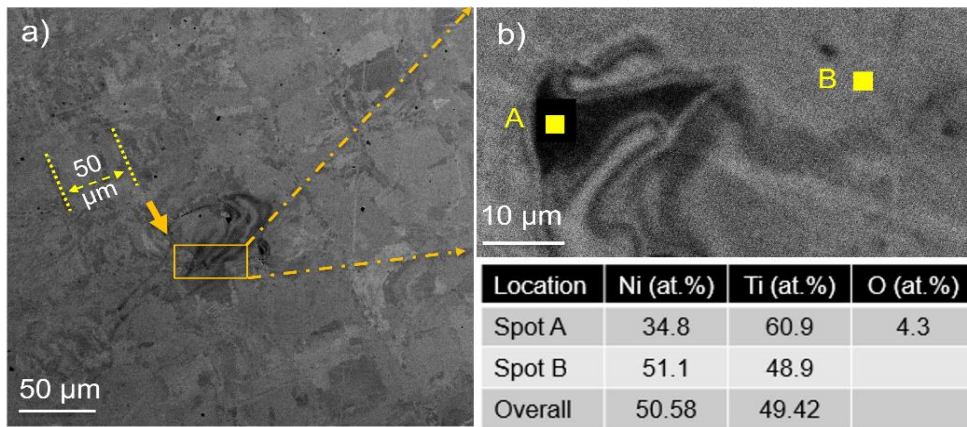


Figure 3.5. BSE-SEM image of a) AP sample. The orange arrow indicates the Ti rich region., b) Magnified view of the Ti-rich region (top) and EDS composition analysis (bottom).

The Ti rich region or Ti-rich inclusion in AP or ST sample were not detected in the XRD analysis (Figure 3.3) as a separate phase, which indicates the insignificant presence of such phase in the attained microstructure. Due to the high affinity to oxygen, formation of Ti rich oxides in the AM processed NiTi is very widely reported. Similar Ti-rich oxide inclusions were also observed by other researchers in the LPBF processed NiTi, which was attributed to the presence of oxygen in

the printing chamber [38], [77], [78]. However, the presence of finer Ti rich oxide inclusions reduces the  $A_f$  temperature because of the depleted Ti in the matrix but is not attributed to affect the superelastic response [73], [79].

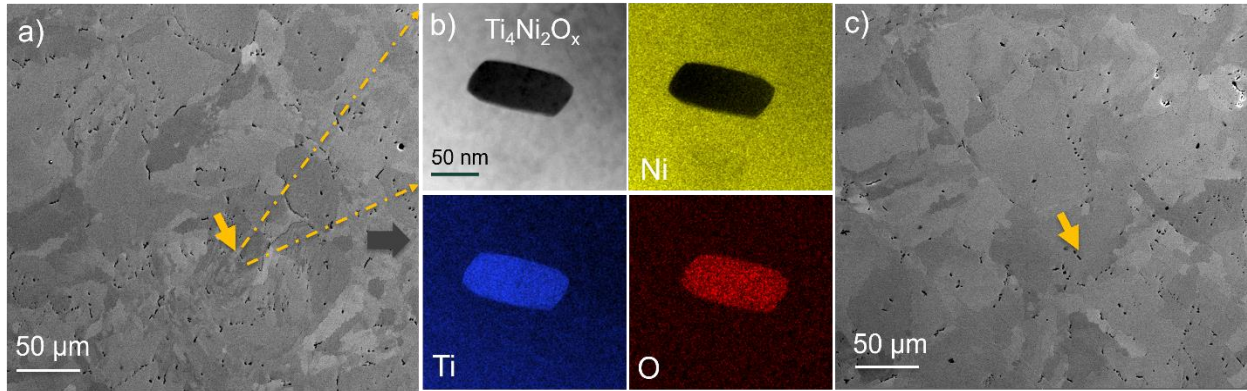


Figure 3.6. a) BSE-SEM image of solution treated (ST) sample. B) STEM-HAADF image and the associated EDS map of the Ti-rich oxide in the ST sample, c) BSE-SEM image of the solution and age treated (SAT) sample. The orange arrow in image a and c indicates Ti-rich oxides ( $Ti_4Ni_2O_x$ ).

The SAT sample did not show any further change in the microstructure based on the SEM analysis (Figure 3.6(c)). The TEM bright field imaging as well as the selected area electron diffraction (SAED) analysis of the SAT sample detected the presence of  $Ni_4Ti_3$  in the microstructure. The dark contrast in the bright field TEM image (Figure 3.7(a)) indicates the presence of high density and uniformly distributed ultrafine Ni-rich precipitate,  $Ni_4Ti_3$ . The SAED pattern of the SAT sample in Figure 3.7(b) shows that the brightest spots in the hexagonal pattern represent the cubic NiTi  $\langle 110 \rangle$  matrix. The satellite spots around each brightest spot are from  $Ni_4Ti_3 \langle 001 \rangle$  with two different orientations overlapped together on top of the NiTi. The faint spots at  $1/3 \langle 110 \rangle$  between the brightest spots indicate the R-phase because the lattice parameter of R-phase is  $1/3$  of that of the B2 austenite phase. Similar diffraction pattern in the NiTi indicating the presence of  $Ni_4Ti_3$  and R-phase was also observed by other researchers [80], [81], [82]. This supports the DSC plot of the SAT sample (Figure 3.3) where two-step phase transformations (austenite to R-phase and to

martensite) were observed during cooling with the  $R_s$  (R-phase start) temperature at 34 °C indicating the presence of R-phase at room temperature.

The inverse pole figure (IPF) grain mapping as well as the pole figure (PF) of the AP and SAT samples are shown in Figure 3.8. The IPF and PF images of the AP sample showed comparatively

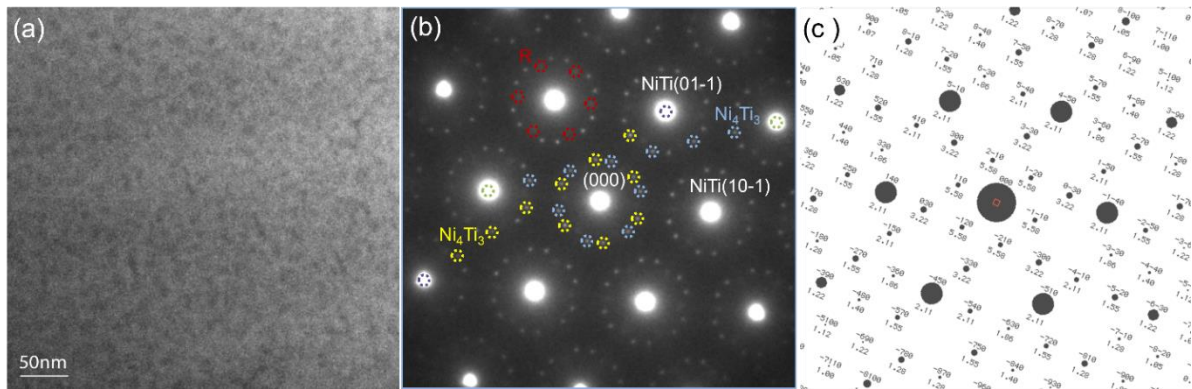


Figure 3.7. (a) Bright field TEM image of SAT sample shows Ni-rich precipitate, (b) Selected area electron diffraction (SAED) pattern along NiTi  $\langle 111 \rangle$ . The bright spots are from NiTi. The satellite spots are diffractions from  $Ni_4Ti_3$  labeled with yellow and blue dashed circles, respectively. Very faint diffractions labeled with red dashed circles are from R phase. (c) Simulated electron diffraction of  $Ni_4Ti_3$ .

preferred [001] orientation along the building direction, whereas the images of the SAT sample showed comparatively random orientation indicating more isotropic microstructure.

The incomplete and sub-grains, with low-angle grain boundaries, observed in the AP sample grew and coalesced to form larger and regular sized grains with high-angle grain boundaries in the SAT sample. The grain size distribution and the grain boundary misorientation angles of the AP and SAT samples are shown in Figures 3.9(a) and (b), respectively. The grain size plot in Figure 3.9(a) shows the increased number of larger grains in the SAT sample indicating the resultant grain coarsening during the heat treatment. The fraction of high-angle grain boundaries has also increased in the SAT sample in comparison to the AP sample, as evident from Figure 3.9(b).

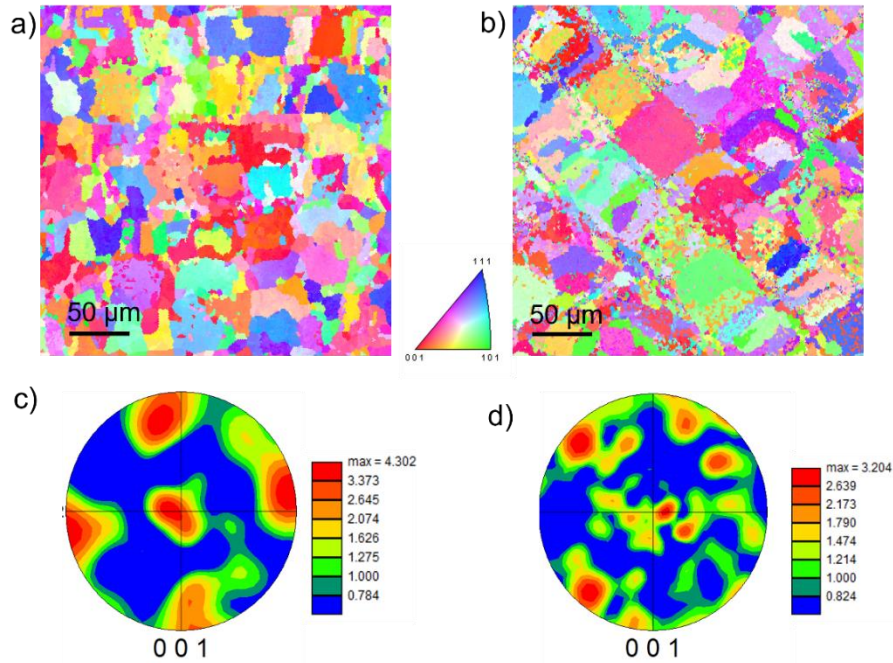


Figure 3.8. Inverse pole figure (IPF) of a) AP) and b) SAT samples and corresponding pole figure (PF) of c) AP and d) SAT sample.

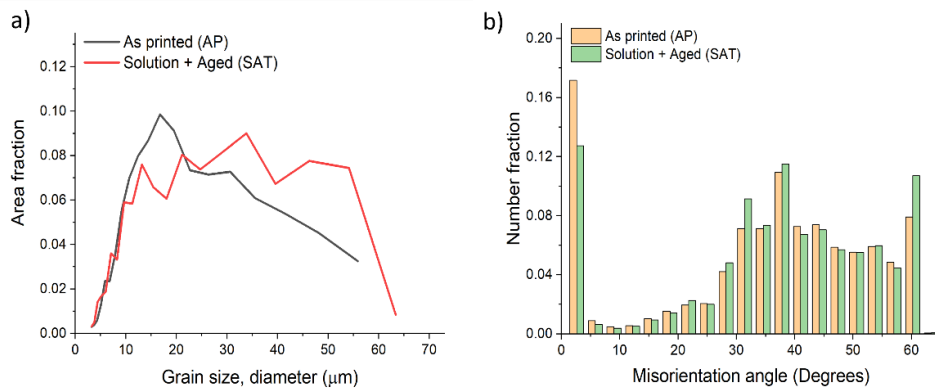


Figure 3.9. a) Grain size (diameter) b) misorientation angle of the AP and SAT.

It is noted that the grain coarsening and re-orientation taken place during the solution treatment, whereas the aging treatment only created the  $\text{Ni}_4\text{Ti}_3$  precipitate in the microstructure without any further change in the grain morphology.

### 3.3.4. Compressive and superelastic properties

The stress-strain curves of the AP, ST, and SAT samples from the compressive test are shown in Figure 3.10. The AP sample demonstrated a fracture strength of 3343 MPa and fracture strain of 57%. In the ST sample, the stiffness slightly decreased while the elongation before fracture increased to the strain of 66% (Figure 3.10(a)). The SAT sample showed the lowest elongation before fracture among all three samples. Upon loading, the austenite NiTi deforms in four consecutive steps, (1) elastic deformation of austenite, (2) stress induced martensitic (SIM) transformation, (3) elastic deformation and (4) plastic deformation of martensite until ultimate fracture. In all three samples, the stress plateau representing the SIM transformation is clearly observed (Figure 3.10(b), a comparatively flatter portion of each stress-strain curve around 100 MPa). However, the stress plateau in the SAT sample is flatter and shorter indicating smoother martensitic phase transformation.

The stress-strain plot of the cyclic compressive test of AP and SAT samples at body temperature are shown in Figure 3.11. The superelastic properties are compared in Table 3.2. The cyclic test result of the ST sample was not presented to focus on the comparison of the AP and SAT samples.

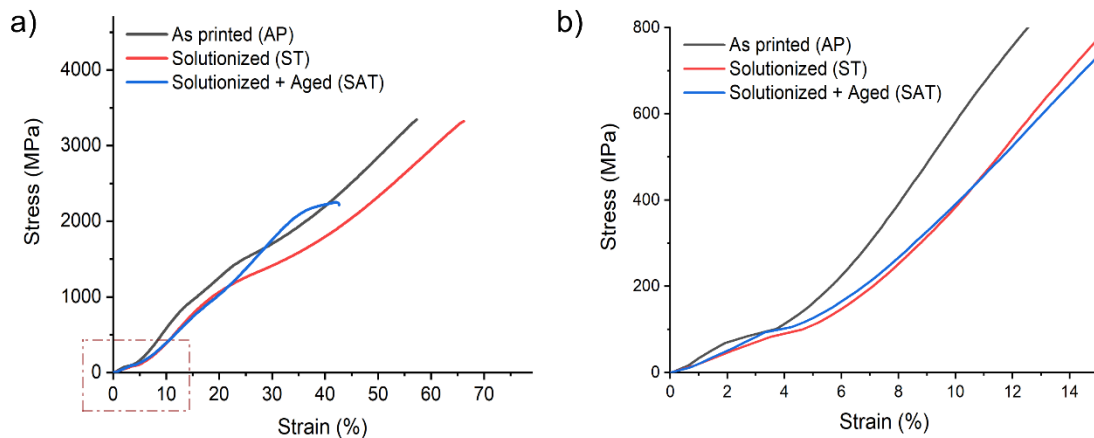


Figure 3.10. a) Compressive stress strain plot of the AP, ST, and SAT sample at body temperature (37 °C). b) enlarged view of the initial portion of the plots.

Figure 3.11 shows that the critical stress for the martensitic phase transformation is higher for the SAT sample (100 MPa) than the AP sample (72 MPa). In comparison to the AP sample, the SAT sample demonstrated narrower stress-strain hysteresis. However, both types of the samples showed larger hysteresis and lower strain recovery ratio in the first cycle in comparison to the subsequent cycles. Other researchers [43], [68] also found the similar result of higher hysteresis and lower recovery ratio at the first cycle in the LPBF printed NiTi. This was attributed to the partial plastic deformation and remnant martensitic variant that did not completely reverse to the austenite phase upon unloading. However, starting from the 2<sup>nd</sup> cycle, both the AP and SAT sample showed considerably higher strain recovery ratio. Throughout the cyclic test, the SAT sample demonstrated higher recoverable strains and recovery ratios in comparison to the AP sample. For instance, in the 1<sup>st</sup> cycle, the SAT sample showed the recovery ratio of 79.6% with recoverable strain of 6.86%, whereas the AP sample showed 73.1% recovery ratio with 5.87% recoverable strain.

Starting from the 2<sup>nd</sup> cycle, the SAT sample demonstrated more than 90% recovery ratio with 6.5% recoverable strain. At the 10<sup>th</sup> cycle, the SAT sample showed 96.6% recovery ratio with a recoverable strain of 6.62%, which is the highest superelasticity reported for the LPBF-processed NiTi to the best of our knowledge. It is also noticeable that the total imposed strain in the SAT sample was higher (8.61%) than the AP sample (8.03%) with the same applied stress which can be related to the change in grain size and orientation (Discussed in section 3.3.3) due to the heat treatment that increased the strain response in the superelastic limit. Despite having a higher imposed strain, the SAT sample demonstrated better superelastic performance in comparison to the AP sample.

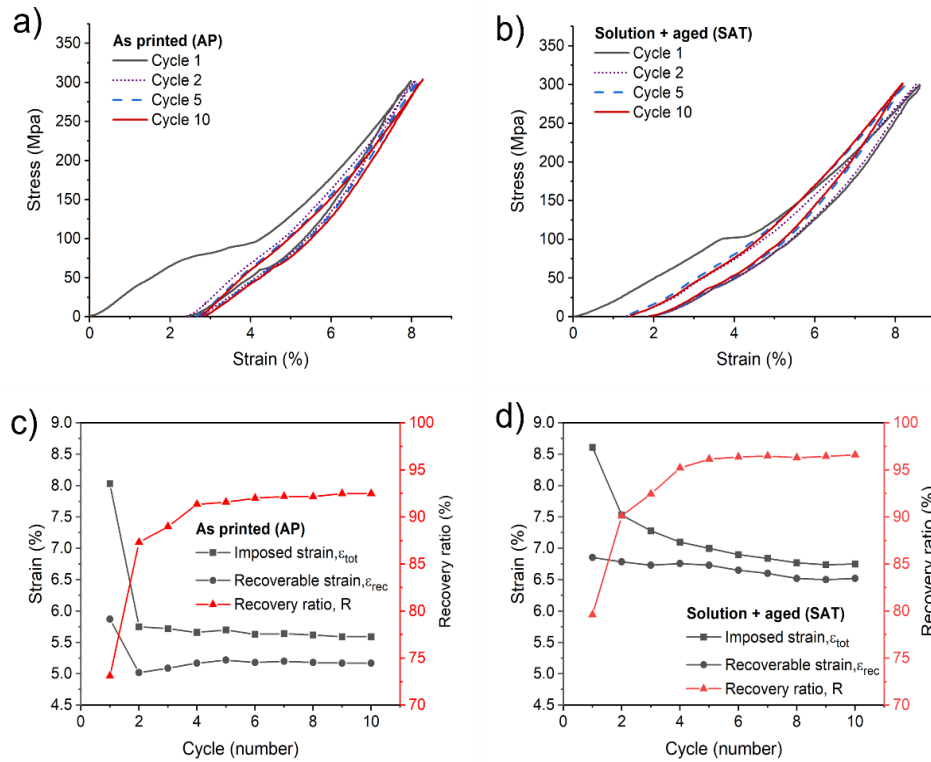


Figure 3.11. a) Cyclic compression test at body temperature (37 °C). of a) AP, b) SAT sample. Only cycles 1, 2, 5 and 10 have been plotted for the easy distinction. Imposed and recoverable strain with recovery ratio of c) AP and d) SAT sample.

Table 3.2. List of total strain, recoverable strain, and recovery ratio at different cycles of the AP and SAT sample.

Type	Applied stress (MPa)	1st Cycle			10th Cycle		
		$\epsilon_{tot}$ (%)	$\epsilon_{rev}$ (%)	Recovery ratio (%)	$\epsilon_{tot}$ (%)	$\epsilon_{rev}$ (%)	Recovery ratio (%)
As printed (AP)	300	8.03	5.87	73.1	5.59	5.17	92.48
Solution + Aged (SAT)	300	8.61	6.86	79.6	6.67	6.52	96.6

### 3.3.5. Micro-hardness measurements

The Vickers hardness measurements were performed to investigate the impact of heat treatment on the hardness property. The hardness tests were performed with the samples before and after the cyclic compression test (discussed in section 3.3.4) to investigate the hardness change by the cyclic loading due to the strain hardening. Figure 3.12 and Table 3.3 show the microhardness result of the AP, ST, and SAT samples. The AP sample showed a Vickers hardness of 283 HV. After both

the solution and aging heat treatment cycles, the hardness of the ST and SAT samples slightly increased. The SAT sample demonstrated a hardness of 359 HV, which is 27% higher than the AP sample. In comparison to the as-processed condition, the ST and SAT samples demonstrated higher hardness after the cyclic compression test. For instance, the hardness of the AP sample after cyclic compression test increased to 344 HV, which is an increase of 22% in comparison to the as-processed condition. Among the three samples, the hardness increases in the SAT sample due to the cyclic loading was the least, around 6%, compared to 22% and 18% for the AP and ST sample, respectively (Table 3.3). This indicates that the hardness property of the SAT sample is less affected by the cyclic loading which is desired during service.

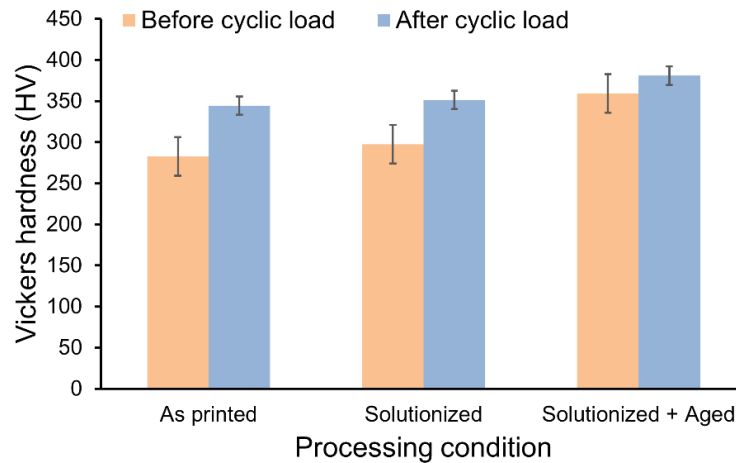


Figure 3.12. Vickers hardness test result of AP, ST, and SAT samples. Note the change of hardness with the solution and aging heat treatment cycle as well as after the cyclic compression load.

Table 3.3. Hardness of the AP, ST and SAT samples.

Sample type	Before cyclic load		After cyclic load	
	Hardness (HV)	Increase from AP sample	Hardness (HV)	Increase due to the loading
AP	283	-	344	22%
ST	297	5%	351	18%
SAT	359	27%	381	6%

## 3.4. Discussion

### 3.4.1. As-printed NiTi

In comparison to the as-received powder, the shallower and wider DSC phase transformation peak of the AP sample (Figure 3.3) can be attributed to the microstructural inhomogeneity induced by the complex thermal history during printing. The inhomogeneity of the AP microstructure is evident from the BSE image in Figure 3.5(a) and 3.5(b) (discussed in section 3.3.3). Due to the compositional inhomogeneity in the microstructure, the phase transformation in the AP sample occurred over a wider range of temperature. The change in  $A_f$  temperature in the AP sample compared to the as-received powder (from 32.6 °C to 2.1 °C) indicates the rise in Ni/ Ti ratio in the matrix phase of the AP sample [20]. This primarily happened due to the Ti loss by oxidation during printing. The presence of Ti rich oxide region in the AP sample was confirmed by the EDS analysis (Figure 5(b)). The Ti content makes NiTi very reactive with oxygen to form Ti rich oxides in the AP sample as widely reported [19], [83]. The loss of Ti by oxidation reduced the amount of Ti present in the NiTi matrix phase and consequently reduced the  $A_f$  temperature. In general, loss of Ti by oxidation is compensated by the loss of Ni by evaporation. However, in our samples, the loss of Ni by evaporation was negligible under the low LED condition and, therefore, the minute loss of Ti due to oxidation became a significant factor to reduce the  $A_f$  temperature of the printed sample. With the XRD analysis, the major phase constituent was found to be austenite in the AP sample (Figure 3.4). However, though certain Ti rich phases with oxide content were detected by microscopic and compositional analysis, no Ti rich phase was observed in the XRD analysis because of their insignificant content.

### 3.4.2. Development of heat treatment to tailor the phase transformation temperature

The heat treatment protocol including the solution and aging treatment was chosen to tailor the  $A_f$  temperature close to the body temperature as well as homogenize the microstructure and composition of the as-printed NiTi sample. It was found that after the solution treatment at 900 °C for 1 hour and the aging treatment at 450 °C for 30 minutes, the  $A_f$  temperature has shifted from 2.1 °C to 30.5 °C (Figure 3.3), which is desired for many biomedical applications [12], [84].

The solution treatment performed on the AP sample assisted in homogenizing the microstructure and composition. Consequently, the microstructure of the ST sample (Figure 3.6(a)) looked more regular and homogeneous in comparison to the AP sample (Figure 3.5). This is also evident from the narrower and sharper DSC phase transformation peaks of the ST sample in comparison to that of the AP sample (Figure 3.3). Because the solution cycle holds the microstructure at a high temperature, the large and irregular shaped Ti-rich region with oxygen content observed in the AP sample is formed into regular shaped Ti-rich oxides,  $Ti_4Ni_2O_x$ , randomly distributed throughout the microstructure (Figures 3.6(a) and 3.6(b)). However, some Ti may have dissolved into the NiTi matrix during the solution treatment, which slightly increased the  $A_f$  temperature of the ST sample (from 2.1 °C to 6.2 °C). The grains have coarsened and reoriented during the solution cycles, which affected the mechanical property of the ST sample (will be discussed in section 3.4.3).

During the aging treatment at 450 °C for 30 minutes, ultrafine Ni rich precipitates  $Ni_4Ti_3$  formed throughout the microstructure (Figures 3.4 and 3.7). However, no further change in the grain size or grain orientation was observed after the aging treatment. The grain coarsening and orientation observed in the EBSD of the SAT sample in Figure 3.8(b) occurred during the solution cycle. Formation of Ni rich precipitate during aging treatment depleted the Ni content in the matrix phase, which consequently increased the  $A_f$  temperature of the SAT sample to 30.5 °C (Figure 3.3).

It is notable that formation of ultrafine  $\text{Ni}_4\text{Ti}_3$  in the microstructure significantly affects the phase transformation and superelastic property of NiTi [24], [80], [85]. Presence of  $\text{Ni}_4\text{Ti}_3$  creates coherent stress field around the precipitate which facilitates reducing the nucleation energy required for the martensitic phase transformation [23], [85], [86]. Instead of directly transforming to the B19' martensite phase, the B2 austenite initially transforms to an intermediate phase, called R-phase (lattice parameter in between the B2 and B19' phase). This is because in presence of  $\text{Ni}_4\text{Ti}_3$ , the shear strain required for the R-phase formation is less than the shear strain required for the B19' martensite formation (1% vs. 10% shear strain required respectively) [73], [87]. First, R-phase nucleates at the interface between the B2 matrix and the  $\text{Ni}_4\text{Ti}_3$  precipitate, and with additional heating, finally R-phase transforms to the martensite. The DSC plot of SAT sample in Figure 3.3 shows the two-step phase transformation during cooling where the first peak indicates the transformation of B2 austenite to the R-phase and the second peak indicates the transformation of R-phase to the B19' martensite. Because of the less shear strain required for nucleating the new phase, the phase transformation in NiTi becomes easier and the likelihood of attaining a complete phase transformation increases. This is also demonstrated by the narrower and sharper phase transformation peaks of the SAT sample in Figure 3.3. The presence of  $\text{Ni}_4\text{Ti}_3$  and the R-phase in the SAT sample were also confirmed by the TEM analysis (Figure 3.7) which further supports the phenomena.

The heat treatment protocol developed in this study has a very short period of holding time compared to the other works reported in the literature. Lee et al. [62] reported that they did not observe any distinct phase transformation peak in the DSC test until they performed solution treatment at 1050°C for 10 hours. Haberland et al. [34] performed solution treatment at 950°C for 5.5 hours to homogenize the LPBF printed NiTi followed by 1.5 hours of aging to observe two

steps distinct phase transformation. In comparison to these cycles, the solution cycle used in this study was performed only for 1 hour followed by 30 minutes of aging to achieve the desired phase transformation behavior. Since in our work the Ni loss by evaporation during printing was negligible, the NiTi matrix of the AP sample was comparatively Ni rich that increased the rate of Ni-rich precipitate formation during aging. Again, the formation of precipitates by aging treatment is a function of atomic diffusion and the solubility of the precipitates in the matrix phase [88], [89]. At a higher aging temperature, the probability of forming new precipitation phase increases as the atoms become more diffusive. In contrast, the solubility of the precipitates in the matrix phase increases as the temperature increases, which reduces the probability of forming the precipitates. In Ni-rich NiTi, Ni-rich precipitates form when aging at the temperature between 300°C to 600°C. The aging temperature of 450°C compromised the effect of both diffusion and solubility on the precipitate formation, and the expected phase transformation behavior could be achieved in short holding time.

### **3.4.3. Effect of heat treatment on the compressive and superelastic properties**

The ultra-high compressive stress (3343 MPa) and strain (57%) obtained in the AP sample (Figure 3.10) matches the result reported by Gan et al. [90] in the LPBF printed NiTi. After performing the solution treatment, the stress required to deform the ST sample slightly decreased with the increase in ductility (67% strain) compared to the AP sample. This was because of the microstructural homogeneity, grain re-orientation, and grain coarsening occurred during the solution treatment. After the solution and aging treatment (the SAT sample), the overall elongation before fracture was considerably reduced in comparison to the other two samples. This can be attributed to the presence of ultrafine Ni<sub>4</sub>Ti<sub>3</sub> precipitate particles in the microstructure formed

during the aging treatment that acted as a barrier to the dislocation motion and reduced the overall ductility of the SAT sample.

From the stress-strain curves in Figures 3.10 and 3.11, the critical stress for the stress induced martensitic transformation (SIM) was found to be slightly higher for the SAT sample than the AP sample (100 MPa vs. 72 MPa). It is well known that the critical stress for martensitic transformation is low along [001] direction [48], [91]. It was shown in the EBSD analysis (section 3.3) that, after solution and aging treatment, the grains became more randomly oriented in compared to that in the AP sample where the grains were mostly oriented in the [001] direction. The grains deviated from the [001] direction consequently increased the critical stress for the SIM transformation in the SAT sample. However, low critical stress for the martensitic phase transformation is expected to improve the strain recovery since this reduces the chance of any plastic deformation before the phase transformation takes place [65], [78], [92]. It is also noted that, due to the reduced stiffness, the applied strain on the SAT sample was higher than that on the AP sample (Figure 3.11 and Table 3.2). Nevertheless, the SAT sample demonstrated a higher recoverable strain compared to the AP sample (Figures 3.11(c) and (d)). The stress-strain hysteresis of NiTi in the cyclic test is an important indication of functional fatigue performance. The narrower hysteresis in the SAT sample (Figures 3.11(a) and (b)) means that these samples have better fatigue performance [84], [93], which may be important for some biomedical applications.

The improved superelasticity observed in the SAT sample can be attributed to the microstructural homogeneity obtained by the heat treatment as well as the presence of  $\text{Ni}_4\text{Ti}_3$  precipitates that triggered the phase transformation, decreased the plastic deformation, and increased the

recoverable strain upon unloading. Therefore, the stress plateau in the SAT sample was comparatively flatter and shorter, presenting smoother phase transformation in the SAT samples.

#### **3.4.4. Change in hardness**

After solution treatment, because of the compositional homogeneity and reduced residual stress (that can locally induce to form martensite), the volume fraction of austenite may have slightly increased in the microstructure. Since the austenite in NiTi is harder than the martensite, the overall hardness of the ST sample increased (Figure 3.12 and Table 3.3). After solution and aging treatment, the hardness of the SAT sample increased due to the presence of ultrafine  $\text{Ni}_4\text{Ti}_3$  precipitates in the microstructure that restricted dislocation motion [94], [95]. Due to the cyclic loading, the hardness of each sample has increased which can be attributed to the strain hardening behavior. Upon loading, newly formed dislocations in the microstructure interact with each other, which hardens the materials [96], [97]. This is also an indication of the plastic deformation taken place during cyclic compression test and explains the reason for having certain residual strain after loading (Figure 3.11) since dislocations act as a barrier to have reversible austenitic phase transformation, and thus recovering the imposed strain. To note that the change in hardness in the SAT sample after cyclic loading was smallest (6% compared to 22% of AP sample) among the three samples (Figure 3.12, Table 3.3). The presence of  $\text{Ni}_4\text{Ti}_3$  in the SAT microstructure facilitated the martensitic phase transformation and reduced the dislocation generation by plastic deformation upon loading. As a result, the SAT sample demonstrated less strain hardening due to the cyclic loading and the hardness of these samples were less affected. This can be related to the reduction in the residual strain of the SAT sample in comparison to the AP sample (Figure 3.11 and Table 3.2) which means reduced plastic deformation in the SAT sample during cyclic loading.

### 3.5. Conclusion

The work was conducted to develop a proper post heat treatment protocol to overcome the major limitation of the AM processed NiTi parts by achieving the desired phase transformation temperature with improved superelastic characteristics for the biomedical applications. The summary of the work is listed as follows.

- Because of the compositional change and complex thermal cycles associated with LPBF printing, it is difficult to attain the desirable phase transformation and superelastic property in the as-printed NiTi. In this work, NiTi was printed in LPBF without any pre-substrate heating on Ti baseplate using a low laser energy density of  $35 \text{ J/mm}^3$  to minimize the compositional change while avoiding any structural defects such as crack or delamination in the printed sample. Because of the Ti loss by oxidation, the austenite finish ( $A_f$ ) temperature of the as printed sample was found as  $2.1 \text{ }^\circ\text{C}$ .
- Subsequently, a post heat treatment protocol was developed to tailor the  $A_f$  temperature of the printed sample slightly below the body temperature to meet the biomedical requirements. The heat treatment protocol developed here includes the solutionizing cycle at  $900 \text{ }^\circ\text{C}$  for 1 hour followed by the aging cycle at  $450 \text{ }^\circ\text{C}$  for 30 minutes. The solution treatment homogenized the microstructure, whereas the aging cycles formed ultrafine and uniformly distributed Ni-rich  $\text{Ni}_4\text{Ti}_3$  precipitates in the microstructure that shifted the  $A_f$  temperature from  $2.1 \text{ }^\circ\text{C}$  to  $30.5 \text{ }^\circ\text{C}$ .
- In the cyclic compressive test at the body temperature, starting from the 2<sup>nd</sup> cycle, the SAT sample demonstrated superelastic characteristics with a recovery ratio of more than 90% with 6.78% recoverable strain. The recovery ratio and the recoverable strain at 10<sup>th</sup> cycle was found as 96.6% and 6.52% respectively. However, the recovery ratio at the 1<sup>st</sup> cycle

was comparatively low (79.1% with the recoverable strain of 6.86%). This provides an advantage to deform the SAT sample to a certain dimension in the manufacturing stage and obtain nearly full superplastic characteristics during service.

- The SAT samples also showed narrower stress-strain hysteresis which indicates a better fatigue performance of these samples. In comparison to the AP sample, the SAT sample showed isotropic microstructure due to the grain coarsening and re-orientation during the solution heat treatment cycle.
- In the microhardness test, the SAT sample showed increased hardness by 11% because of the precipitation hardening. The hardness of these samples are also less affected by the cyclic loading which is desired during the service. This was attributed to the improved reversible phase transformation and reduced plastic deformation in presence of  $\text{Ni}_4\text{Ti}_3$ .

This work expects to provide an important processing roadmap in making functional NiTi biomedical implants fabricated by LPBF with desirable phase transformation and superelastic behaviors. However, further research work is required on the durability and biocompatibility of the processed sample for the biomedical devices.

## Chapter 4: Optimizing the Printing Parameters and Post Processing

### Conditions to Fabricate Superelastic Stent

#### 4.1. Introduction

NiTi stent is attractive since they provide the advantage of easy deployment due to the self-expandable property as well as behave superelastically when deployed inside the body. In contrast to the multi-step traditional manufacturing process, making NiTi stent by additive manufacturing (AM) is demanding since it offers one-step fabrication process as well as customizable patient design. However, the individual strut of a stent is very thin (less than 200  $\mu\text{m}$ ) and making such thin structure by AM is challenging. Since the phase transformation and superelastic property of NiTi is very sensitive to the microstructure and composition, due to the different thermal history in thin struts the final property obtained may be different in compared to the large cross-sectional sample. In addition, the presence of pores and surface defects in such thin structure may lead to premature structural failure. In this chapter, laser powder bed fusion (LPBF) processing parameters have been studied and optimized to print NiTi thin struts with minimum porosity and avoid structural failure during deformation. The post surface treatment has been studied to remove the un-melted powder and minimize surface defects. The post heat treatment of the thin printed NiTi struts has been developed to obtain the austenite finish ( $A_f$ ) temperature closely below the body temperature as well as to improve the superelastic and shape memory property of the printed thin struts for the stent application. The change in the strut thickness during the processing steps has been evaluated to know the proper strut thickness required during the design to ultimately get a stent with desired strut thickness. The mechanical and superelasticity test at body temperature as well as the different materials characterization have been performed to evaluate the final properties of the fabricated thin NiTi samples.

## 4.2. Materials and method

### 4.2.1. Materials and fabrication

Pre-alloyed NiTi powder with 55.5 wt.% (50.7 at.%) Ni content was acquired from AP & C, a GE Additive Company (St-Eustache, Québec, Canada). In this section of study, since very thin structure was printed (high surface to volume ratio and more susceptible to oxidation), larger sized powder was used since they contain comparatively lower oxygen. The powder was mostly spherical with the diameter range between 45  $\mu\text{m}$  and 106  $\mu\text{m}$ . The powders contained 0.011 wt.% of oxygen. The printing was performed on a NiTi substrate and without any prior heating under 250 ppm oxygen level. To study the effect of laser energy density (LED) on the phase transformation, density and superelastic properties of the printing thin structure the sample were printed using a wide range of LED as shown in Table 4.1. The surface treatment of the printed sample was performed in an acid solution of HF: HNO<sub>3</sub>: H<sub>2</sub>O with the mixture ratio of 1: 2: 3. The acid solution beaker was placed in a water bath to avoid excessive heating during the etching process. The post heat treatment was performed in the same manner mentioned in Chapter 3.

Table 4.1. LPBF processing parameter used to print the thin NiTi sample.

Speed (mm/s)	Layer thickness ( $\mu\text{m}$ )	Hatch ( $\mu\text{m}$ )	Power (W)	Energy density (J/mm <sup>3</sup> )
900				57
550				93
400	90	50	230	128
300				170
260				198

### 4.2.2. Experimental

The DSC test, optical microscopy, SEM and EDS analysis of the samples were performed using the same instrument mentioned in Chapter 2. The cyclic 3-point bending test of the fabricated thin rods were performed in a dynamic mechanical analysis (DMA, series QA800) manufactured by TA instrument (New Castle, Delaware, USA) at 37 °C to study the mechanical and superleastic

properties at body temperature. The test was performed at a displacement control mode with a strain rate of 0.5% per minute. The sample was loaded to deform up to 4.5% strain followed by unloading to zero stress. The load displacement data obtained from the test were converted to the stress strain data using the following formula.

$$\text{Bending stress} = \frac{FL}{\pi r^3}$$

$$\text{Bending strain} = \frac{6Dd}{L^2}$$

Where F is applied load, L is span length, r is sample radius, d is sample diameter, D is sample deflection.

### **4.3. Result and discussion**

#### **4.3.1. Variation of phase transformation temperature due to the sample diameter**

The  $A_f$  temperature of NiTi is highly sensitive of the microstructure and the composition. Given the same printing condition, the thermal cycles associated in LPBF printing can differ with different sample diameters. Therefore, it is important to study whether change in the sample diameter has any effect on the  $A_f$  temperature of the printed NiTi. In this regard, cylindrical NiTi samples of 4 mm, 1 mm, 0.5 mm and 0.25 mm diameter were fabricated using the same printing condition of LED 93 J/mm<sup>3</sup>.

The illustration of the sample size as well as the DSC phase transformation result are shown in Figure 4.1. And the corresponding  $A_f$  temperatures are listed in Table 4.2. Except for the 4 mm, all the sample showed two-steps phase transformation during heating (martensite to R-phase to austenite). The 4 mm sample showed one step phase transformation (martensite to austenite). It is to note that the NiTi powder used to fabricate the sample was  $A_f$  temperature of 32.6 °C. From Table 4.2, it is seen that the  $A_f$  temperature of the samples decreased with the increase in the sample diameter. The drop of  $A_f$  indicate the rise in the Ni/Ti ratio in the NiTi matrix. This primarily can happen due to the loss of Ti by oxidation during printing. With the increase in sample diameter,

the cooling rate of the melt pool becomes slower. Consequently, the deposited layer stays at high temperature for longer time and increases the loss of Ti by oxidation. The cross-sectional area of a 4 mm diameter sample is more than 250 times larger compared to a 0.25 mm sample. This significantly increased the Ti loss by oxidation in 4 mm sample and considerably dropped the  $A_f$

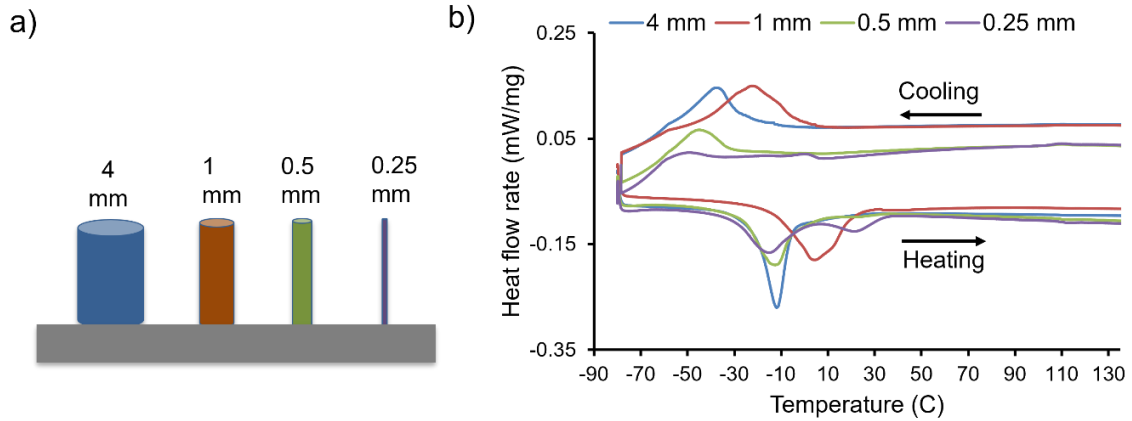


Figure 4.1. a) Illustration and b) DSC plot of the NiTi sample with various diameters printed under same condition.

temperature. The difference in  $A_f$  between 0.25 mm and 0.5 mm sample was insignificant because of the closer cross-sectional area. The study concludes that to achieve the same phase transformation behavior in NiTi part, it is required to adjust the printing condition with significant change in the dimension.

Table 4.2. Diameter, cross sectional area and corresponding  $A_f$  temperature of the NiTi printed under same condition.

Sample diameter (mm)	0.25	0.5	1	4
Cross-sectional area (mm <sup>2</sup> )	0.2	0.8	3.1	50.3
$A_f$ (°C)	32	31.5	24	-3

### 4.3.2. Variation of $A_f$ temperature along the building direction

The convenient way to print stent in LPBF is layer by layer along the long direction (parallel to the building direction). Since cooling rate throughout the height of a sample may not be the same, it is important to check whether the  $A_f$  temperature of the sample throughout the height is not affected.

To study the variation of  $A_f$  temperature along the height of the NiTi rod, samples were taken for the DSC test from four different height of the printed 500  $\mu\text{m}$  (0.5 mm) rod. The illustration of the sample as well as the DSC result are shown in Figure 4.2. It is observed from Figure 4.2(b) that there was no significant difference in the  $A_f$  temperature at the different height of the NiTi rod. The  $A_f$  temperature is dependent on the Ni/Ti content in the matrix phase. The same  $A_f$  temperature throughout the sample height indicate that the cooling rate at different height of the sample was not significant enough to change the local composition of the sample, i.e., to affect the Ni evaporation or oxidation of Ti and therefore the  $A_f$  temperature of the rod was not affected.

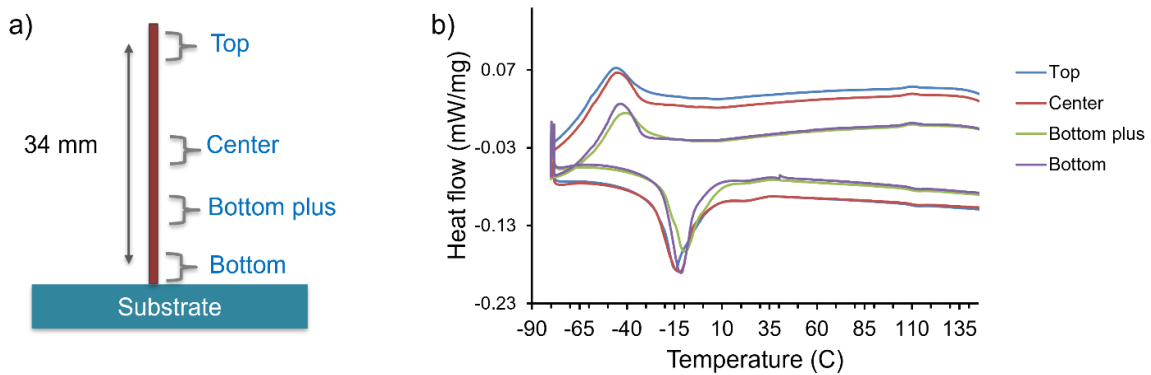


Figure 4.2. a) Illustration and b) DSC plot of the NiTi sample taken from different height of the 500  $\mu\text{m}$  rod.

### 4.3.3. Effect of laser energy density on the phase transformation behavior

Since change in the matrix composition by loss of Ni or Ti can happen during printing which ultimately affect the  $A_f$  temperature of the printed sample, the phase transformation properties of

the thin NiTi sample printed with various laser energy density (Table 4.1) were studied. The DSC plot of the NiTi samples printed with various LED are shown in Figure 4.3. The Figure shows that the martensite to austenite phase transformation peaks during heating slightly shifted to the upward with increasing LED. For instance, the sample printed with 57 J/mm<sup>3</sup> LED was of -2 °C, whereas the sample printed with 170 J/mm<sup>3</sup> showed A<sub>f</sub> of 18 °C. With increasing LED, more Ni evaporated from the melt pool and reduced the Ni/Ti ratio in the matrix phase and increased the A<sub>f</sub> temperature

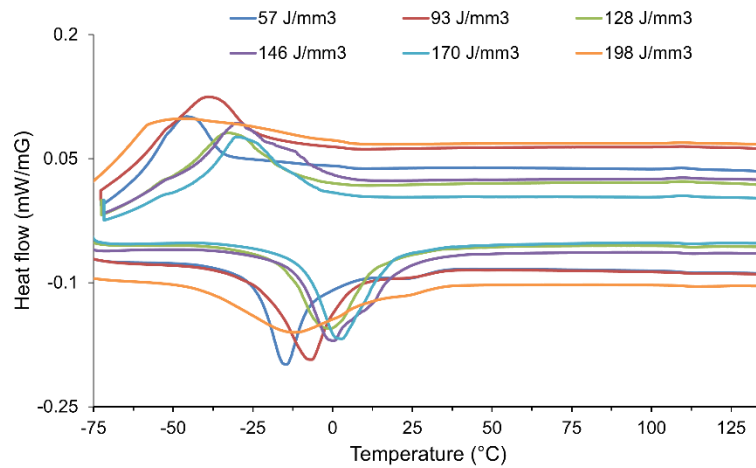


Figure 4.3. DSC phase transformation plot of the 500 μm NiTi rod printed with various LED.

accordingly. However, with further increase in LED the A<sub>f</sub> temperature dropped to 13 °C which can be attributed to the high Ti loss by oxidation at very high LED that compensated the Ni loss by evaporation and slightly dropped the A<sub>f</sub> temperature. Wang et al. [35] and Haberland et al. [98] also reported same observations in the change of A<sub>f</sub> temperature with increasing LED for the LPBF fabricated NiTi samples.

#### 4.3.4. Effect of laser energy density on the porosity content

The presence of pores in the printed part acts as a crack initiation site and reduces the ultimate fracture strength and ductility of the part. Specially, for the thin strut as in a stent (less than 200 μm diameter), presence of a small sized pore can significantly reduce the load bearing cross-

sectional area resulting in high local stress leading to the premature failure and poor fatigue performance. In that regard, thin NiTi rods of 500  $\mu\text{m}$  were fabricated using various LED starting from 57  $\text{J}/\text{mm}^3$  to 198  $\text{J}/\text{mm}^3$  as listed in Table 4.1. The density of the printed rods was determined

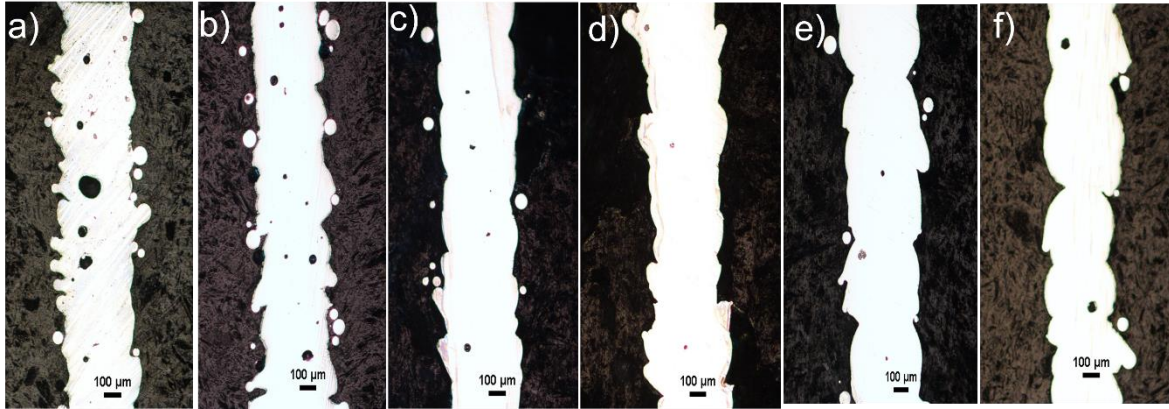


Figure 4.4. Optical microscopy (parallel to building direction) of the 500  $\mu\text{m}$  NiTi rods printed with various laser energy density of a) 57  $\text{J}/\text{mm}^3$  b) 93  $\text{J}/\text{mm}^3$  c) 128  $\text{J}/\text{mm}^3$  and d) 146  $\text{J}/\text{mm}^3$  e) 170  $\text{J}/\text{mm}^3$  f) 198  $\text{J}/\text{mm}^3$ .

by the Archimedes method as well as by cross-sectional microscopic analysis using ImageJ. Figure 4.4 and Figure 4.5 show the optical microscopic images of the cross-section parallel to the building direction. The average density and the size of largest pores found in four cross-sectional observations for each sample are plotted in Figure 4.6.

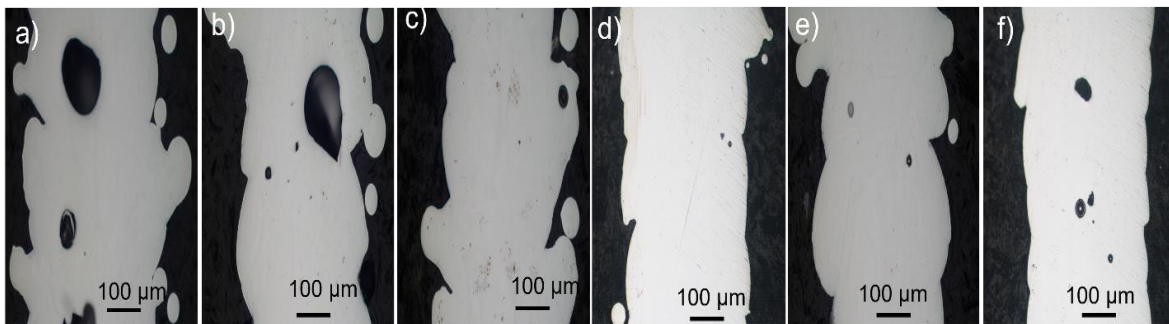


Figure 4.5. Optical microscopy (parallel to building direction) of the 500  $\mu\text{m}$  NiTi rods printed with various LED of a) 57  $\text{J}/\text{mm}^3$  b) 93  $\text{J}/\text{mm}^3$  c) 128  $\text{J}/\text{mm}^3$  d) 146  $\text{J}/\text{mm}^3$  e) 170  $\text{J}/\text{mm}^3$  f) 198  $\text{J}/\text{mm}^3$ .

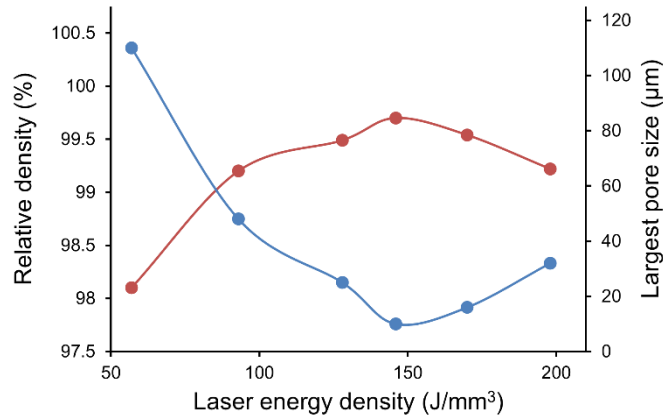


Figure 4.6. Relative density and the largest pore size (among the four cross-sectional observations per sample) with different LED.

The Figures show that at low LED printing, the size and quality of the pores are very high which may be attributed to the lack fusion at low LED. With increasing LED, the pores size and quantity decrease up to a certain point providing maximum density in the sample. With further increases in LED, the pore content again increases may be due to the high melt pool spattering and keyhole porosity. Though maximum density of the sample was found for the 146 J/mm<sup>3</sup>, density of the sample with 128 J/mm<sup>3</sup> and 170 J/mm<sup>3</sup> were also very closer to the maximum value.

#### 4.3.5. Surface defects and surface treatment

In laser powder bed fusion technology, the printed part always comes with some partially melted powder stuck to the surface as well as uneven surface because of the layer-by-layer stacking. These partially melted powder and the uneven surface act as stress concentration sites during loading resulting in accelerated crack generation. Specifically, presence of such surface defects can significantly influence the fatigue performance of the part and leads to premature failure. The SEM images of the stent printed with different LED are shown in Figure 4.7. From the Figure, it is observed that with increasing LED, the amount of partially melted powder on the surface decreases. This is because of the high temperature melt pool at high LED that completely melts the powder in the surrounding area. In contrast, at the low LED, since the melt pool temperature is comparatively low, there are higher number of powders in the surrounding area that are not fully

melted rather than partially melted due to the heat affected area. The stacking of the layers on top of each other are also clearly observed. It is also observed from Figure 4.7 that the thickness of the rods increases with increasing LED due to the larger heat affected area at higher LED. The increase in the average thickness of the individual struts in the fabricated stent printed with different LED in compared to the nominal (design) thickness are plotted in Figure 4.8. It is seen that up to LED of  $170 \text{ J/mm}^3$  the increase in thickness was linear and for  $198 \text{ J/mm}^3$  the increase was much higher.

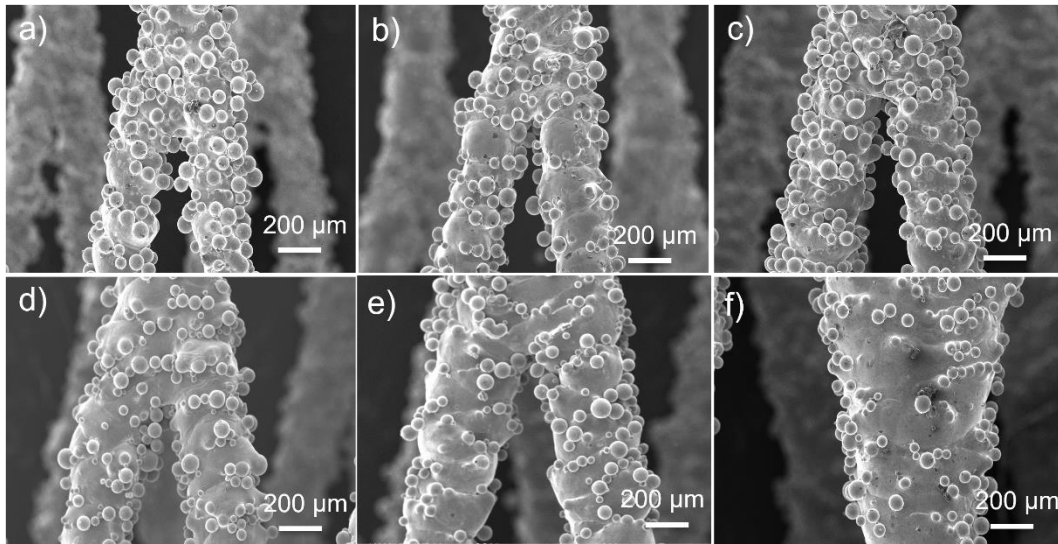


Figure 4.7. SEM image of the stent with  $250 \mu\text{m}$  nominal strut thickness printed with various laser energy density of a)  $57 \text{ J/mm}^3$  b)  $93 \text{ J/mm}^3$  c)  $128 \text{ J/mm}^3$  d)  $146 \text{ J/mm}^3$  e)  $170 \text{ J/mm}^3$  f)  $198 \text{ J/mm}^3$ .

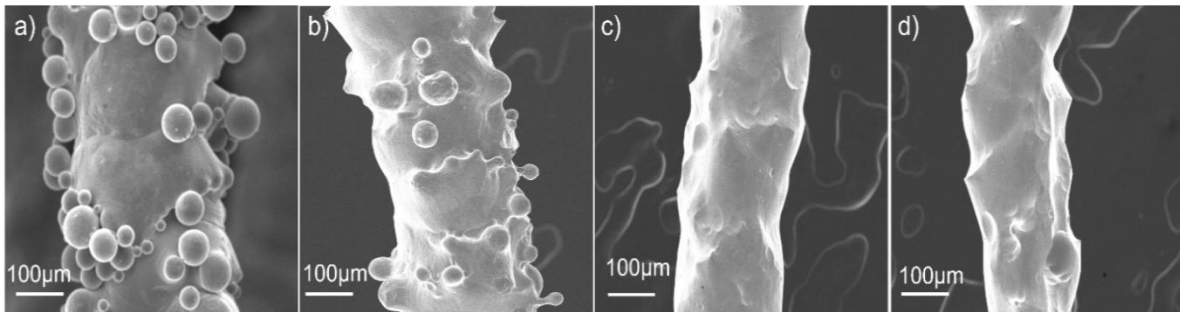


Figure 4.8. a) as printed strut of a NiTi stent, etched in the acid solution for b) 1 minute, c) 3 minutes and d) 5 minutes.

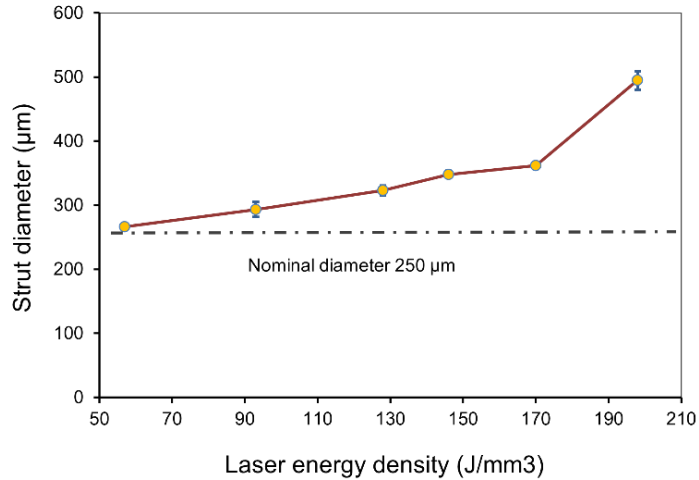


Figure 4.9. Change in strut thickness with increasing LED.

Chemical treatment is a widely used technique to remove the surface defects from the NiTi parts. Several researchers have reported that use of acid solution of HF: HNO<sub>3</sub>: H<sub>2</sub>O with the mixture ratio of 1: 2: 3 effectively removed the un-melted powders as well as made the surface smoother [99], [100], [101]. To figure out the etching time that provides the best surface for the printed stent, the chemical treatment was performed for different holding time in the acid solution. Figure 4.9 shows the SEM images of the NiTi single strut etched for different holdings time. It was found that etching for 3 minutes provided the better surface finish with removing the attached powder from the surface. Etching for a shorter time could not remove the attached powder completely and left the surface rough. Whereas, etching for longer time provided with highly corroded local area with sharp corners.

#### 4.3.6. Structural failure and superelasticity of the printed rod

To investigate the mechanical properties as well as the superelastic behavior, cyclic 3-point bending tests were performed at body temperature (37 °C) on the 500 µm rods printed with various LED. The stress-strain plot and the superelastic properties of the test are shown in Figure 4.10 and Table 4.3 respectively. The test result shows that the rod printed with LED of 57 J/mm<sup>3</sup> and 93 J/mm<sup>3</sup> failed at 2.75% and 2.79% of strain, respectively and these sample could not be deformed

up to 4.5% of strain. The rod printed with higher LED such as 128 J/mm<sup>3</sup>, 146 J/mm<sup>3</sup>, 170 J/mm<sup>3</sup> and 198 J/mm<sup>3</sup> could be deformed up to 4.5% strain without any fracture and unloaded to zero stress. It is observed from Figure 4.10(b) that the loading and unloading stress curves for these samples were not identical. It is observed that the loading and unloading stress of the sample

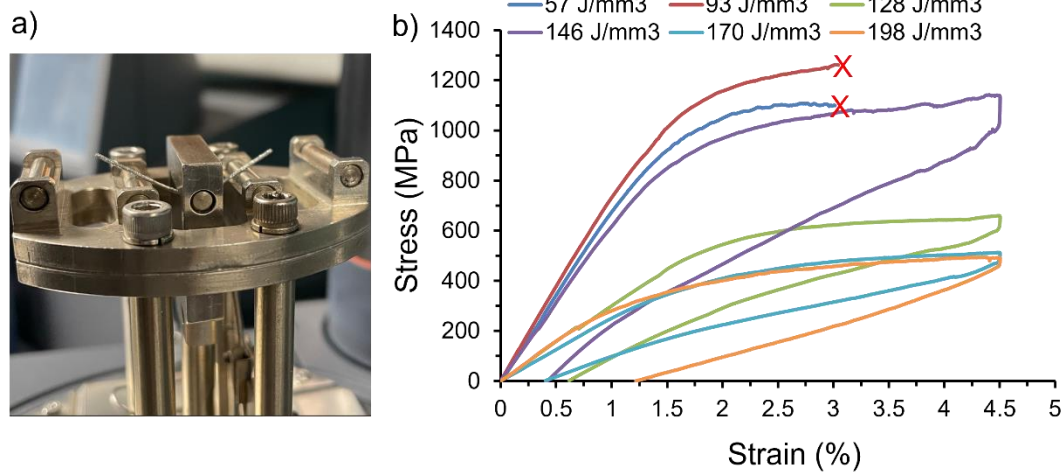


Figure 4.10. a) 3-point bending setup in DMA, b) calculated stress-strain plot of displacement-controlled load-unload 3-point bend test at 37 °C of 500 μm rod printed with different LED.

Table 4.3. Load-unload 3-point bending test result at 37 °C of 500 μm NiTi rod printed with different laser energy density.

Laser energy density (J/mm <sup>3</sup> )	57	93	128	146	170	198
Max. applied strain, $\epsilon_{tot}$ (%)	4.5	4.5	4.5	4.5	4.5	4.5
Max. fracture strain (%)	2.75	2.79	-	-	-	-
Reversible strain, $\epsilon_{rev}$ (%)	-	-	3.86	4.03	4.12	3.27
Recovery ratio, $\epsilon_{rev}/\epsilon_{tot}$ (%)	-	-	86%	90%	92%	73%

printed with 146 J/mm<sup>3</sup> was highest than the other three samples. Samples printed with 170 J/mm<sup>3</sup> and 198 J/mm<sup>3</sup> showed similar loading stress curve. Among all four samples undergone with the cyclic load, the sample printed with J/mm<sup>3</sup> showed the highest recoverable strain of 4.12% with 92% recovery ratio. The early structural failure of the sample printed with 57 J/mm<sup>3</sup> and J/mm<sup>3</sup> LED can be attributed to the high porosity content (discussed in section 4.3.4) that reduced the

load bearing capacity of these samples. The loading and unloading stress as well as the strain recovery of NiTi are dependent on the grain size, orientation and the presence of any secondary precipitates phase in the microstructure [35], [50], [102]. Moghaddam et al. [50] printed NiTi under different LED and showed that better superelasticity was obtained for the sample with [001] orientated grain along the building direction. The change in LED also affects the grain size and shape that ultimately affects the stress-strain curve. The NiTi materials property desired for the stent application is to have lower loading stress as well as lower hysteresis with higher recoverable strain [55], [84], [103]. Among the samples fabricated, the sample fabricated with  $170 \text{ J/mm}^3$  showed best match to these criteria.

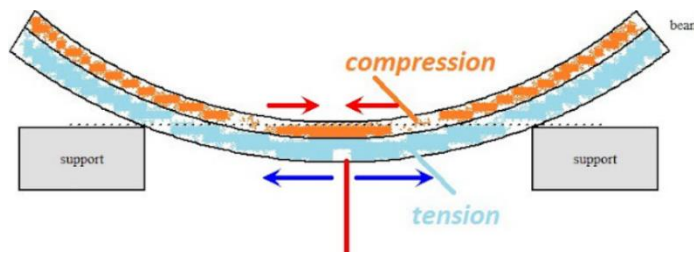


Figure 4.11. Stress distribution in a 3-point bending test [104].

The sample printed with  $146 \text{ J/mm}^3$  though demonstrated strain recovery closer to the sample printed with  $170 \text{ J/mm}^3$ , the higher loading stress and stress-strain hysteresis of the sample is not suitable for the stent application, in compared to the other samples.

It should be noted that in comparison to the pure compression or tensile stress bending stress is a localized stress where maximum stress is applied only in a localized cross-section of the beam [104]. Since in a 3-point bending test, the upper surface of the beam experience highest compression stress whereas the bottom portion of the surface experience highest tensile stress. Therefore, care should be taken while using the bending test result for the advanced simulation to analyze and qualify the materials performance.

#### 4.3.7. Shape setting (aging) heat treatment

The final stage of making NiTi devices is performing the aging treatment which acts as the shape setting treatment and train NiTi to remember certain shape. The treatment is also performed to improve the shape memory, superelasticity and mechanical properties of the final NiTi part [19], [62]. NiTi remembers the shape given during this heat treatment process and can retain the shape after deformation either by heating or unloading. The treatment is generally performed between 300 °C to 600 °C. In some cases, a prior solution treatment followed by quenching is recommended to homogenize the microstructure. Specifically, for additively manufactured bulk part, solution heat treatment is performed to reduce the built in residual stress and homogenize the microstructure prior to performing the aging (shape setting) treatment. However, for the very thin strut structure like in a stent (less than 200  $\mu\text{m}$ ) the solution treatment followed by quenching form a thick (in compared to the sample diameter) surface oxygen layer that facilitates easy crack generation and lead to the premature failure during loading. The high oxygen rich outer region in the solution treated 500  $\mu\text{m}$  rod was observed under SEM and shown in the Figure 4.12.

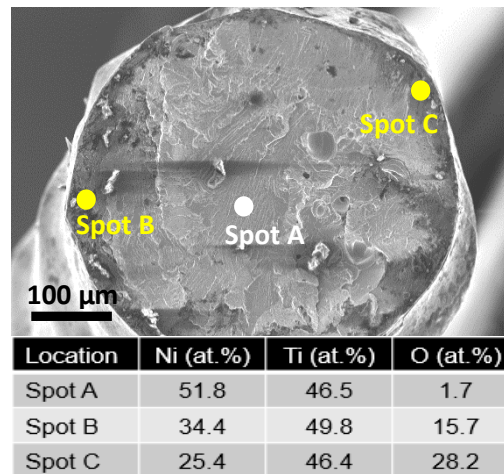


Figure 4.12. SEM image and EDS analysis of the solutionized (900 °C, 1 hour) 500  $\mu\text{m}$  NiTi rod fracture surface.

In comparison to the large bulk sized sample, the thin structure possesses less inhomogeneity and residual stress during printing due to the comparatively less thermal gradient. For these reasons, the shape setting treatment was performed on the as-printed thin structure without any prior solution treatment.

It was shown in chapter 3 that the aging treatment at 450 °C provides sharper and distinct phase transformation with shorter holding time. Therefore, the aging treatment for the thin rods were also performed at 450 °C for 30 minutes that provided with the  $A_f$  temperature of 33 °C. The DSC plots showing the phase transformation of the as printed (with LED 170 J/mm<sup>3</sup>) and heat treated NiTi are shown in Figure 4.13(a). The Figure shows that after aging treatment the  $A_f$  temperature increased to 33 °C. This happened due to the formation of Ni-rich precipitation phase that deplete Ni content in the matrix phase and increase the  $A_f$  temperature. The aged sample showed two step

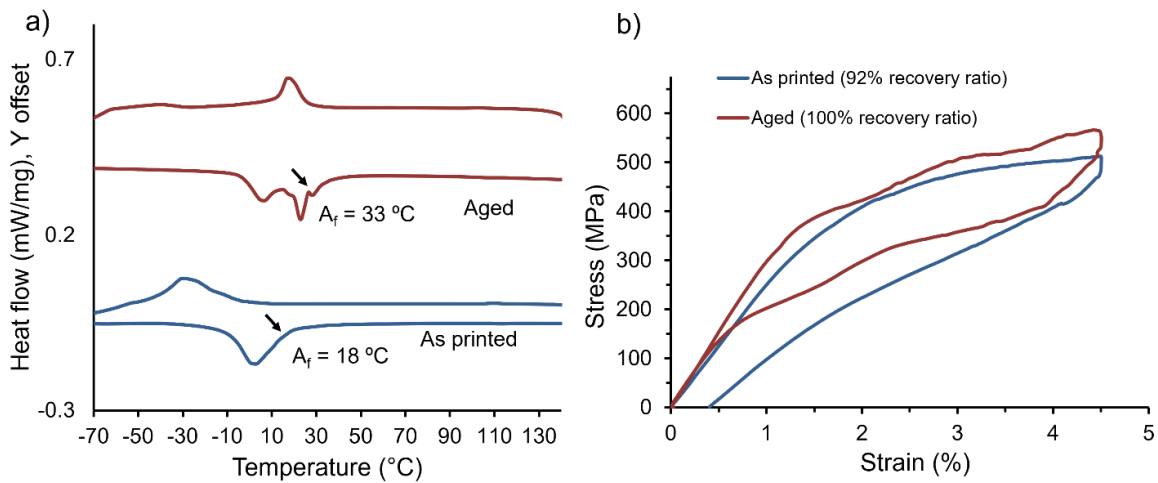


Figure 4.13. a) DSC phase transformation plot, b) Calculated stress-strain plot of displacement-controlled load-unload 3-point bend test at 37 °C of the as printed and aging heat treated (at 450 °C, 30 minutes) NiTi sample.

martensite to austenite phase transformation which normally happens in presence of Ni<sub>4</sub>Ti<sub>3</sub> in the microstructure as discussed elaborately in Chapter 3 (section 3.4.3).

The load-unload 3-point bend test at 37 °C was performed to evaluate the superelastic property of the sample after performing the aging heat treatment. Figure 4.13(b) shows the stress-strain plot of the cyclic 3-point bend test of the as-printed and aged samples. The Figure clearly shows the significant improvement of the superelastic property after performing the aging treatment. The aged NiTi rod demonstrated perfect superelasticity with 4.5% recoverable strain and 100% recovery ratio. To the best of our knowledge, this is the first time to report perfect superelasticity in the LPBF processed NiTi sample.

#### **4.3.8. Printing superelastic NiTi stent**

The major challenges in making stent by AM are maintaining structural integrity and avoiding structural failure during deformation which is dominated by the porosity content and the surface defects. According to the study on the effect of LED on the porosity content on the thin NiTi sample, LED 128 J/mm<sup>3</sup>, 146 J/mm<sup>3</sup> and 170 J/mm<sup>3</sup> provided density more than 99.5%. To remove the partially melted powder from the surface, the surface treatment study showed that 3 minutes etching in the acid solution (HF: HNO<sub>3</sub>: H<sub>2</sub>O = 1: 2: 3) provided with comparatively smoother surface.

The NiTi stent is fabricated in an open condition which is compressed and placed inside a catheter system to deploy in the destination body part. When the stent is released from the catheter, the stent retains its originally fabricated open shape. The loading and unloading stress during compression and opening is important. A lower loading stress plateau between 500 MPa to 600 MPa as well as lower stress-strain hysteresis with higher unloading stress are recommended for the stent application [9], [12], [84]. This is because of that a stent with lower loading stress requires a catheter made with a less strong material that allow to make the catheter sheath thinner and more flexible. Such a delivery system allows to better navigate the tortuous arteries and vessels during

deployment with less invasion. In addition, higher superelasticity is expected to make the stent recover most of its original open shape when released from the catheter. Having these considerations, among the printed thin samples, the sample printed with  $170 \text{ J/mm}^3$  showed the most suitable properties for the stent application including lower loading stress, lower hysteresis, and maximum recoverable strain. Finally, the aging treatment (shape setting treatment) on the printed and surface treated sample was performed at  $450 \text{ }^\circ\text{C}$  for 30 minutes to tailor the  $A_f$  temperature of the printed closely below the body temperature as well as to improve the superelasticity and shape memory property. The heat-treated sample demonstrated complete superelasticity with 100% strain recovery which is rarely achieved in NiTi. The nitinol rod processed with the optimized conditions showed visual shape recovery with increasing temperature as demonstrated in the video [105].

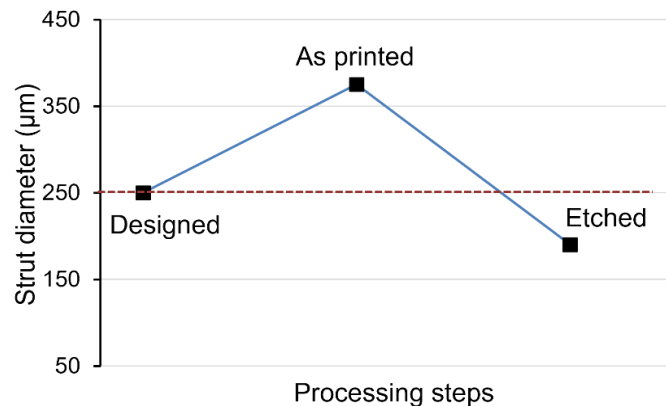


Figure 4.14. Strut thickness changes in the processing steps of a stent.

The final processed stent consists of individual strut thickness of  $190 \text{ }\mu\text{m}$ . Since the stent was printed with comparatively higher LED, the strut thickness of the printed stent increased by 50% during printing due to the larger heat affected zone which was further reduced during etching by 50% providing with  $190 \text{ }\mu\text{m}$  strut thickness. Change in the strut thickness with the processing steps is plotted in Figure 4.13. Using the developed printing and post processing conditions finally the NiTi stents of  $7 \text{ mm}$  outer diameter and  $13 \text{ mm}$  height were fabricated. These stents could be

deformed without any structural failure as well as demonstrated visual superelastic property when released [106]. The fabricated nitinol stent following the developed printing parameter as well the post processing conditions is shown in Figure 4.14.

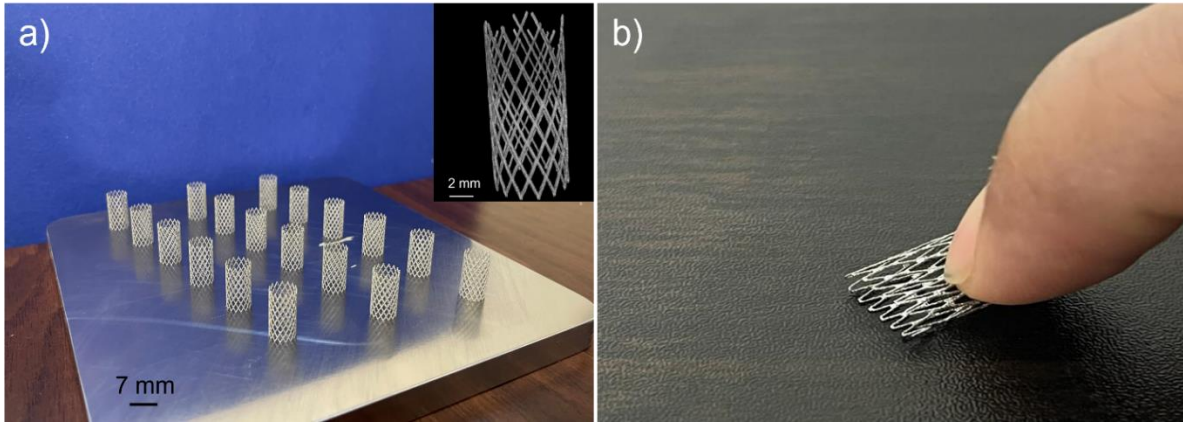


Figure 4.15. a) as LPBF printed NiTi stent on the built plate. Inset is the micro-CT scan image of a single stent. b) Shows that the stent was completely flattened without any structural damage.

#### 4.4. Conclusion

In this chapter, the LPBF printing parameter as well as the post processing technique has been studied and optimized to fabricate the NiTi stent with structural accuracy, mechanical integrity as well as proper phase transformation and superelastic property desirable for the biomedical application. The summary of the work is listed as follows.

- Using same printing parameter to fabricate NiTi part of different diameters can possess different phase transformation temperature because of the variation in the Ni evaporation or Ti loss by oxidation due to the different associated thermal cycle in different cross-sectional area. However, the  $A_f$  temperature of a single sample throughout the height did not show considerable variation in the phase transformation temperature.
- The density of the thin rods was found to increase to a certain point with the increase in the LED. Using very high LED showed further decrease in the density due to the high

spattering issue. Chemical etching of the printed sample at an acid solution (HF : HNO<sub>3</sub> : H<sub>2</sub>O = 1 : 2 : 3) for 3 minutes removed the partially melted powder and smoothed the surface.

- Among the sample fabricated, the sample fabricated with LED of 170 J/mm<sup>3</sup> demonstrated height superelasticity with 92% recovery ratio as well as low loading stress recommended for the stent applicaiton.
- After performing the aging heat treatment at 450 °C for 30 minutes, the sample demonstrated perfect superelasticity with 4.5% recoverable strain and 100% recovery ratio. Obtaining perfect superelasticity in NiTi is difficult even in the traditional manufacturing route, and this is first time to report such superelasticity in the AM processed NiTi.
- The stent fabricated with the developed processing conditions showed mechanical integrity during deformation and visual superelastic property.

The work proposes a viable route of fabricating NiTi stent by AM while maintaining desirable mechanical and functional properties. Further research work needs to be done to study the biocompatibility and fatigue performance of the fabricated stent using the developed processing condition.

## Chapter 5: Summary and Future Work

### 5.1. Summary

The dissertation focuses on the attempt to advance the fabrication of NiTi devices by laser powder bed fusion (LPBF) technique for biomedical applications. Though LPBF is well studied for other materials such as steel, Ti and Ni base alloys, the study on fabricating NiTi by LPBF is still in the initial stage. Hence, the work was designed to address certain challenges in fabricating NiTi by LPBF. At first, a multistep printing method was developed to reduce the manufacturing cost by fabricating NiTi bulk sample on a Ti substrate which is four times cheaper than a NiTi substrate. Incorporation of initial base layers followed by the lattice structure assisted in improving the part-substrate bonding as well as reducing the warping issue in the deposited layers that ultimately enabled printing NiTi on Ti substrate. Afterwards, a heat treatment protocol has been developed to homogenize the microstructure of the printed sample and tailor the  $A_f$  temperature closely below the body temperature. The microstructures, phases, grain orientations as well as the phase transformations of the as printed and the heat-treated sample were thoroughly characterized. The heat-treated sample showed improved superelastic characteristics (6.64% recoverable strain) compared to the as-printed samples (4.95% recoverable strain) due to the formation of ultrafine Ni rich precipitate  $Ni_4Ti_3$  that facilitated easy phase transformation and reduced the plastic deformation.

One of the major goals of the work was to fabricate self-expandible NiTi stent by LPBF. However, fabricating thin structures by LPBF has been always challenging because of the structural inaccuracy and mechanical failure. To fabricate NiTi stent that consist strut of less than 200  $\mu m$  thickness, the LPBF printing parameter was thoroughly studied to achieve the minimum porosity, structural accuracy, mechanical integrity as well as maximum superelastic property. The chemical-

based surface treatment was used to smoothen the surface of the printed samples. Finally, the aging treatment was performed that provided with  $A_f$  temperature less than the body temperature as well as demonstrated perfect superelasticity with 100% strain recovery in the 3-point bending test at body temperature. The printed stent with the developed parameters and post processing showed structural accuracy, mechanical integrity and visual superelasticity.

## **5.2. Future work**

The work was designed to improve the materials property of the LPBF NiTi. However, the performance of a biomedical device is dependent on both the materials properties as well as on the design of the device. Extensive research work needs to be done, using the obtained materials performance result in this work, to study the design of a stent to reduce the stress concentration, improve the fatigue life as well as achieve the proper mechanical properties required during service. The work was done mainly focusing on improving the mechanical and functional properties. Further work needs to be performed to study the biocompatibility and the long-term fatigue property. All the tests performed in the work were done in the materials level with the standard loading cycles. To confirm the desired property in a stent, component level tests need to be performed with the simulated stress cycles that a typical stent is supposed to experience during service.

## REFERENCES

- [1] T. Duerig, A. Pelton, and D. Stöckel, “An overview of nitinol medical applications,” *Materials Science and Engineering: A*, vol. 273–275, pp. 149–160, Dec. 1999, doi: 10.1016/S0921-5093(99)00294-4.
- [2] J. M. Jani, M. Leary, A. Subic, and M. A. Gibson, “A review of shape memory alloy research, applications and opportunities,” *Materials & Design (1980-2015)*, vol. 56, p. 1078, 2014.
- [3] C. Menna, F. Auricchio, and D. Asprone, “Chapter 13 - Applications of Shape Memory Alloys in Structural Engineering,” in *Shape Memory Alloy Engineering*, L. Lecce and A. Concilio, Eds., Boston: Butterworth-Heinemann, 2015, pp. 369–403. doi: 10.1016/B978-0-08-099920-3.00013-9.
- [4] D. Stoeckel, “Nitinol medical devices and implants,” *Minimally Invasive Therapy & Allied Technologies*, vol. 9, no. 2, pp. 81–88, Jan. 2000, doi: 10.3109/13645700009063054.
- [5] A. R. Pelton, J. Dicello, and S. Miyazaki, “Optimisation of processing and properties of medical grade Nitinol wire,” *Minimally Invasive Therapy & Allied Technologies*, vol. 9, no. 2, pp. 107–118, Jan. 2000, doi: 10.3109/13645700009063057.
- [6] T. W. Duerig and M. Wholey, “A comparison of balloon- and self-expanding stents,” *Minimally Invasive Therapy & Allied Technologies*, vol. 11, no. 4, pp. 173–178, Jan. 2002, doi: 10.1080/136457002760273386.
- [7] D. Hodgson and S. Russell, “Nitinol melting, manufacture and fabrication,” *Minimally Invasive Therapy & Allied Technologies*, vol. 9, no. 2, pp. 61–65, Jan. 2000, doi: 10.3109/13645700009063051.
- [8] J. W. Mwangi, L. T. Nguyen, V. D. Bui, T. Berger, H. Zeidler, and A. Schubert, “Nitinol manufacturing and micromachining: A review of processes and their suitability in processing medical-grade nitinol,” *Journal of Manufacturing Processes*, vol. 38, pp. 355–369, Feb. 2019, doi: 10.1016/j.jmapro.2019.01.003.
- [9] S. W. Robertson, “On the Mechanical Properties and Microstructure of Nitinol for Biomedical Stent Applications,” Lawrence Berkeley National Lab. (LBNL), Berkeley, CA (United States), LBNL-62454, Jan. 2006. doi: 10.2172/901533.
- [10] K. Otsuka and X. Ren, “Physical metallurgy of Ti–Ni-based shape memory alloys,” *Progress in Materials Science*, vol. 50, no. 5, pp. 511–678, Jul. 2005, doi: 10.1016/j.pmatsci.2004.10.001.
- [11] S. K. Patel, B. Behera, B. Swain, R. Roshan, D. Sahoo, and A. Behera, “A review on NiTi alloys for biomedical applications and their biocompatibility,” *Materials Today: Proceedings*, vol. 33, pp. 5548–5551, Jan. 2020, doi: 10.1016/j.matpr.2020.03.538.

- [12] K. Maleckis *et al.*, “Nitinol Stents in the Femoropopliteal Artery: A Mechanical Perspective on Material, Design, and Performance,” *Ann Biomed Eng*, vol. 46, no. 5, pp. 684–704, May 2018, doi: 10.1007/s10439-018-1990-1.
- [13] G. B. Kauffman and I. Mayo, “The Story of Nitinol: The Serendipitous Discovery of the Memory Metal and Its Applications,” *Chem. Educator*, vol. 2, no. 2, pp. 1–21, Jun. 1997, doi: 10.1007/s00897970111a.
- [14] R. R. Adharapurapu and K. S. Vecchio, “Superelasticity in a New BioImplant Material: Ni-rich 55NiTi Alloy,” *Exp Mech*, vol. 47, no. 3, pp. 365–371, Jun. 2007, doi: 10.1007/s11340-006-9004-x.
- [15] M. Kumar, “Nitinol-Based Shape-Memory Alloys,” in *Shape Memory Composites Based on Polymers and Metals for 4D Printing: Processes, Applications and Challenges*, M. R. Maurya, K. K. Sadasivuni, J.-J. Cabibihan, S. Ahmad, and S. Kazim, Eds., Cham: Springer International Publishing, 2022, pp. 45–66. doi: 10.1007/978-3-030-94114-7\_3.
- [16] W.-S. Chu *et al.*, “Review of biomimetic underwater robots using smart actuators,” *Int. J. Precis. Eng. Manuf.*, vol. 13, no. 7, pp. 1281–1292, Jul. 2012, doi: 10.1007/s12541-012-0171-7.
- [17] K. A. Tsoi, J. Schrooten, and R. Stalmans, “Part I. Thermomechanical characteristics of shape memory alloys,” *Materials Science and Engineering: A*, vol. 368, no. 1, pp. 286–298, Mar. 2004, doi: 10.1016/j.msea.2003.11.006.
- [18] R. Chaudhari, J. J. Vora, and D. M. Parikh, “A Review on Applications of Nitinol Shape Memory Alloy,” in *Recent Advances in Mechanical Infrastructure*, A. K. Parwani, P. L. Ramkumar, K. Abhishek, and S. K. Yadav, Eds., in *Lecture Notes in Intelligent Transportation and Infrastructure*. Singapore: Springer, 2021, pp. 123–132. doi: 10.1007/978-981-33-4176-0\_10.
- [19] M. H. Elahinia, *Shape Memory Alloy Actuators: Design, Fabrication, and Experimental Evaluation*. John Wiley & Sons, 2016.
- [20] J. Frenzel, A. Wiczorek, I. Opahle, B. Maaß, R. Drautz, and G. Eggeler, “On the effect of alloy composition on martensite start temperatures and latent heats in Ni–Ti-based shape memory alloys,” *Acta Materialia*, vol. 90, pp. 213–231, May 2015, doi: 10.1016/j.actamat.2015.02.029.
- [21] K. Otsuka and T. Kakeshita, “Science and Technology of Shape-Memory Alloys: New Developments,” *MRS Bulletin*, vol. 27, no. 2, pp. 91–100, Feb. 2002, doi: 10.1557/mrs2002.43.
- [22] N. Ono, A. Satoh, and H. Ohta, “A Discussion on the Mechanical Properties of Shape Memory Alloys Based on a Polycrystal Model,” *Materials Transactions, JIM*, vol. 30, no. 10, pp. 756–764, 1989, doi: 10.2320/matertrans1989.30.756.

- [23] N. Zhou, C. Shen, M. F.-X. Wagner, G. Eggeler, M. J. Mills, and Y. Wang, "Effect of Ni<sub>4</sub>Ti<sub>3</sub> precipitation on martensitic transformation in Ti–Ni," *Acta Materialia*, vol. 58, no. 20, pp. 6685–6694, Dec. 2010, doi: 10.1016/j.actamat.2010.08.033.
- [24] S. Jiang, Y. Zhang, Y. Zhao, S. Liu, L. Hu, and C. Zhao, "Influence of Ni<sub>4</sub>Ti<sub>3</sub> precipitates on phase transformation of NiTi shape memory alloy," *Transactions of Nonferrous Metals Society of China*, vol. 25, no. 12, pp. 4063–4071, Dec. 2015, doi: 10.1016/S1003-6326(15)64056-0.
- [25] G. M. Michal and R. Sinclair, "The structure of TiNi martensite," *Acta Crystallographica Section B*, vol. 37, no. 10, pp. 1803–1807, 1981, doi: 10.1107/S0567740881007292.
- [26] Y. Guo, A. Klink, C. Fu, and J. Snyder, "Machinability and surface integrity of Nitinol shape memory alloy," *CIRP Annals*, vol. 62, no. 1, pp. 83–86, Jan. 2013, doi: 10.1016/j.cirp.2013.03.004.
- [27] R. Bogue, "Shape-memory materials: a review of technology and applications," *Assembly Automation*, vol. 29, no. 3, pp. 214–219, Jan. 2009, doi: 10.1108/01445150910972895.
- [28] S. Kumar Patel, B. Swain, R. Roshan, N. K. Sahu, and A. Behera, "A brief review of shape memory effects and fabrication processes of NiTi shape memory alloys," *Materials Today: Proceedings*, vol. 33, pp. 5552–5556, Jan. 2020, doi: 10.1016/j.matpr.2020.03.539.
- [29] A. N. Alagha, S. Hussain, and W. Zaki, "Additive manufacturing of shape memory alloys: A review with emphasis on powder bed systems," *Materials & Design*, vol. 204, p. 109654, Jun. 2021, doi: 10.1016/j.matdes.2021.109654.
- [30] M. Elahinia, N. Shayesteh Moghaddam, M. Taheri Andani, A. Amerinatanzi, B. A. Bimber, and R. F. Hamilton, "Fabrication of NiTi through additive manufacturing: A review," *Progress in Materials Science*, vol. 83, pp. 630–663, Oct. 2016, doi: 10.1016/j.pmatsci.2016.08.001.
- [31] C. Wang *et al.*, "Additive manufacturing of NiTi shape memory alloys using pre-mixed powders," *Journal of Materials Processing Technology*, vol. 271, pp. 152–161, Sep. 2019, doi: 10.1016/j.jmatprotec.2019.03.025.
- [32] E. Farber, J.-N. Zhu, A. Popovich, and V. Popovich, "A review of NiTi shape memory alloy as a smart material produced by additive manufacturing," *Materials Today: Proceedings*, vol. 30, pp. 761–767, Jan. 2020, doi: 10.1016/j.matpr.2020.01.563.
- [33] X. Zhang, C. J. Yocom, B. Mao, and Y. Liao, "Microstructure evolution during selective laser melting of metallic materials: A review," *Journal of Laser Applications*, vol. 31, no. 3, p. 031201, Aug. 2019, doi: 10.2351/1.5085206.

- [34] C. Haberland, M. Elahinia, J. M. Walker, H. Meier, and J. Frenzel, "On the development of high quality NiTi shape memory and pseudoelastic parts by additive manufacturing," *Smart Mater. Struct.*, vol. 23, no. 10, p. 104002, Sep. 2014, doi: 10.1088/0964-1726/23/10/104002.
- [35] X. Wang *et al.*, "Effect of process parameters on the phase transformation behavior and tensile properties of NiTi shape memory alloys fabricated by selective laser melting," *Additive Manufacturing*, vol. 36, p. 101545, Dec. 2020, doi: 10.1016/j.addma.2020.101545.
- [36] S. Dadbakhsh, B. Vrancken, J.-P. Kruth, J. Luyten, and J. Van Humbeeck, "Texture and anisotropy in selective laser melting of NiTi alloy," *Materials Science and Engineering: A*, vol. 650, pp. 225–232, Jan. 2016, doi: 10.1016/j.msea.2015.10.032.
- [37] Y. Liu, Z. L. Xie, J. Van Humbeeck, and L. Delaey, "Effect of texture orientation on the martensite deformation of NiTi shape memory alloy sheet," *Acta Materialia*, vol. 47, no. 2, pp. 645–660, Jan. 1999, doi: 10.1016/S1359-6454(98)00376-0.
- [38] L. Xue *et al.*, "Laser Powder Bed Fusion of Defect-Free NiTi Shape Memory Alloy Parts with Superior Tensile Superelasticity," *Acta Materialia*, vol. 229, p. 117781, May 2022, doi: 10.1016/j.actamat.2022.117781.
- [39] A. R. Pelton, S. M. Russell, and J. DiCello, "The physical metallurgy of nitinol for medical applications," *JOM*, vol. 55, no. 5, pp. 33–37, May 2003, doi: 10.1007/s11837-003-0243-3.
- [40] M. Mahmoudi *et al.*, "On the printability and transformation behavior of nickel-titanium shape memory alloys fabricated using laser powder-bed fusion additive manufacturing," *Journal of Manufacturing Processes*, vol. 35, pp. 672–680, Oct. 2018, doi: 10.1016/j.jmapro.2018.08.037.
- [41] X. Lu, M. Cervera, M. Chiumenti, and X. Lin, "Residual Stresses Control in Additive Manufacturing," *Journal of Manufacturing and Materials Processing*, vol. 5, no. 4, Art. no. 4, Dec. 2021, doi: 10.3390/jmmp5040138.
- [42] A. Takezawa, Q. Chen, and A. C. To, "Optimally variable density lattice to reduce warping thermal distortion of laser powder bed fusion," *Additive Manufacturing*, vol. 48, p. 102422, Dec. 2021, doi: 10.1016/j.addma.2021.102422.
- [43] J. Wang, Z. Pan, K. Carpenter, J. Han, Z. Wang, and H. Li, "Comparative study on crystallographic orientation, precipitation, phase transformation and mechanical response of Ni-rich NiTi alloy fabricated by WAAM at elevated substrate heating temperatures," *Materials Science and Engineering: A*, vol. 800, p. 140307, Jan. 2021, doi: 10.1016/j.msea.2020.140307.
- [44] P. Jamshidi *et al.*, "Development, characterisation, and modelling of processability of nitinol stents using laser powder bed fusion," *Journal of Alloys and Compounds*, vol. 909, p. 164681, Jul. 2022, doi: 10.1016/j.jallcom.2022.164681.

- [45] O. A. Mohamed, S. H. Masood, and W. Xu, “Nickel-titanium shape memory alloys made by selective laser melting: a review on process optimisation,” *Adv. Manuf.*, vol. 10, no. 1, pp. 24–58, Mar. 2022, doi: 10.1007/s40436-021-00376-9.
- [46] T. Bormann, R. Schumacher, B. Müller, M. Mertmann, and M. de Wild, “Tailoring Selective Laser Melting Process Parameters for NiTi Implants,” *J. of Materi Eng and Perform.*, vol. 21, no. 12, pp. 2519–2524, Dec. 2012, doi: 10.1007/s11665-012-0318-9.
- [47] S. Saedi, A. S. Turabi, M. Taheri Andani, C. Haberland, H. Karaca, and M. Elahinia, “The influence of heat treatment on the thermomechanical response of Ni-rich NiTi alloys manufactured by selective laser melting,” *Journal of Alloys and Compounds*, vol. 677, pp. 204–210, Aug. 2016, doi: 10.1016/j.jallcom.2016.03.161.
- [48] M. Fonte and A. Saigal, “Effects of crystallographic texture directionality on the compressive stress–strain response of shape recovered polycrystalline nitinol,” *Scripta Materialia*, vol. 63, no. 3, pp. 320–323, Aug. 2010, doi: 10.1016/j.scriptamat.2010.04.017.
- [49] K. Gall, H. Sehitoglu, R. Anderson, I. Karaman, Y. I. Chumlyakov, and I. V. Kireeva, “On the mechanical behavior of single crystal NiTi shape memory alloys and related polycrystalline phenomenon,” *Materials Science and Engineering: A*, vol. 317, no. 1, pp. 85–92, Oct. 2001, doi: 10.1016/S0921-5093(01)01183-2.
- [50] N. Shayesteh Moghaddam *et al.*, “Achieving superelasticity in additively manufactured NiTi in compression without post-process heat treatment,” *Sci Rep*, vol. 9, no. 1, Art. no. 1, Jan. 2019, doi: 10.1038/s41598-018-36641-4.
- [51] C. P. Frick *et al.*, “Thermal processing of polycrystalline NiTi shape memory alloys,” *Materials Science and Engineering: A*, vol. 405, no. 1, pp. 34–49, Sep. 2005, doi: 10.1016/j.msea.2005.05.102.
- [52] J. Korpela, A. Kokkari, H. Korhonen, M. Malin, T. Närhi, and J. Seppälä, “Biodegradable and bioactive porous scaffold structures prepared using fused deposition modeling,” *Journal of Biomedical Materials Research Part B: Applied Biomaterials*, vol. 101B, no. 4, pp. 610–619, 2013, doi: 10.1002/jbm.b.32863.
- [53] R. Castaño *et al.*, “Development and Implementation of a New Nitinol Stent Design for Managing Benign Stenoses and Fistulas of the Digestive Tract,” *undefined*, 2015, Accessed: Oct. 25, 2022. [Online]. Available: <https://www.semanticscholar.org/paper/Development-and-Implementation-of-a-New-Nitinol-for-Casta%20B1o-Alvarez/4aaec18f5840c3baa484ea0f025875142772bce7>
- [54] T. W. Duerig, D. E. Tolomeo, and M. Wholey, “An overview of superelastic stent design,” *Minimally Invasive Therapy & Allied Technologies*, vol. 9, no. 3–4, pp. 235–246, Jan. 2000, doi: 10.1080/13645700009169654.

- [55] D. Stoeckel, A. Pelton, and T. Duerig, “Self-expanding nitinol stents: material and design considerations,” *Eur Radiol*, vol. 14, no. 2, pp. 292–301, Feb. 2004, doi: 10.1007/s00330-003-2022-5.
- [56] T. W. Duerig, D. E. Tolomeo, and M. Wholey, “An overview of superelastic stent design,” *Minimally Invasive Therapy & Allied Technologies*, vol. 9, no. 3–4, pp. 235–246, Jan. 2000, doi: 10.1080/13645700009169654.
- [57] D. Stoeckel, “Nitinol medical devices and implants,” *Minimally Invasive Therapy & Allied Technologies*, vol. 9, no. 2, pp. 81–88, Jan. 2000, doi: 10.3109/13645700009063054.
- [58] A. G. Demir and B. Previtali, “Additive manufacturing of cardiovascular CoCr stents by selective laser melting,” *Materials & Design*, vol. 119, pp. 338–350, Apr. 2017, doi: 10.1016/j.matdes.2017.01.091.
- [59] S. Maffia *et al.*, “Selective laser melting of NiTi stents with open-cell and variable diameter,” *Smart Mater. Struct.*, vol. 30, no. 10, p. 105010, Aug. 2021, doi: 10.1088/1361-665X/ac1908.
- [60] L. Yan *et al.*, “Evaluation and characterization of nitinol stents produced by selective laser melting with various process parameters,” *Prog Addit Manuf*, Mar. 2022, doi: 10.1007/s40964-022-00289-4.
- [61] A. Chakraborty *et al.*, “In-process failure analysis of thin-wall structures made by laser powder bed fusion additive manufacturing,” *Journal of Materials Science & Technology*, vol. 98, pp. 233–243, Jan. 2022, doi: 10.1016/j.jmst.2021.05.017.
- [62] J. Lee and Y. C. Shin, “Effects of Composition and Post Heat Treatment on Shape Memory Characteristics and Mechanical Properties for Laser Direct Deposited Nitinol,” *Lasers Manuf. Mater. Process.*, vol. 6, no. 1, pp. 41–58, Mar. 2019, doi: 10.1007/s40516-019-0079-5.
- [63] X. Chen, K. Liu, W. Guo, N. Gangil, A. N. Siddiquee, and S. Konovalov, “The fabrication of NiTi shape memory alloy by selective laser melting: a review,” *Rapid Prototyping Journal*, vol. 25, no. 8, pp. 1421–1432, Jan. 2019, doi: 10.1108/RPJ-11-2018-0292.
- [64] *Materials Handbook*. London: Springer London, 2008. doi: 10.1007/978-1-84628-669-8.
- [65] P. R. Halani, I. Kaya, Y. C. Shin, and H. E. Karaca, “Phase transformation characteristics and mechanical characterization of nitinol synthesized by laser direct deposition,” *Materials Science and Engineering: A*, vol. 559, pp. 836–843, Jan. 2013, doi: 10.1016/j.msea.2012.09.031.
- [66] J. C. Chekotu, R. Groarke, K. O’Toole, and D. Brabazon, “Advances in Selective Laser Melting of Nitinol Shape Memory Alloy Part Production,” *Materials*, vol. 12, no. 5, Art. no. 5, Jan. 2019, doi: 10.3390/ma12050809.

- [67] C. A. Biffi, A. Tuissi, and A. G. Demir, “Martensitic transformation, microstructure and functional behavior of thin-walled Nitinol produced by micro laser metal wire deposition,” *Journal of Materials Research and Technology*, vol. 12, pp. 2205–2215, May 2021, doi: 10.1016/j.jmrt.2021.03.108.
- [68] Z. Yu *et al.*, “Study on properties of SLM-NiTi shape memory alloy under the same energy density,” *Journal of Materials Research and Technology*, vol. 13, pp. 241–250, Jul. 2021, doi: 10.1016/j.jmrt.2021.04.058.
- [69] Q. Ren *et al.*, “Effect of a constant laser energy density on the evolution of microstructure and mechanical properties of NiTi shape memory alloy fabricated by laser powder bed fusion,” *Optics & Laser Technology*, vol. 152, p. 108182, Aug. 2022, doi: 10.1016/j.optlastec.2022.108182.
- [70] L. Thijs, K. Kempen, J.-P. Kruth, and J. Van Humbeeck, “Fine-structured aluminium products with controllable texture by selective laser melting of pre-alloyed AlSi10Mg powder,” *Acta Materialia*, vol. 61, no. 5, pp. 1809–1819, Mar. 2013, doi: 10.1016/j.actamat.2012.11.052.
- [71] Y. Yang *et al.*, “Evolution of functional properties realized by increasing laser scanning speed for the selective laser melting fabricated NiTi alloy,” *Journal of Alloys and Compounds*, vol. 804, pp. 220–229, Oct. 2019, doi: 10.1016/j.jallcom.2019.06.340.
- [72] C. Y. Yap *et al.*, “Review of selective laser melting: Materials and applications,” *Applied Physics Reviews*, vol. 2, no. 4, p. 041101, Dec. 2015, doi: 10.1063/1.4935926.
- [73] J. Frenzel, E. P. George, A. Dlouhy, Ch. Somsen, M. F.-X. Wagner, and G. Eggeler, “Influence of Ni on martensitic phase transformations in NiTi shape memory alloys,” *Acta Materialia*, vol. 58, no. 9, pp. 3444–3458, May 2010, doi: 10.1016/j.actamat.2010.02.019.
- [74] S. K. Patel, B. Behera, B. Swain, R. Roshan, D. Sahoo, and A. Behera, “A review on NiTi alloys for biomedical applications and their biocompatibility,” *Materials Today: Proceedings*, vol. 33, pp. 5548–5551, Jan. 2020, doi: 10.1016/j.matpr.2020.03.538.
- [75] A. Biscarini, G. Mazzolai, and A. Tuissi, “Enhanced Nitinol Properties for Biomedical Applications,” *Recent Patents on Biomedical Engineering*, vol. 1, no. 3, pp. 180–196, Nov. 2008.
- [76] J. Khalil Allafi, X. Ren, and G. Eggeler, “The mechanism of multistage martensitic transformations in aged Ni-rich NiTi shape memory alloys,” *Acta Materialia*, vol. 50, no. 4, pp. 793–803, Feb. 2002, doi: 10.1016/S1359-6454(01)00385-8.
- [77] M. Elahinia, N. Shayesteh Moghaddam, M. Taheri Andani, A. Amerinatanzi, B. A. Bimber, and R. F. Hamilton, “Fabrication of NiTi through additive manufacturing: A review,” *Progress in Materials Science*, vol. 83, pp. 630–663, Oct. 2016, doi: 10.1016/j.pmatsci.2016.08.001.

- [78] N. Shayesteh Moghaddam *et al.*, “Achieving superelasticity in additively manufactured NiTi in compression without post-process heat treatment,” *Sci Rep*, vol. 9, no. 1, Art. no. 1, Jan. 2019, doi: 10.1038/s41598-018-36641-4.
- [79] J. Sam, B. Franco, J. Ma, I. Karaman, A. Elwany, and J. H. Mabe, “Tensile actuation response of additively manufactured nickel-titanium shape memory alloys,” *Scripta Materialia*, vol. 146, pp. 164–168, Mar. 2018, doi: 10.1016/j.scriptamat.2017.11.013.
- [80] J. Khalil-Allafi and B. Amin-Ahmadi, “Multiple-step martensitic transformations in the Ni<sub>51</sub>Ti<sub>49</sub> single crystal,” *J Mater Sci*, vol. 45, no. 23, pp. 6440–6445, Dec. 2010, doi: 10.1007/s10853-010-4729-4.
- [81] W. Tirry, D. Schryvers, K. Jorissen, and D. Lamoen, “Electron-diffraction structure refinement of Ni<sub>4</sub>Ti<sub>3</sub> precipitates in Ni<sub>52</sub>Ti<sub>48</sub>,” *Acta Cryst B*, vol. 62, no. 6, pp. 966–971, Dec. 2006, doi: 10.1107/S0108768106036457.
- [82] J. Ye, R. K. Mishra, A. R. Pelton, and A. M. Minor, “Direct observation of the NiTi martensitic phase transformation in nanoscale volumes,” *Acta Materialia*, vol. 58, no. 2, pp. 490–498, Jan. 2010, doi: 10.1016/j.actamat.2009.09.027.
- [83] K. Safaei *et al.*, “Additive Manufacturing of NiTi Shape Memory Alloy for Biomedical Applications: Review of the LPBF Process Ecosystem,” *JOM*, vol. 73, no. 12, pp. 3771–3786, Dec. 2021, doi: 10.1007/s11837-021-04937-y.
- [84] A. Biscarini, G. Mazzolai, and A. Tuissi, “Enhanced Nitinol Properties for Biomedical Applications,” *Recent Patents on Biomedical Engineering*, vol. 1, no. 3, pp. 180–196, Nov. 2008.
- [85] J. Khalil-Allafi, A. Dlouhy, and G. Eggeler, “Ni<sub>4</sub>Ti<sub>3</sub>-precipitation during aging of NiTi shape memory alloys and its influence on martensitic phase transformations,” *Acta Materialia*, vol. 50, no. 17, pp. 4255–4274, Oct. 2002, doi: 10.1016/S1359-6454(02)00257-4.
- [86] X. B. Wang, B. Verlinden, and J. Van Humbeeck, “R-phase transformation in NiTi alloys,” *Materials Science and Technology*, vol. 30, no. 13, pp. 1517–1529, Nov. 2014, doi: 10.1179/1743284714Y.0000000590.
- [87] J. Khalil-Allafi, A. Dlouhy, and G. Eggeler, “Ni<sub>4</sub>Ti<sub>3</sub>-precipitation during aging of NiTi shape memory alloys and its influence on martensitic phase transformations,” *Acta Materialia*, vol. 50, no. 17, pp. 4255–4274, Oct. 2002, doi: 10.1016/S1359-6454(02)00257-4.
- [88] A. Deschamps and C. R. Hutchinson, “Precipitation kinetics in metallic alloys: Experiments and modeling,” *Acta Materialia*, vol. 220, p. 117338, Nov. 2021, doi: 10.1016/j.actamat.2021.117338.

- [89] Q. Fang *et al.*, “A statistical theory of probability-dependent precipitation strengthening in metals and alloys,” *Journal of the Mechanics and Physics of Solids*, vol. 122, pp. 177–189, Jan. 2019, doi: 10.1016/j.jmps.2018.09.010.
- [90] J. Gan *et al.*, “Effect of laser energy density on the evolution of Ni<sub>4</sub>Ti<sub>3</sub> precipitate and property of NiTi shape memory alloys prepared by selective laser melting,” *Journal of Alloys and Compounds*, vol. 869, p. 159338, Jul. 2021, doi: 10.1016/j.jallcom.2021.159338.
- [91] S. Dadbakhsh, B. Vrancken, J.-P. Kruth, J. Luyten, and J. Van Humbeeck, “Texture and anisotropy in selective laser melting of NiTi alloy,” *Materials Science and Engineering: A*, vol. 650, pp. 225–232, Jan. 2016, doi: 10.1016/j.msea.2015.10.032.
- [92] S. Saedi, A. S. Turabi, M. Taheri Andani, C. Haberland, H. Karaca, and M. Elahinia, “The influence of heat treatment on the thermomechanical response of Ni-rich NiTi alloys manufactured by selective laser melting,” *Journal of Alloys and Compounds*, vol. 677, pp. 204–210, Aug. 2016, doi: 10.1016/j.jallcom.2016.03.161.
- [93] M. J. Mahtabi, N. Shamsaei, and M. R. Mitchell, “Fatigue of Nitinol: The state-of-the-art and ongoing challenges,” *Journal of the Mechanical Behavior of Biomedical Materials*, vol. 50, pp. 228–254, Oct. 2015, doi: 10.1016/j.jmbbm.2015.06.010.
- [94] B. Chad Hornbuckle, X. X. Yu, R. D. Noebe, R. Martens, M. L. Weaver, and G. B. Thompson, “Hardening behavior and phase decomposition in very Ni-rich Nitinol alloys,” *Materials Science and Engineering: A*, vol. 639, pp. 336–344, Jul. 2015, doi: 10.1016/j.msea.2015.04.079.
- [95] T. Gladman, “Precipitation hardening in metals,” *Materials Science and Technology*, vol. 15, no. 1, pp. 30–36, Jan. 1999, doi: 10.1179/026708399773002782.
- [96] V. A. Phillips, “Hardening mechanisms in a precipitation hardenable nickel-12.71 at. % aluminium alloy,” *The Philosophical Magazine: A Journal of Theoretical Experimental and Applied Physics*, vol. 16, no. 139, pp. 103–117, Jul. 1967, doi: 10.1080/14786436708229260.
- [97] A. Nadai, “Plastic Behavior of Metals in the Strain-Hardening Range. Part I,” *Journal of Applied Physics*, vol. 8, no. 3, pp. 205–213, Apr. 2004, doi: 10.1063/1.1710282.
- [98] C. Haberland, H. Meier, and J. Frenzel, “On the Properties of Ni-Rich NiTi Shape Memory Parts Produced by Selective Laser Melting,” presented at the ASME 2012 Conference on Smart Materials, Adaptive Structures and Intelligent Systems, American Society of Mechanical Engineers Digital Collection, Jul. 2013, pp. 97–104. doi: 10.1115/SMASIS2012-8040.
- [99] S. Dadbakhsh, M. Speirs, J. V. Humbeeck, and J.-P. Kruth, “Laser additive manufacturing of bulk and porous shape-memory NiTi alloys: From processes to potential biomedical applications,” *MRS Bulletin*, vol. 41, no. 10, pp. 765–774, Oct. 2016, doi: 10.1557/mrs.2016.209.

- [100] W. Haider, N. Munroe, V. Tek, C. Pulletikurthi, P. K. S. Gill, and S. Pandya, “Surface Modifications of Nitinol,” *JLT*, vol. 19, no. 2, 2009, doi: 10.1615/JLongTermEffMedImplants.v19.i2.30.
- [101] L. M. Pérez, L. Gracia-Villa, J. A. Puértolas, M. Arruebo, S. Irusta, and J. Santamaría, “Effect of Nitinol surface treatments on its physico-chemical properties,” *Journal of Biomedical Materials Research Part B: Applied Biomaterials*, vol. 91B, no. 1, pp. 337–347, 2009, doi: 10.1002/jbm.b.31407.
- [102] S. Cai, J. E. Schaffer, M. R. Daymond, C. Yu, and Y. Ren, “Effect of heat treatment temperature on nitinol wire,” *Appl. Phys. Lett.*, vol. 105, no. 7, p. 071904, Aug. 2014, doi: 10.1063/1.4893595.
- [103] K. Maleckis *et al.*, “Nitinol Stents in the Femoropopliteal Artery: A Mechanical Perspective on Material, Design, and Performance,” *Ann Biomed Eng*, vol. 46, no. 5, pp. 684–704, May 2018, doi: 10.1007/s10439-018-1990-1.
- [104] author/clayton-dekorne, “Beam Stress and Strain: A Lesson in Statics,” JLC Online. Accessed: Jan. 22, 2024. [Online]. Available: [https://www.jlconline.com/Training-the-Trades/beam-stress-and-strain-a-lesson-in-statics\\_o](https://www.jlconline.com/Training-the-Trades/beam-stress-and-strain-a-lesson-in-statics_o)
- [105] *3D Printed Nitinol Shows Shape Memory Property*, (Nov. 13, 2023). Accessed: Jan. 22, 2024. [Online Video]. Available: <https://www.youtube.com/watch?v=zeeK5cipF7Y>
- [106] “3D Printed Superelastic Nitinol Stent - YouTube.” Accessed: Jan. 22, 2024. [Online]. Available: <https://www.youtube.com/shorts/PgGBk94Ab8c>